UTS UNIVERSITY OF TECHNOLOGY SYDNEY

# Advanced Conformal Transmitarrays for 5G and Beyond Wireless Communications

**by Lizhao Song**

Thesis submitted in fulfilment of the requirements for the degree of

**DOCTOR OF PHILOSOPHY**

under the supervision of Dr Peiyuan Qin
and Prof. Yingjie Jay Guo

University of Technology Sydney
Faculty of Engineering and Information Technology

July 2021

# CERTIFICATE OF ORIGINAL AUTHORSHIP

I, Lizhao Song declare that this thesis, is submitted in fulfilment of the requirements for the award of Doctor of Philosophy, in School of Electrical and Data Engineering/Faculty of Engineering and Information Technology at the University of Technology Sydney.

This thesis is wholly my own work unless otherwise reference or acknowledged. In addition, I certify that all information sources and literature used are indicated in the thesis.

This document has not been submitted for qualifications at any other academic institution.

This research is supported by the Australian Government Research Training Program.

Signature: Production Note:
Signature removed prior to publication.

Date: 26/07/2021

# ACKNOWLEDGEMENTS

I would like to thank University of Technology Sydney and Faculty of Engineering and Information Technology for providing scholarships to support my PhD study in the last three years. This dissertation would not have been produced without assistance and supports from my university.

I owe my deepest gratitude to my principal supervisor Dr Peiyuan Qin. He is the one who unlocked the door of research for me and ignited my passion to research. I still remember how I gradually grow from an ignorant girl into a dedicated researcher under his guidance and supervision. For all of my presentations in front of public, he is the one who checked each word and sentence over and over, and provided me feedback and advice in the first place. For all of my antenna designs, he is the one who provided me valuable ideas and enlightened me to develop innovative works. For all of my papers, he is the one who revised them again and again, and corrected my errors patiently. There are too much kindness and assistance from him to be listed here. He does not only influence me research-wisely, but also acts as a successful personal model. I have learned generosity, thoughtfulness and optimism from him, which benefit me significantly.

I am deeply grateful to my co-supervisor, Prof. Y. Jay Guo. As an exceptional researcher in multiple areas, he is knowledgeable and farsighted. He is always supportive on my research and provides me guidance and inspirations. As the director of Global Big Data Technologies Centre (GBDTC), he creates an inclusive and positive research environment to motivate and facilitate my progress. As my supervisor, he offers me numerous invaluable opportunities and platforms. I am profoundly influenced by his serious attitude, kindness and consideration.

I would like to thank my colleague Mr Shulin Chen, who also acts like my senior brother, for his help on my research and personal life. I appreciate his encouragements and stimulations at each of my breakdowns. I also appreciate his correctness and criticism on each of my faults. It is such a luck and pleasure to know him in the past few years.

Besides, I would like to show my genuine appreciation to Prof. Richard W. Ziolkowski, Prof. Bevan Jones and Prof. Trevor Bird for their insightful advice and suggestions on my research. Also, I would like to thank Dr Can Ding, Dr He Zhu and Dr Wei Lin for their kind helps and encouragements. My gratitude also goes to Mr Tianyu Yang, Mr Jiwei Lian, Mr Ming Li, Miss Xuan Wang, Miss Maral Ansari, Miss Haihan Sun and Mr Wei Huang. They have been both my helpful colleagues and lovely friends.

Moreover, I owe a great debt of appreciation to my parents and brother for their consistent love and unconditional support.

# ABSTRACT

Transmitarray antennas (TAs) have received considerable attention as they can serve long-distance communications for space and terrestrial wireless systems. For many wireless communication platforms, such as aircrafts and unmanned aerial vehicles (UAV), conformal TAs, which can be flush mounted onto the shaped platforms, are highly demanded in order to meet the aerodynamic requirements. In this dissertation, a few innovative techniques have been developed for conformal TAs.

Firstly, a thin frequency selective surfaces (FSS) element is developed with a thickness of 0.508 mm ($0.04\lambda_0$ at 25 GHz). It is then applied to a curved TA conformal to a cylindrical surface. The prototype radiates a fixed boresight beam with a peak measured gain of 19.6 dBi and an aperture efficiency of 25.1%. Secondly, a mechanical beam-scanning conformal TA is proposed. Its size is about 2.5 times of the fixed-beam one, steering its beam to seven different radiation angles, i.e., ±15°, ±10°, ±5°, and 0°. The measured prototype shows a stable gain of 18.7 dBi at all beam angles.

Thirdly, to improve the aperture efficiency of conformal TAs further, Huygens metasurface theory is employed to design a dual-layer TA element. The element is composed of two metal layers printed on a single substrate with a 0.5-mm thickness ($0.017\lambda_0$ at 10 GHz). The oblique incidence effects are also considered in the process of element synthesis. Finally, a cylindrically conformal TA is developed, which achieves a measured gain of 20.6 dBi with a 47% aperture efficiency.

Fourthly, by combining connected arrays and true-time-delay lines, a novel technique is introduced to obtain ultrawideband (UWB) TAs. The elements consist of a horizontally connected slot bowtie and vertical meander slot-lines. The TAs have been designed in

both planar and conformal configurations. Stable boresight radiation patterns from 6 GHz to 17 GHz are obtained for both antennas. Compared to conformal TAs using multi-layer FSS elements, the proposed one has an ultra-wide bandwidth of 96% in terms of stable radiation patterns.

Fifthly, a conformal TA, with an elliptical cylindrical contour at a millimetre-wave (mm-wave) band, is presented for wide-angle multibeam radiations. A systematic design procedure is developed. The prototype provides eleven beams with a beam coverage of ±43°. The measured peak boresight gain is 27 dBi at 70.5 GHz with a less than 2.7-dB scanning loss.

# TABLE OF CONTENTS

# LIST OF FIGURES

# LIST OF TABLES

# LIST OF ABBREVIATIONS

| | |
|---|---|
| TAs | Transmitarray antennas |
| RAs | Reflectarray antennas |
| FSS | Frequency Selective Surfaces |
| UAV | Unmanned Aerial Vehicles |
| UWB | Ultrawideband |
| 5G | Fifth generation |
| Mm-wave | Millimetre-wave |
| CP | Circular-polarization |
| 2-D | Two-dimensional |
| 3-D | Three-dimensional |
| EM | Electromagnetic |
| LPDA | Log-periodic dipole antenna |
| SLL | Sidelobe level |

# Chapter 1: Introduction

Transmitarray antennas (TAs) have been considered as one of the competitive candidates to serve long distance communications for space and terrestrial wireless systems [1]. By leveraging the merits of lens antennas and microstrip phased arrays, they can achieve high gains without using complex and lossy feed networks, also provide beam-steering capabilities [2]-[3]. They can achieve a similar function as dielectric lenses, but they are fabricated on printed circuit boards, which makes them lightweight, cheap, and suitable for integrating active devices. Usually, they are composed of numerous phase-shifting elements and one or multiple illuminating feed sources. The transmission phases of these elements are individually designed in order to provide appropriate phase responses to transform the spherical wave coming from the feed source into a planar one. Consequently, highly directive radiation beams can be realized with high gains and narrow beamwidths.

The last two decades have witnessed substantial research efforts in enhancing the performance of TAs, e.g., improving the gain bandwidth, achieving a high aperture efficiency, reducing the entire profile and realizing beam-steering functionalities, etc. However, most of these research works are focused on TAs with planar configurations. They are not suitable to be applied to the airborne platforms with curved shapes, e.g., aircrafts and UAVs. On the other hand, owing to the aerodynamic requirements, it is highly desirable to employ conformal TAs as part of the platform surface can accommodate the TA with a feed placed behind.

## 1.1 Motivation and Scope

Although the design techniques for planar TAs have been quite mature, most of them employ multi-layer array elements [4]-[6]. In order to provide a 360° full phase-variation range with a small transmission loss, multiple metal layers are usually printed on the dielectric substrates separated by air gaps or dielectric materials. Generally, the total thickness of the elements varies from $0.3\lambda_0$ -$1\lambda_0$ ($\lambda_0$ is the wavelength in free space). However, considering the current manufacturing technologies, it is very challenging and expensive to do multi-layer metal printings on curved surfaces, which hinders the developments and implementations of conformal TAs. Few works have been reported to date in conformal TAs [7]-[8], but only preliminary simulation results were provided. Therefore, one of the most feasible solutions is to design very-thin TA elements with a thickness of about 0.5 mm, so that the TA surface is able to be bent and attached onto the curved platforms.

Another important requirement for TAs is to scan the beam. Beam scanning of TAs may not need complicated feed networks, thereby reducing the cost and losses especially at mm-wave bands or higher frequencies [9]. A typical approach to achieve electronically beam scanning in planar TAs is to adjust the element transmission phase by using PIN diodes [10] or varactor diodes [11] for discrete and continuous beam steering, respectively. Nevertheless, for conformal TAs with larger curvatures, it would be very challenging to integrate those active components onto the surfaces.

Moreover, significant research efforts have been devoted to reduce the thickness of planar TA elements in order to compress the entire profile of TAs [12]-[13]. However, at least three metal layers were employed in those designs, which makes conformal designs costly and complicated for precise alignments and multi-layer attachments at high frequencies.

Besides, there is always a trade-off between TA thickness and its aperture efficiency. It can be found that the aperture efficiency is less than 40% when the element thickness is about $0.1\lambda_0$. Therefore, a key challenge for conformal TAs arises in developing dual-layer ultra-thin elements with high aperture efficiencies.

Similar to planar TAs, the operating bandwidth is another issue for conformal designs [14]. Actually, conformal TAs might lead to even narrower bandwidths if we apply ultra-thin elements to form curved surfaces.

Furthermore, mm-wave multibeam antennas are widely hailed as a key antenna technology for the fifth generation (5G) and beyond wireless communication networks, supporting high-data-rate communications with an increased spectral efficiency [15]. To date, most of the published high-gain mm-wave multibeam TAs work at around 30 GHz and provide a beam coverage of about 60° (±30°) with planar profiles. This would limit the applications of this technology. It is of practical importance to industry that the beam coverage is further extended in order to cover a larger angular range enabling point-to-point/multi-point-to-multi-point communications. Besides, it is desirable to have multibeam TAs operating at higher frequency bands. The mm-wave band above 50 GHz offers a large spectrum, and it has a great potential to support future high-speed wireless networks.

Recently, in order to meet rapidly changing demands from various communication scenarios, substantial attention has been attracted to develop reconfigurable TAs with beam-scanning and multi-beam radiation capabilities. The beam reconfigurability can enable tuneable radiation properties in a flexible and reversible way. Considerable research efforts are being devoted to broaden the beam-scanning range and lower the scanning loss. On the other hand, with the 5G wireless networks rolling out, UAVs, also commonly known as drones, are considered as one of the best candidates for delivering

airborne networks due to their high mobility and low cost. UAV aided wireless networks can be swiftly deployed to bridge wireless communication links between satellite and terrestrial platforms/user terminals, providing seamless and pervasive connectivity at remote areas or in the event of ground network infrastructure being destroyed due to natural disasters. Within this context, conformal TAs, which can be flush mounted on the body of the drones, will play an essential role to balance communication and aerodynamic performance. The use of conformal TAs can also significantly reduce maintenance costs and make the communications more robust. Therefore, the development of conformal TAs and its reconfigurability will become an attractive research topic in the future.

## 1.2 Organisation of Thesis

This dissertation is structured with seven chapters, which are described as follows.

In Chapter 1, a brief introduction of TAs and conformal TAs is provided, which is followed by the motivation and scope of conformal TAs and its developments. Moreover, the organisation of the dissertation is clarified, and a statement of contributions of the author is given. The publications from the author are listed at the end.

In Chapter 2, the research background of TAs and its state-of-the-art design technologies are explained in details. The basic working principle and theory of TAs are illustrated. The reported methodologies for various performance enhancements of TAs are introduced and compared, leading to research challenges and gaps which coincide with the research topics of this dissertation.

In Chapter 3, a conformal TA with a beam-steering capability is discussed. The overall design of the conformal TA is provided, including the element development, TA prototype simulation and measurement. Besides, a method of beam steering of conformal TAs is proposed and validated by simulation and experiment.

In Chapter 4, a high-efficiency conformal TA with ultra-thin dual-layer Huygens elements is presented. A detailed element design procedure is developed based on Huygens metasurface theory. A cylindrically conformal TA employing the proposed element is simulated and analysed. As a verification, the prototype is fabricated and measured.

In Chapter 5, an innovative technique is introduced to achieve UWB planar and conformal TAs. The details for connected-array element designs are provided and applied to a planar TA. Then, a conformal TA based on the developed element is simulated and analysed. Both of these two prototypes are validated experimentally. Finally, a discussion on the feed source for both TAs is presented.

In Chapter 6, a design methodology for high-performance multibeam shaped TAs is developed. The design procedures are introduced and analysed, which are verified through simulations. For experiments, a prototype operating at a mm-wave band has been designed, fabricated and measured, and the results from simulation and measurement are compared.

In Chapter 7, a conclusion is dawn. Potential challenges and future work in this research area are discussed.

## 1.3 Statement of Contributions

In this dissertation, advances on conformal TAs are presented based on the research progress that the author has made during her PhD study. The design concepts and implementations of various conformal TAs are discussed and provided in details. More specifically, her contributions are listed as below.

1. A thin conformal TA is presented and its beam-steering function is realized. The proposed design can switch the beam to ±15°, ±10°, ±5°, and 0° with a stable

realized gain, which has been verified and demonstrated from measurement results. This design is among the earliest findings of successfully implemented conformal TAs in practice. Some early works in this area only demonstrated preliminary simulation results. The developed TA and its beam steering may find wide applications in communication systems where conformal structures are demanded.

2. Huygens metasurface theory is employed in conformal TAs to develop an ultra-thin and low-transmission-loss array element in order to meet the low-profile demand for conformal implementations. It successfully addresses the challenges associated with conformal TAs, i.e., the array usually has a very low efficiency (less than 40%) due to the use of ultra-thin elements. In the proposed design, the measured aperture efficiency of a conformal TA is obtained as 47% with a $0.017\lambda_0$ overall thickness. To the best of the authors' knowledge, this is the first conformal TA with the thinnest element and a high aperture efficiency ever reported.

3. A TA element based on the connected slot-bowtie is developed for UWB operations, which can be applied to both planar and conformal TAs with stable boresight radiation patterns in a 96% fractional bandwidth. The measured efficiencies are found to be higher than other reported planar UWB TAs. The proposed UWB planar and conformal TAs can be employed for bandwidth hungry applications such as radio telescopes, satellite communications, and advanced radar systems.

4. An elliptical cylindrical transmitting surface is developed for multibeam TAs at a mm-wave band. In contrast to other reported multibeam TAs, it can achieve a much larger beam coverage and a low scanning loss without sacrificing the aperture efficiency. Moreover, this is the first reported shaped TA at higher mm-

wave frequencies. To date, most published shaped TAs operate at up to 30 GHz. As 5G and beyond systems move up to higher frequencies, it is imperative to develop antennas operating at higher mm-wave bands. To the author's knowledge, the proposed design is one of the very few shaped TAs working in E-band with a high gain.

## 1.4 List of Publications

The list of publications on journals and conferences is given below. It includes both published and accepted papers.

**Journals**

1. Pei-Yuan Qin, Li-Zhao Song, and Y. Jay Guo, "Beam steering conformal transmitarray employing ultra-thin triple-layer slot elements," *IEEE Trans. Antennas Propag.,* vol. 67, no. 8, pp. 5390-5398, Aug. 2019.

2. Li-Zhao Song, Pei-Yuan Qin, and Y. Jay Guo, "A high-efficiency conformal transmitarray antenna employing dual-layer ultra-thin Huygens element," *IEEE Trans. Antennas Propag.,* vol. 69, no. 2, pp. 848-858, Feb. 2021.

3. Li-Zhao Song, Pei-Yuan Qin, Stefano Maci, Y. Jay Guo, "Ultrawideband conformal transmitarray employing connected slot-bowtie elements," *IEEE Trans. Antennas Propag.,* vol. 69, no. 6, pp. 3273-3283, Jun. 2021.

4. Li-Zhao Song, Pei-Yuan Qin, Shu-Lin Chen, Y. Jay Guo, "An elliptical cylindrical shaped transmitarray for wide-angle multibeam applications," *IEEE Trans. Antennas Propag.,* vol. 69, no. 10, pp. 7023-7028, Oct. 2021.

5. Pei-Yuan Qin, Li-Zhao Song, Y. Jay Guo, "Conformal transmitarrays for unmanned aerial vehicles aided 6G networks," *IEEE Communications Magazine*, accepted, 2021.

**Conferences**

1. Li-Zhao Song, Pei-Yuan Qin, and Y. Jay Guo, “Conformal transmitarray and its beam scanning,” *2019 International Symposium on Antennas and Propagation (ISAP)*, Oct. 2019.

2. Li-Zhao Song, Pei-Yuan Qin, Yan-Hui Liu, and Y. Jay Guo, “Dual-layer Huygens element based conformal transmitarray with a high-efficiency,” *2020 IEEE Asia-Pacific Microwave Conference (APMC)*, Dec. 2020.

3. Li-Zhao Song, Pei-Yuan Qin, and Y. Jay Guo, “A review on conformal transmitarrays,” *15th European Conference on Antennas and Propagation (EuCAP)*, Mar. 2021.

# Chapter 2: Background & Literature Review

This chapter provides a fundamental theory and some conventional methods for planar TA designs. It also describes the state-of-the-art research progress for both planar and conformal TAs.

## 2.1 Introduction of TAs

### *2.1.1 Basic concept*

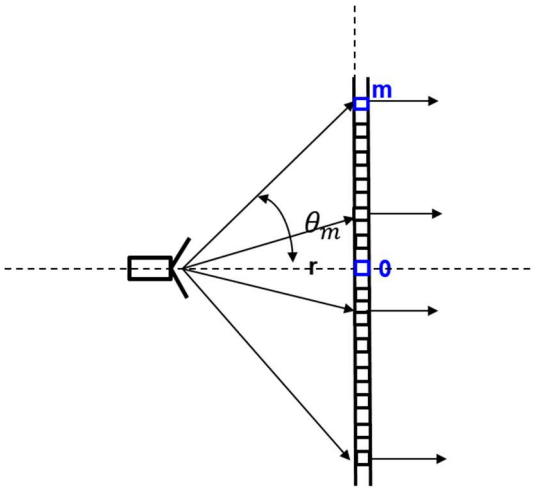


Fig. 2-1 Sketch of a TA.

TAs, composed of a planar transmitting surface and one or multiple feed sources as shown in Fig. 2-1, have been researched substantially due to their combined merits from both lens and microstrip phased array antennas, i.e., high gains, low profiles, adjustable radiation performance and easy fabrications, etc. The transmitting surface of a TA consists of a number of artificially arranged antenna elements in accordance to the desired phase distributions along the surface. It is calculated to compensate for different spatial phase delays at different elements to transform the spherical phase front from the feed

source into a planar phase front. Consequently, the transmitted radiation pattern usually possesses a narrow beamwidth with a high gain.

As a comparison, lens antennas can realize the conversion of spherical-to-planar wave fronts as well [16]-[17]. A typical topology of a bi-convex lens antenna is given in Fig. 2-2. The feed source is located at the focal point of one side, and a planar transmitted wave can be obtained in the other side. It is analysed with the refraction mechanism from geometrical optics, where the lens shape/curvature is elaborated for the desired refraction index. The lens antennas can function well within a wide frequency bandwidth, and are suitable for high-frequency applications. However, at lower microwave bands, especially at less than 3 GHz, the antennas would be heavy and bulky, resulting in complicated and costly manufactures.

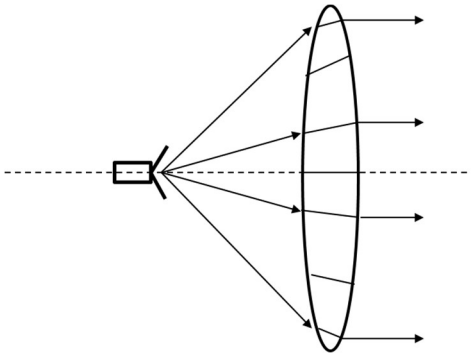

Fig. 2-2 Topology of a conventional bi-convex dielectric lens.

Another typical method for wave manipulations is using microstrip phased arrays [18], where specific feed networks are employed to excite each antenna element with desired amplitude and phase values, as illustrated in Fig. 2-3. Compared to the spatial-feed TAs, the microstrip phased arrays will increase the antenna complexity and transmission loss owing to the inherent drawbacks of the feed networks.

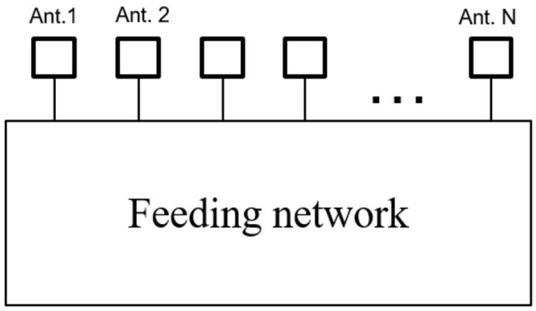


Fig. 2-3 Schematic of a phased array.

Therefore, by exploiting the spatial-feed approach and low-profile microstrip element models, TAs have the advantages of both lens and phased array antennas, and avoid most of their disadvantages, making them outstand in wireless communications and sensing applications.

### *2.1.2 Design methods of TA element.*

As illustrated in Fig. 2-1, each element along the TA surface is individually designed to compensate for the wave path difference from the feed source. With a focal length denoted as *r*, the transmission phase of the *m-th* element $\varphi_m$ is calculated with (2-1).

$$\varphi_m = \varphi_0 + r\left(\frac{1}{cos\theta_m} - 1\right) * 2\pi/\lambda \tag{2-1}$$

where $\varphi_0$ is the transmission phase of the centre element, $\theta_m$ is the angle between the wave path to the *m-th* element and the horizontal axis, and $\lambda$ is the wavelength in free space.

It is noticed that the transmission characteristics of element models are crucial to a high-performance TA. Basically, there are two requirements for element synthesis. The first one is to ensure the transmission amplitude of each element ($|S_{21}|$) is as high as possible, with a lowest threshold as -3 dB. Second, the element transmission phase ($\angle S_{21}$) is capable to be varied within 0°-360° in order to enable arbitrary phase compensations along the TA surface.

Based on the current research progress in TAs, the element synthesis methods can be classified into three types with distinct principles, i.e., frequency selective surfaces (FSS), receiver-transmitter antennas and metamaterial structures.

Multi-layer FSS, consisting of multiple printed radiators separated by dielectric materials or air gaps, is the most frequently applied design technique in TAs [19]-[23]. It can easily provide a band-pass characteristic in a desired frequency band with a low transmission loss. The phase variation would be realized from physical dimension adjustments. For example, in [19], a multi-layer FSS element adopting dual-resonant double-square rings with four identical layers was developed, as shown in Fig. 2-4. The inner square ring patch will resonate as a stopband filter at a higher frequency, while the outer one will resonate as a stopband filter at a lower frequency, thus leading to a wide passband between them as the transmission region. The cut-off frequency points at lower and higher bands are determined by the widths of the inner and outer rings, respectively. A 360° phase range is covered by tuning the dimensions from both rings with a low transmission loss. By applying this element into a TA prototype, a wide 1-dB gain bandwidth of 7.5% and a high aperture efficiency of 47% are obtained.

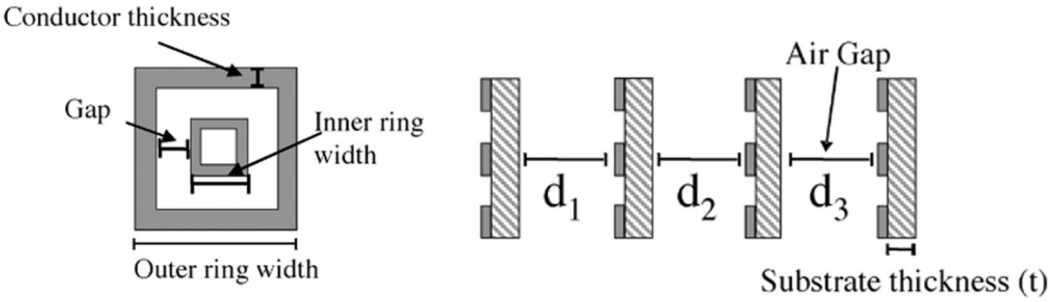


Fig. 2-4 The element model of TAs reported in [19].

Another typical element type for TAs is the receiver-transmitter model, which mainly contains three components, namely, one bottom layer of a printed patch antenna as the receiver, one top layer of a printed patch antenna as the transmitter, and a transition

structure for energy coupling between the receiver and transmitter. The phase variation mechanism could be integrated in the transition section, e.g., strip-lines/aperture coupling slots with variable lengths [24]-[26]. As given in Fig. 2-5, two parallel resonant patches on the two outer surfaces are employed as the receiver and transmitter separately. Two slotted ground planes and a strip-line layer are added between two patches for the aperture coupling. This type of antenna element has the potential of operating in a wide bandwidth due to a true-time-delay phase tuning. However, it may cause large inter-element spaces in TAs in order to accommodate longer strip-lines/slots for large phase compensations.

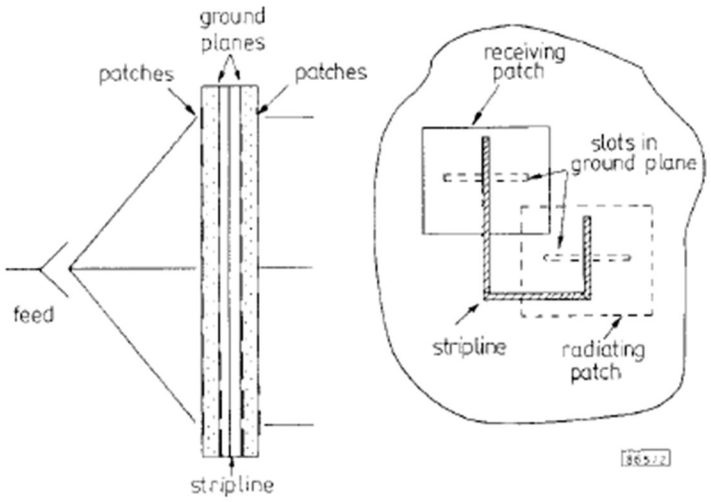


Fig. 2-5 Aperture-coupled microstrip patch element proposed in [25].

With the receiver-transmitter principle in element designs, the phase variation could also be realized from dimension variations or element rotations of the transmitter and receiver patches. For example, as proposed in [27], an asymmetric element model based on antenna-filter-antenna structure was reported with the capability of providing an up-to-360° continuous phase shift in the transmitted wave as the patches are rotated. The element schematic is shown in Fig. 2-6. The shifted transmission phase is twice the amount of the element rotation angle. It is noticed that this element operating mechanism

is for converting a clockwise circular-polarized (CP) wave to an anti-clockwise CP wave, and it can provide a less than 0.5 dB insertion loss at 20.5 GHz.

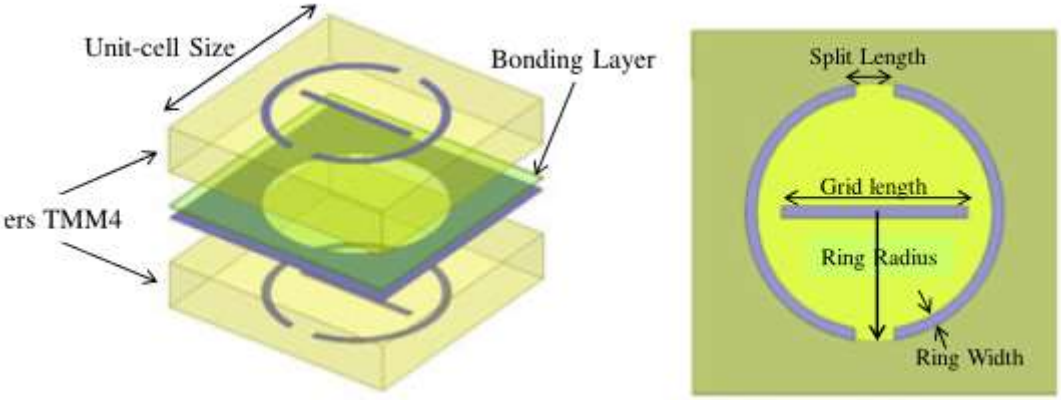


Fig. 2-6 The three-dimensional structure and its top/bottom layer of element developed in [27].

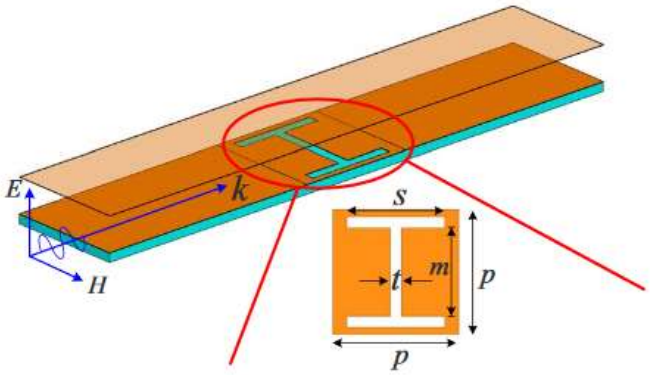


Fig. 2-7 The complementary I-shaped metamaterial reported in [28].

The third approach on element synthesis for TAs is applying metamaterial transformations, where effective medium theory is usually referred to. Its analysis and design process are similar to the traditional lens antennas. As presented in [28], a complementary I-shaped resonant metamaterial is designed at 10 GHz, with its element model shown in Fig. 2-7. The relationships between the element geometry and the effective permittivity and permeability are simulated, which are then combined with

Luneburg lens design techniques for a 2-D planar broadband low-loss array model with a transmission function.

## **2.2** Low-profile TAs

In order to satisfy the phase compensation requirements, elements are expected to cover a 360° transmission phase range with an acceptable transmission loss. It should be noted that it is very difficult to achieve this goal by using only one or two metal layers. It is reported that at least three layers of FSS are needed to accomplish the sufficient phase shift range [29]. Employing this technology, various antenna elements are developed for TAs, including a three-layer spiral dipole element [4], a four-layer double hexagonal ring elements [21], three-layer orthogonal dipoles [22], and multi-layer subwavelength true-time-delay elements [30]-[31]. Unfortunately, one potential drawback of this technology is the relatively high profiles of antenna elements, which are usually more than 0.5 $\lambda_0$ ($\lambda_0$ is the wavelength in the free space).

Efforts have been devoted to reduce the profile of the TA elements while still achieving the required 360° phase range. In [6], a three-layer bandpass FSS element is presented with a profile of 0.36$\lambda_0$. Another typical three-layer element with a thickness of 0.22$\lambda_0$ is demonstrated. It consists of a split circular ring connected by a narrow strip in the middle layer and two polarizers in the upper and bottom layers [5], as given in Fig. 2-8. The middle patch layer is positioned at 45° with respect to x-axis, providing a polarization conversion between the incidence and transmission waves, and its parameters are swept for variable transmission phases. The two polarizers on the outer surfaces are applied to improve the transmission efficiency. A total phase coverage of around 380° is reached with a low transmission loss.

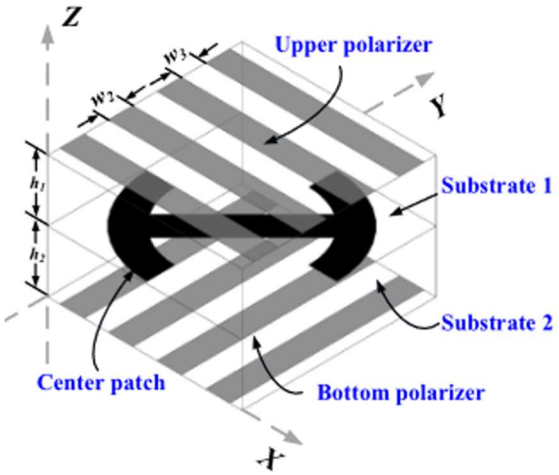


Fig. 2-8 3-D view of the element in [5].

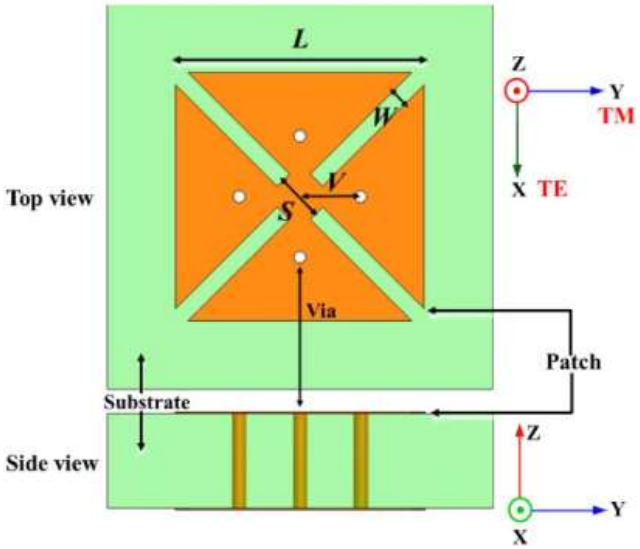


Fig. 2-9 Double-layer TA element model reported in [32].

In [32], a two-layer element is shown consisting of modified Malta crosses printed on a dielectric substrate with four vertical-plated through vias, as illustrated in Fig. 2-9. Two Malta cross patches on the top and bottom layers of the substrate act as transmitting and receiving components, respectively. The four vias are added between them to direct guided wave signals for energy coupling. The thickness of the element is $0.43\lambda_0$, and the patch length $L$ is adjustable for desired transmission phases, providing a less than 1-dB transmission loss for the 80% of obtainable phase range. Besides, a two-layer element

with two coplanar patches printed on two sides of a printed circuit board (PCB) is proposed in [33], That can achieve a 180° phase range. The patches are connected by a few through vias. The element thickness is 0.203 mm, which is $0.05\lambda_0$ at 77 GHz.

## **2.3** Beam-scanning TAs

In the last few decades, beam-scanning antenna arrays have been well researched based on various antenna types, e.g., phased array antennas, leaky wave antennas, reflectarray antennas (RAs) and TAs, etc. They can enable dynamic beam scanning without re-arranging antenna apertures, thereby making them attractive and essential for high-speed wireless communications and sensing systems. Since the beam scanning of TAs may not require complex feed networks, it will reduce the fabrication cost and system losses, particularly at high frequency bands [9].

To date, some research results on reconfigurable beam-scanning TAs have been reported, and most of them employ active components, e.g., PIN diodes [34]-[36] or varactor diodes [10]-[11], [37], to control the operating status of TA elements in order to obtain different transmission phase values. Instead of a continuous 360° phase range of the traditional element, the reconfigurable one usually shows a quantized 360° coverage.

As developed in [36], a 1-bit TA element is composed of a patch antenna as the receiver, a magnetic dipole antenna as the transmitter, and a metallized via for wave coupling, as depicted in Fig. 2-10. Two PIN diodes are loaded on the transmitter for transmission phase reconfigurations. By applying a specific bias voltage, the PIN diodes will be turned on/off so that a 180° phase difference can be obtained. In the final TA implementation, the radiation beam is scanned from 0° to 60° with a 3.6-dB scanning loss along E-pane.

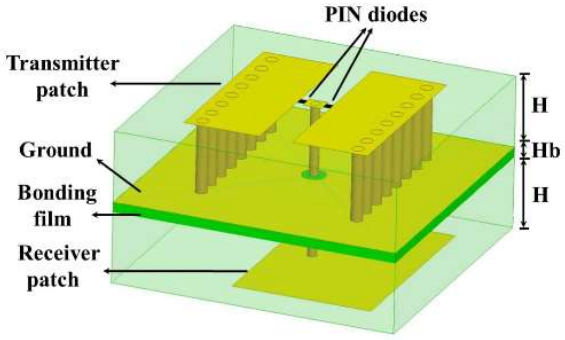


Fig. 2-10 1-bit reconfigurable TA element in [36].

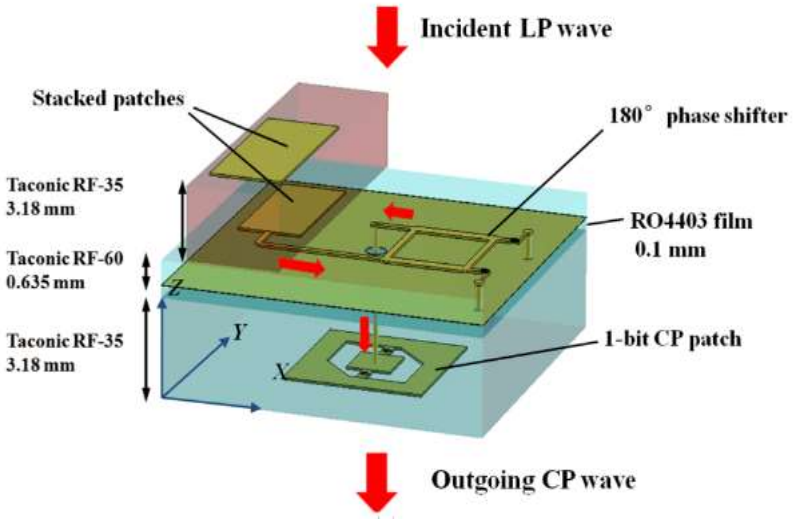


Fig. 2-11 Circular-polarized reconfigurable TA element proposed in [10].

Another novel receiver-transmitter model for reconfigurations with varactor diodes is presented in [10], as displayed in Fig. 2-11. Two stacked patches are utilised as the receiver of a linear-polarized incidence wave, and a circular-polarized patch is designed as the transmitter with two PIN diodes integrated. A four-port 180° phase shifter is added in the middle layer to couple the guided wave signals from the receiver to the transmitter. Varactor diodes are loaded to two ports, so that the transmission phase after the phase shifter can be tuned continuously within 0°-180°. Besides, the PIN diodes on the transmitter can provide a 1-bit differential phase shift, i.e., 0°/180°. Finally, the element realizes a 360° continuous phase coverage with a less than 2-dB transmission loss. By

employing the proposed element into a TA design, a beam steering range of ±45° is obtained with an about 1.7-dB scanning loss at the maximal angles.

## **2.4** High-efficiency TAs

Previously, we discussed about the profile-reduction techniques for TAs, which raise another concern, i.e., aperture efficiency. The aperture efficiency of TAs is defined as the ratio of the gain and the maximum directivity of the array aperture, the latter obtained as $4\pi$ times the physical aperture area on square wavelength. It is found that there is always a trade-off between TA thickness and its aperture efficiency. The authors in both [38] and [39] use multi-layer slot elements and realize 55% aperture efficiencies of TAs. The applied element model from [39] is shown in Fig. 2-12 as an example, three metal layers are separated with two ¼ $\lambda_0$ air gaps. In a dual-band TA design [22], aperture efficiencies of 45% and 41.3% are achieved at 12.5 GHz and 14.25 GHz, respectively, by applying a three-dipole element. Besides, a novel element arrangement method is introduced in [40], where elements with varied thickness are placed on the aperture to increase the aperture efficiency to 62%. However, due to the employment of quarter-wavelength air gaps between adjacent layers to reduce the element transmission loss, all the abovementioned models show high profiles as more than $0.5\lambda_0$. Therefore, the TA element with a balanced aperture efficiency and overall thickness is highly demanded.

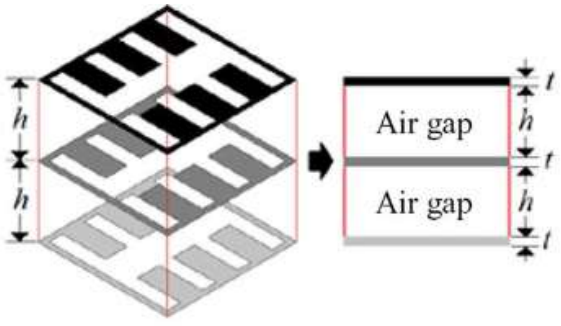


Fig. 2-12 Three-layer slot TA element developed in [39].

In [5], a high-efficiency TA is developed using a three-layer element with a thickness of $0.22\lambda_0$. The peak aperture efficiency of the TA is obtained as 40.7%. As reported in [12], a three-layer metallic element without air gaps shows a low profile of 1mm ($0.033\lambda_0$). As depicted in Fig. 2-13, the top and bottom patch layers are the same with cross strips inserted in a cross slot, while the middle layer has a different shape with T-slots. This element is finally employed in a TA providing a 36% aperture efficiency. In [13], a thin TA with a more than 30% aperture efficiency is developed using three-metal-layer antenna elements with a thickness of 1.6 mm ($0.07\lambda_0$ at 13.5 GHz).

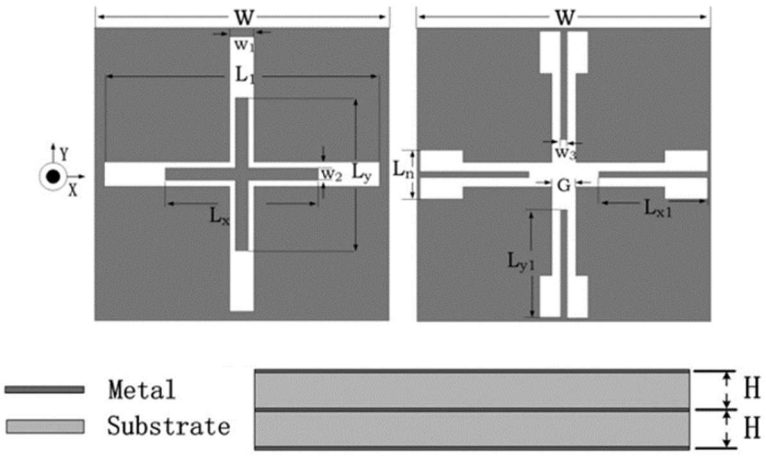


Fig. 2-13 Element configuration designed in [12].

## 2.5 Wideband TAs

For wireless communications and sensing systems, a wide operating bandwidth is also essential to facilitate high-data-rate connections and to enable stable performance in multiple channels.

In the last two decades, there have been many interesting technologies reported to enhance the bandwidth of planar TAs by employing multi-layer elements with FSS structures [6], [20], [41]-[42], true-time-delay lines [25], [30], [43]-[44], or two

orthogonally oriented modes [5], [45]. A typical prototype of TA can achieve a 1-dB gain bandwidth of 56% from 9 GHz to 16 GHz [5].

As reported in [41], a triple-metal-layer element is designed with two identical cross-slots on the top and bottom layers. One pair of square-ring patches with different lengths are printed on the intermediate layer, as shown in Fig. 2-14. Due to two different resonances produced from the cross slots and the square rings, the coupling effects can be improved compared to the traditional FSS elements with multiple identical layers. As a validation, the final implemented TA shows a 16.8% (11.5-13.6 GHz) 1-dB gain bandwidth from measurement.

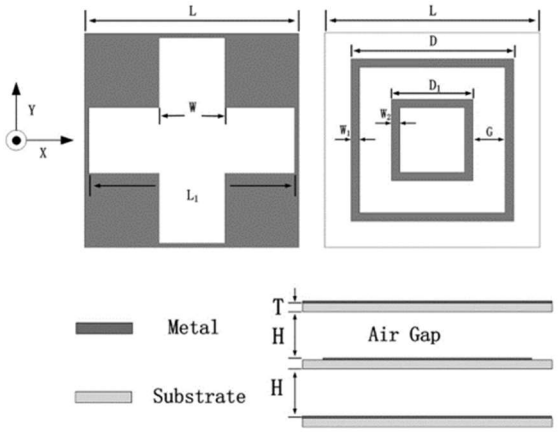


Fig. 2-14 The wideband triple-layer element reported in [41].

By applying the true-time-delay-line method in [30], two types of potential TA elements are developed as metallo-dielectric and all-dielectric structures separately. Their models are shown in Fig. 2-15. The metallo-dielectric model consists of several capacitive patches separated by dielectric substrates, while the all-dielectric model is composed of high $\varepsilon_r$ (permittivity) and low $\varepsilon_r$ dielectric substrates cascaded sequentially. Both of these two structures can be modelled and analysed with a low-pass microwave filter circuit, providing linear phase responses in a wide bandwidth. Eventually, the designed TAs with two types of element achieve 50% and 40% bandwidths, respectively.

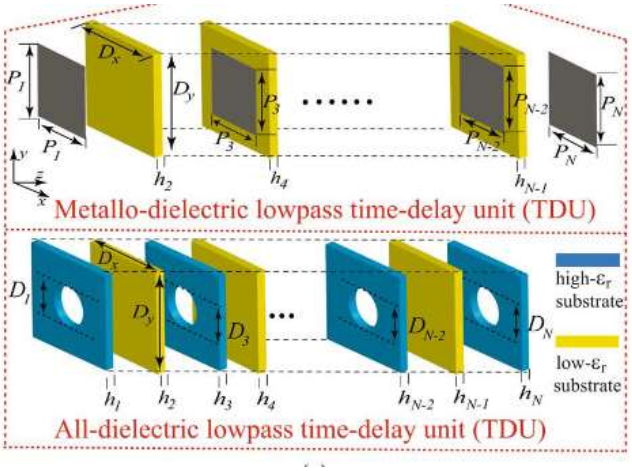


Fig. 2-15 Topologies of two true-time-delay elements presented in [30].

In order to further enlarge the bandwidth, planar TAs employing tightly coupled antenna elements are presented [46]-[47]. Tightly coupled arrays are based on the concept that electrically connected arrays using dipoles or slots can achieve almost an infinite bandwidth. It is well known that with the presence of a ground plane, the bandwidth of connected arrays will be reduced significantly without material loadings [48]. As a result, tightly coupled antenna arrays which utilize capacitance couplings between the elements to compensate for the effects of the ground plane are emerging as one successful UWB antenna array technology [49]-[50]. Here it defines UWB antennas as those with a fractional bandwidth greater or equal to 100%. It should be pointed out that one potential disadvantage for the tightly coupled UWB arrays reported to date is that transmission-line-based feed networks are usually required. They can be very lossy and bulky, especially at mm-wave bands or higher. Therefore, TAs or RAs leveraging both the tightly coupled array technology and spatial feeds are emerging as an attractive solution for high-gain antenna alternatives. In [46], a planar TA using tightly-coupled-dipole elements realizes a more than 100% bandwidth, i.e., from 3 GHz to around 9.5 GHz. The element model is shown in Fig. 2-16, which has both horizontally printed dipoles and vertically printed delay lines. The length of the delay line can be adjusted to compensate

for spatial phase delays from the feed source to the TA surface within an ultra-wide band. The aperture efficiency of the final implemented TA is achieved from 20% to 46% with a peak gain of about 20.6 dBi. In [47], a tightly coupled dipole TA can operate from 9.5 GHz to 16 GHz with an efficiency of around 30%. For these UWB TAs, the bandwidth is defined as the operating band where stable radiation patterns without distortions are obtained.

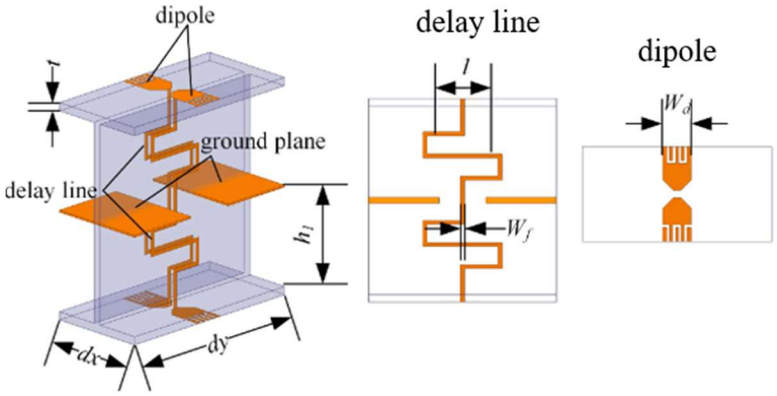


Fig. 2-16 Geometry of the tightly coupled dipole TA element proposed in [46].

## 2.6 Multibeam TAs

Multibeam antennas, which can provide a wide beam coverage to serve a number of distributed users simultaneously, have attracted considerable attention from both academia and industry as a good candidate in satellite communications, radar detections and MIMO systems. Instead of exciting single feed source to steer the beam towards different directions, multibeam realizations require multiple feeds working simultaneously to multiple directions.

Compared with the existing digital/hybrid beamforming technologies [51]-[52], passive or analogue multibeam antennas offer several significant commercial advantages, including lower manufacturing costs, reduced power consumptions and more deployment flexibilities. The existing passive multibeam antennas include those based on lens [53]-

[55], TAs [56]-[58], RAs [59]-[61] and beamforming circuits, e.g., Butler-matrix-based antennas [62]-[63]. Among them, TAs/RAs have their own merits of achieving high gains without requiring lossy transmission-line-based feed networks. Furthermore, compared with RAs, TAs do not have the issue of feed blockages as their feeds and main beams are located on different sides of the apertures. Motivated by these advantages, substantial research efforts have been devoted to multibeam TAs.

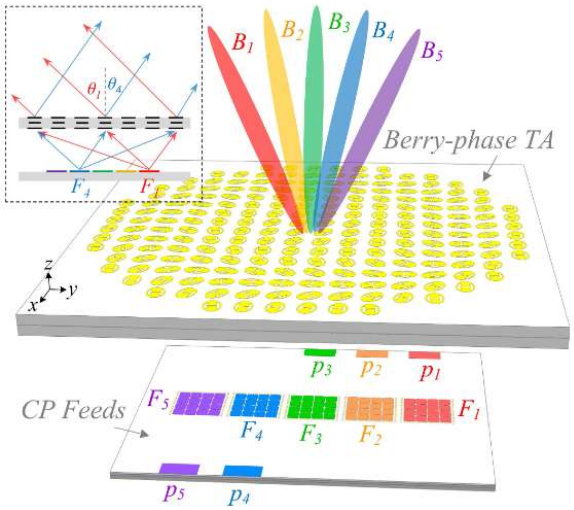


Fig. 2-17 Configuration of multibeam TA in [65].

One popular technology is to utilize a bifocal phase compensation method initially presented in RAs [64]. In [65], circularly polarized multibeam TAs are developed at 26 GHz, generating five pencil beams that cover a range of ±33° with a scanning loss of 1.2 dB. The configuration is sketched in Fig. 2-17. A peak boresight gain is obtained as 22.2 dBic. In [66], a seven-beam transparent TA at 28.5 GHz is presented. It has a peak boresight gain of 25 dBi covering a range of ±30° with a scanning loss of 3.5 dB. Another technology is to develop metamaterial-based planar multibeam TAs. A multibeam TA using Jerusalem cross elements is demonstrated at 28 GHz, achieving an angular coverage of ±27° with a scanning loss of 3.7 dB [67]. The maximum gain is 24.2 dBi. A multibeam folded TA is demonstrated in [68] with five beams covering up to ±10° at 30 GHz.

Besides, by using a sliding transmitting aperture or feed, circularly polarized mechanical beam switching TAs are demonstrated at Ka band [69]-[70]. An asymmetric beam scanning range of 0°-50° is achieved for satellite-on-the-move (SOTM) ground terminal applications. The beam scanning mechanism is shown in Fig. 2-18, where the lens can be slid horizontally with a constant focal length to steer the radiation beam along the elevation plane, and be rotated around a vertical axis to realize beam steering along the azimuth plane. The beam steering methods could be employed to achieve multibeam radiations when multiple feeds are implemented. In [71], a linear multibeam TA is designed based on a sliding aperture concept at 5.8 GHz, where eight beams are produced with a 3-dB beam coverage of ±42°. Since it is a linear array, a medium gain up to 13.9 dBi is achieved.

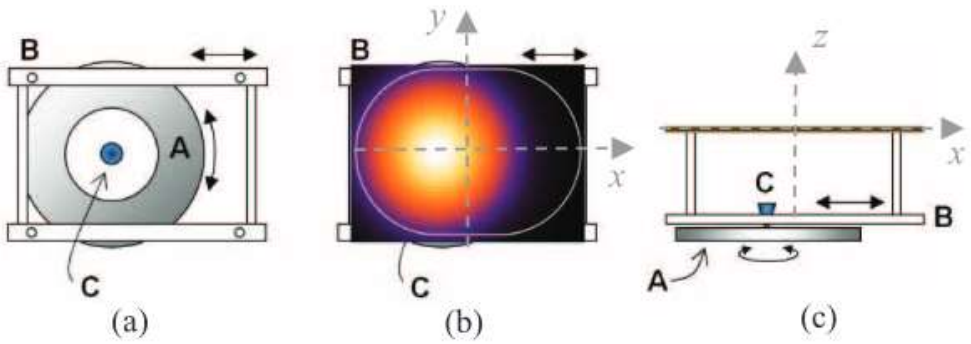


Fig. 2-18 Schematic of lens mounting structure reported in [69].

## **2.7** Conformal TAs

In response to the increasing demands for wireless connectivity, wireless communication technology is moving towards the integration of terrestrial networks with airborne and space borne networks. For airborne platforms with curved shapes, e.g., UAVs and aircrafts, conventional planar TAs are heavy and bulky, and usually protrude from the exterior of the platforms. It increases drag and degrades the aerodynamics, thus leading to reduced vehicle speeds and energy efficiencies. On the other hand**,** conformal high-

gain TAs, which can be designed to follow the shapes of various mounting platforms, are excellent for aerodynamics and are light weight, low profile and low cost.

Unfortunately, most of the current reported TA elements are not suitable for conformal designs. As discussed before, they either consist of multiple thick layers of FSS or need metallic vias connecting top and bottom layers of the elements. Considering the current manufacturing technology, it is very difficult to fabricate a curved structure with several metal layers separated by substrates. Therefore, only few works have been reported for conformal TAs, and only preliminary simulation results are available [72]-[74].

As reported in [72], a quad-layer printed Malta-cross element is applied to cover a 360° phase range, leading to an overall thickness of 17 mm ($0.77\lambda_0$ at 13.5 GHz). The final configuration of a conformal TA is shown in Fig. 2-19. It is constructed in a 3-D simulation software, showing a simulated aperture efficiency of 49.4% and a 1-dB bandwidth of 7.3%. It should be noted that it is very difficult to implement the proposed conformal TA in practice as its element thickness is too large.

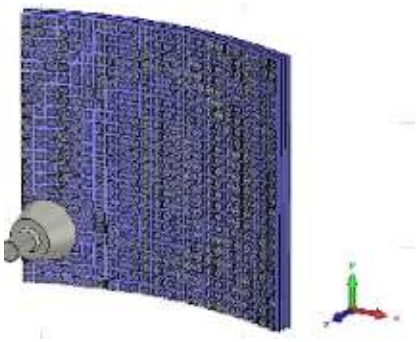

Fig. 2-19 Conformal TA model in [72].

Another conformal TA is simulated in [74], where three planar TA panels are combined on a conformal platform, as displayed in Fig. 2-20. The conformal contour is designed to enhance the beam steering capability of planar TAs with a reconfiguration on the phased-array feed source.

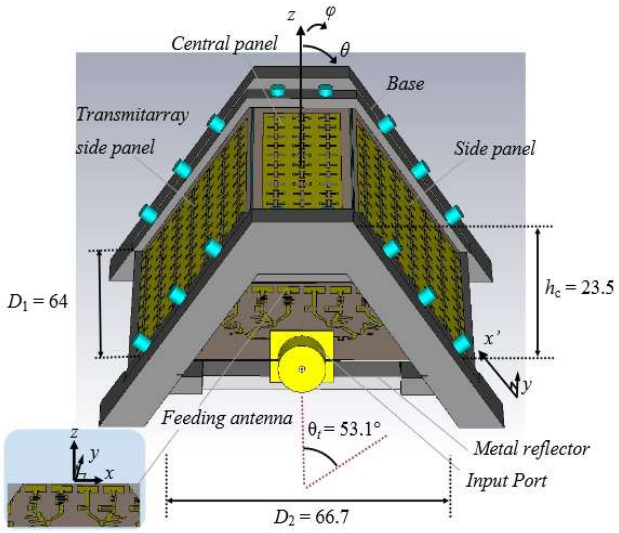


Fig. 2-20 Conformal TA structure in [74].

## 2.8 Summary

Last two decades have witnessed substantial research efforts and progress in improving the performance of planar TAs, including low profile, high efficiency, wide operating bandwidth, beam scanning and multibeam radiations.

In light of the above literature review and discussions, it is found that the research on conformal TAs is still in its infancy. Most of the current technical developments on TA designs are targeted for planar configurations. They cannot be applied directly into conformal structures considering the available fabrication technologies and overall costs. Therefore, innovative techniques on the development of conformal TAs are demanded to bridge this gap for the advancement of conformal TAs.

# Chapter 3: Beam-Steering Conformal Transmitarray Employing Thin Triple-Layer Slot Elements

In this chapter, we firstly report a thin TA element that is suitable for conformal arrays. The element has three layers of square ring slots. Each layer is separated by a distance of only $0.02\lambda_0$ at 25 GHz. Therefore, the entire thickness of the element is about $0.04\lambda_0$ (0.508 mm), making it suitable to be bent and attached to a curved platform. Although the element is very thin, it can achieve a transmission phase range of 330° with a maximum 3.6-dB loss. Secondly, a TA prototype using the proposed element that conforms to a cylindrical surface is designed, fabricated, and measured. Thirdly, we developed a new method to steer the beam of the proposed TA. Instead of simply rotating the entire transmitting surface and the feed source together, only the feed source is rotated at the focal point. A prototype is designed and measured that can steer the beam to 0°, ±5°, ±10°, and ±15°. Good agreement between simulated and measured results is achieved. To the authors' best knowledge, this is the first work ever reported with the experimental verification on conformal TA antennas with beam steering.

The chapter is organized as follows. In section 3.1, the overall design of a conformal TA is presented, including the element design, simulation and measurement of the TA prototype. In section 3.2, a mechanical beam steering method for the proposed conformal TA is described followed by a discussion in section 3.3. This chapter concludes in section 3.4.

## 3.1 Conformal TA Design

### *3.1.1 Element Design*

The TA element used in this work consists of three layers of identical square-ring slots as shown in Fig. 3-1. The width and the length of the slot are *w* and *L*, respectively. The element periodicity is *P* and the overall height is *h*. *w* is chosen to be 0.8 mm and *P* is 5.6 mm. The transmission phase of the element can be varied with *L* in a range of 3.5 mm to 5.41 mm. The three-layer slot element employed has been reported in [75] for a planar multiple-polarization TA. However, the total thickness of the element in [75] is 30 mm, which is more than half of wavelength at its operating frequency. In order to utilize this element for a conformal design, a parametric study of the effect of the height *h* on the transmission coefficient is conducted, which is given in Fig. 3-2. The element is simulated using Floquet method with master-slave boundaries in 3-D electromagnetic (EM) simulation software ANSYS HFSS. When *h* is varied, the other parameters keep unchanged. It can be seen from Fig. 3-2 that the operating frequency goes higher when *h* is reduced and the phase range is reduced with *h*. When *h* equals 6 mm which is 0.5 $\lambda_0$ at 25 GHz, the phase range can cover more than 360°. However, for a 0.254 mm thickness, which is ideal for conformal designs, the phase range decreases significantly. Therefore, a compromise should be made between the thickness and the phase range. It is found that a PCB board, which has a thickness of more than 1 mm, will be easily broken when it is bent. Therefore, in this work, *h* is chosen to be 0.508 mm which is about 0.04$\lambda_0$ at 25 GHz. It is noticed that the stability of $S_{21}$ deteriorates as the thickness *h* is reduced. This is because the resonance of three square-ring slots are affected and the balance between them is broken when the thickness is too small. It can be resolved by adding extra resonant

structures to the metal layer. However, the design complexity will increase considering to balance the resonance between the added structure and the previous square-ring slots.

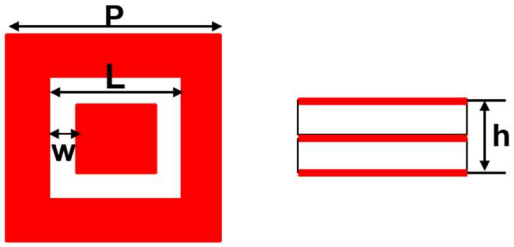


(a) (b)

Fig. 3-1 The proposed FSS element model. (a) Top view. (b) Side view. (Red part is the metal and white part is the substrate)

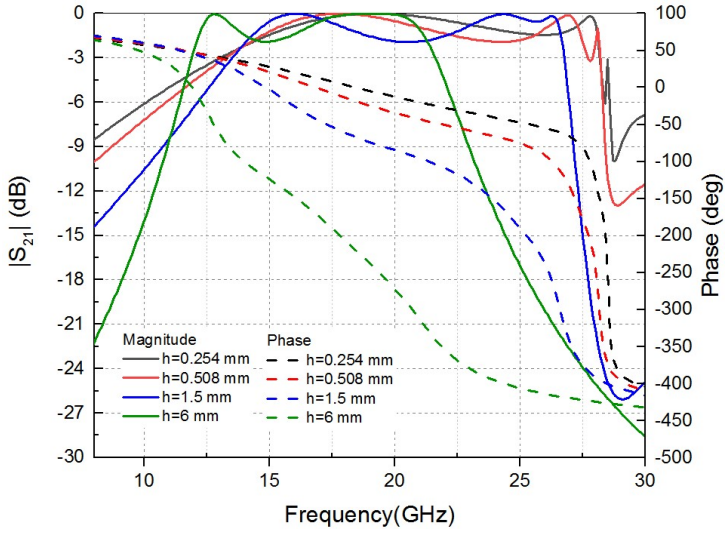


Fig. 3-2 Transmission performance of the planar TA element with L equal to 5 mm at different *h* values.

The above analysis is for a planar triple-layer square ring slot element. As the element is designed for conformal TAs, its transmission coefficient is examined when it is bent with different curvatures. As seen in Fig. 3-3 (a), the three-layer element is bent with different angles α. When α is equal to zero degree, the element becomes a planar one. For the conformal TA in this work, the element is bent with α equal to 7.2°. Fig. 3-3 (b) depicts the amplitude and phase of the transmission coefficient versus the slot length *L*. When *L*

varies from 3.5 mm to 5.41 mm, a transmission phase range of 330° is achieved for the planar element. The transmission amplitude $|S_{21}|$ for most of the points are higher than -3 dB. The worst case is -3.6 dB when $L$ is equal to 5.36 mm. For the bent element model with a small value of α, the phase range and the loss remain almost the same as the planar one. Only when α is extremely large, i.e. 60°, the transmission loss increases slightly, but it is still lower than 3.6 dB. It is interesting to find that the phase range is nearly unchanged even for this large angle. This is because the phase variation is determined by the length of the slot which is not affected by the curvature of the transmitting surface. It should be pointed out that the periodic boundary conditions used in the simulation can only mimic an infinitely large planar surface rather than a cylindrical one. Therefore, there may exist some discrepancies of the element performance between these two surfaces. However, as the bending angle of this work (7.2°) is not that large, the above simulation results can be used as a reasonably accurate reference when calculating phases of the elements.

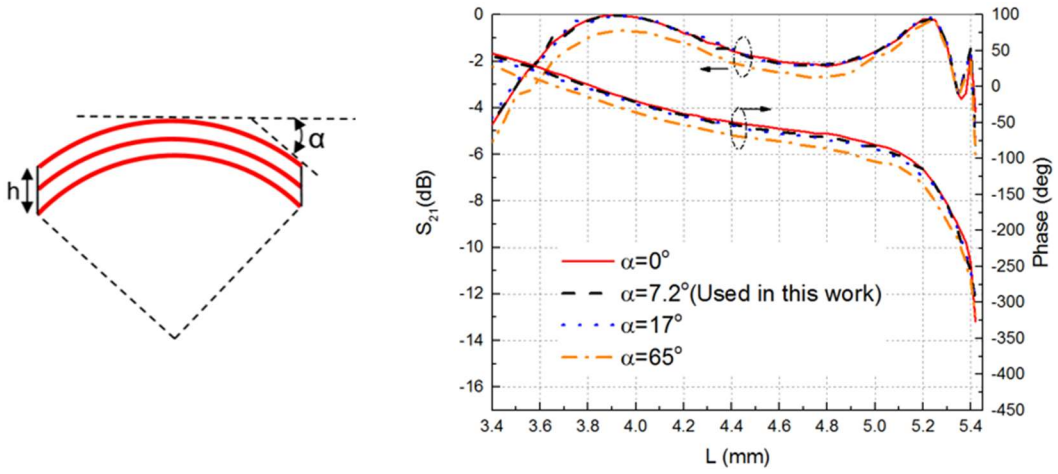


Fig. 3-3 TA element on a curved surface. (a) Element sketch with a bending angle α. (b) Simulated transmission amplitude and phase.

Transmission coefficients of the element are also examined under different incident angles as shown in Fig. 3-4. Here, oblique incidences are examined for the element bent

with α equal to 7.2°. It can be seen that the loss increases with the angle of incidence for *L* between 4 mm and 5.2 mm. When the incident angle is equal to 35° which is the largest one in this TA design, the maximum loss increases to 4 dB when *L* is equal to 5.36 mm. In terms of the phase range, it is almost unchanged for different incident angles. All in all, considering the ultra-thin profile, a 330° phase range and a maximum 4-dB loss at the 35° incidence angle achieved by the element is acceptable for conformal TAs.

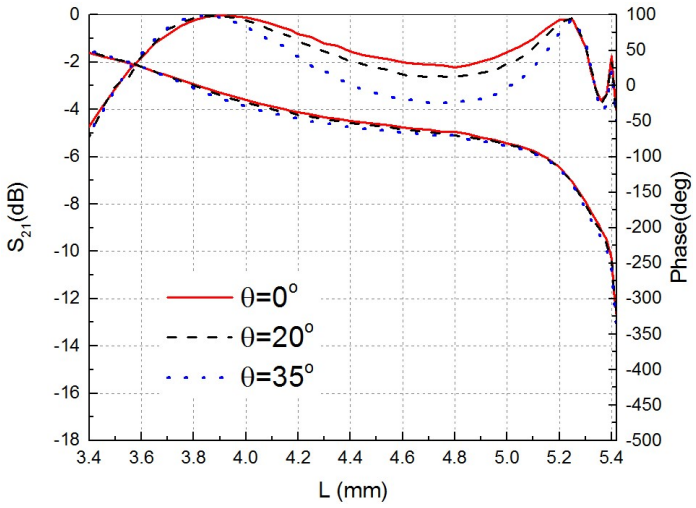


Fig. 3-4 Transmission performance of the curved element with α equal to 7.2° at 25 GHz under normal and oblique incidence.

### *3.1.2 TA Simulation and Measurement*

As known, the transmitting phase of each array element on the surface should be designed to compensate for spatial phase delays from the feed horn to that element, so that a certain phase distribution can be achieved to focus the beam towards a specific direction [3]. Fig. 3-5 (a) and (b) show the 3-D structure and the top view of the conformal TA with a prime focus, respectively.

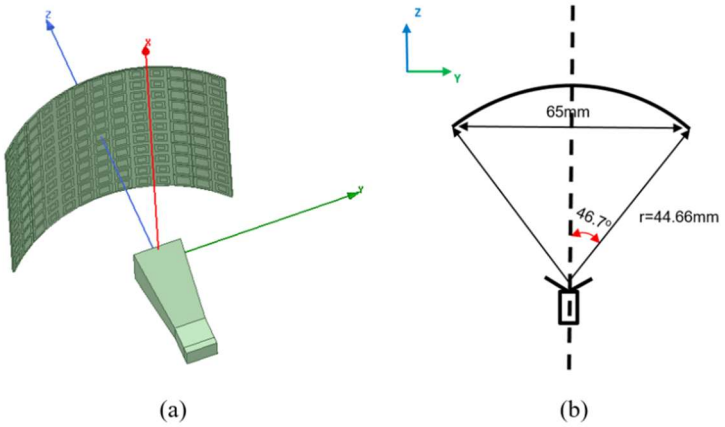


Fig. 3-5 Conformal TA. (a) 3-D structure. (b) Top view.

The feed horn is located in line with the middle of cylindrical TA surface. The unfolded transmitting surface is displayed in Fig. 3-6. It can be seen that there are *m* and *n* elements along *x* axis and *y* axis, respectively. Different colours represent elements with different transmission phase values. Cross sections of the conformal TA along *y0z* and *x0z* planes are illustrated in Fig. 3-7.

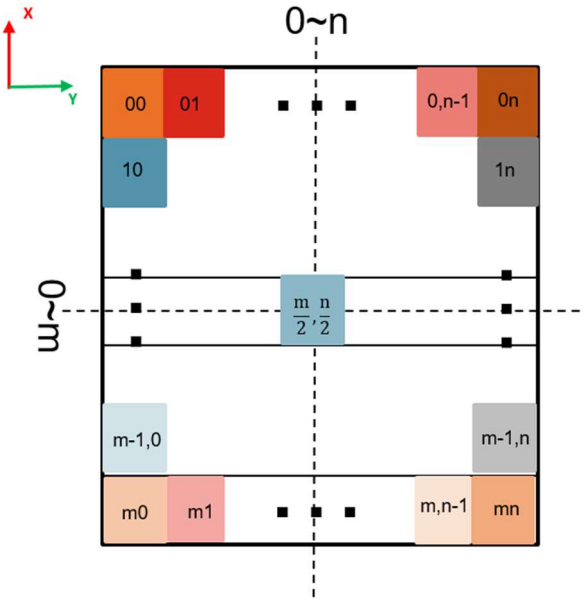


Fig. 3-6 Element distribution of the unfolded conformal TA.

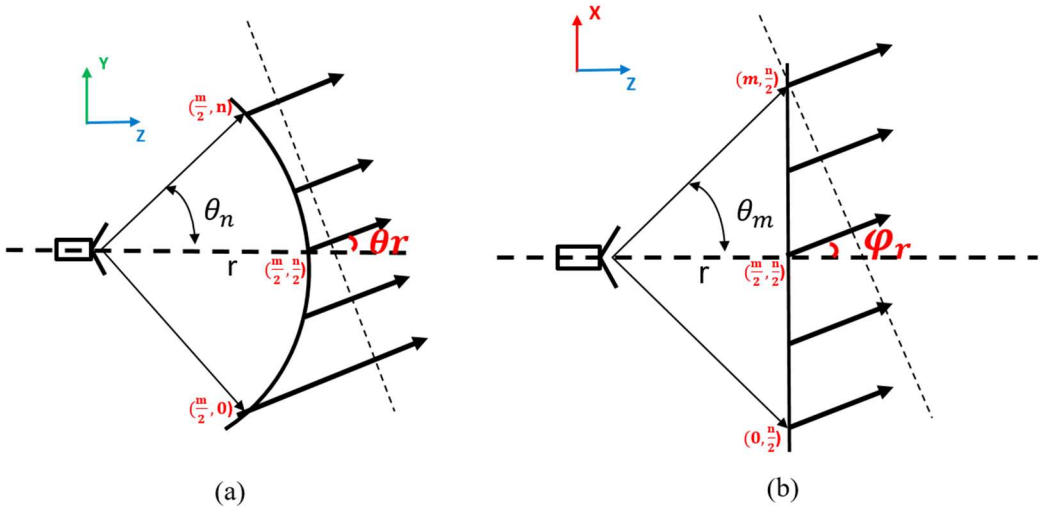


Fig. 3-7 Cross-sectional views of conformal TA model. (a) *y0z* plane. (b) *x0z* plane.

To calculate the accurate compensation phases at different positions on the cylinder, the element phase distribution in the middle curved line along *y0z* plane is considered first. As seen from Fig. 3-7 (a), element phase values on this curved line can be calculated using (3-1). Then these elements will serve as the base for other elements in each column along *x*-axis. For the elements in each column, the phase calculation as shown in Fig. 3-7 (b) is the same as that of a planar TA as they are located along a straight line. For example, for the middle column, its phase can be calculated using (3-2).

$$\varphi_{\frac{m}{2},n} = \varphi_{\frac{m}{2},\frac{n}{2}} + r(\cos\theta_r - \cos(\theta_n - \theta_r)) * \frac{2\pi}{\lambda_0} \tag{3-1}$$

$$\varphi_{m,\frac{n}{2}} = \varphi_{\frac{m}{2},\frac{n}{2}} + r\left(\frac{1}{cos\theta_m} - \tan\theta_m * \sin\varphi_r - 1\right) * \frac{2\pi}{\lambda_0} \tag{3-2}$$

where $\theta_r$ and $\varphi_r$ are radiation angles at *y0z* and *x0z* plane respectively, $\theta_n$ and $\theta_m$ are the half subtended angles of the cylindrical surface along *y0z* and *x0z* plane, respectively, $\varphi_{m/2,n/2}$ is the transmission phase of the centre element, and *r* is the distance from feed point to the centre element, which is chosen as 44.66 mm in this work. $\lambda_0$ is the wavelength at operating frequency in the free space.

Finally, we can obtain the phase $\varphi_{mn}$ for any element as given in (3-3).

$$\varphi_{mn} = \varphi_{m,\frac{n}{2}} + r(\cos\theta_r - \cos(\theta_n - \theta_r)) * \frac{2\pi}{\lambda_0} = \varphi_{\frac{m}{2},\frac{n}{2}} + r\left(\frac{1}{cos\theta_m} + \cos\theta_r - \cos(\theta_n - \theta_r) - \tan\theta_m * \sin\varphi_r - 1\right) * \frac{2\pi}{\lambda_0} \quad (3\text{-}3)$$

### *3.1.3 Simulated and Measured Results*

A conformal TA prototype using the proposed element is designed. It consists of 13×11=143 elements. The cross-sectional size of the transmitting surface is 65 mm × 61.6 mm. A standard gain horn LB-28-10-C-KF from A-INFO is used as the feed source and placed in the centre of the cylindrical surface. The aperture edge illumination is around -10 dB with a half subtended angle of 46.7° for the conformal transmitting surface (as shown in Fig. 3-5 (b)). Each layer of the unfolded transmitting surface was fabricated using a standard PCB technology on low-cost substrates (Dielectric Constant 2.2, tanδ = 0.007). Then the two surfaces are laminated together and attached to a 3-dimentional (3-D) printed cylindrical frame. The whole array is mounted on a frame for antenna measurement purposes. The photograph of the prototype is shown in Fig. 3-8.

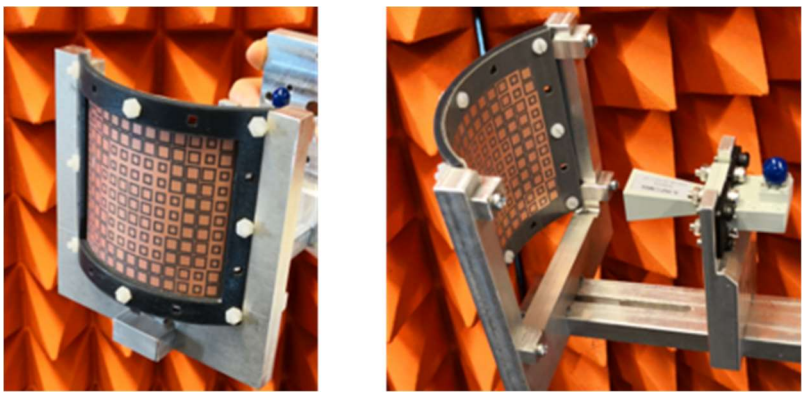

Fig. 3-8 Photograph of the conformal transmittarray prototype.

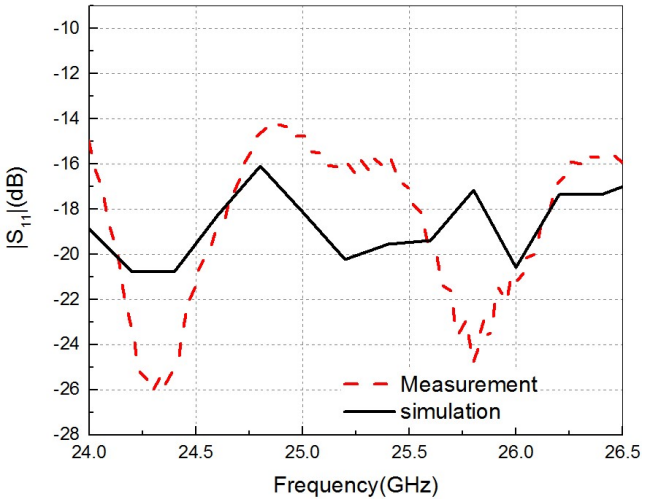


Fig. 3-9 Simulated and measured input reflection coefficients versus frequency of TA.

Fig. 3-9 shows the simulated and measured input reflection coefficients versus frequency of the conformal prototype. As can be seen, the input reflection coefficients are below -10 dB across the frequency band from 24 GHz to 26.5 GHz. Reasonably good agreement between the simulated and measured results is achieved. Far-field radiation patterns were measured using a Microwave Vision Group (MVG) compact range antenna measurement system located at University of Technology Sydney, Australia. Fig. 3-10 shows the simulated and measured E- and H- plane patterns at 25.5 GHz, respectively. Compared to the feed horn antenna which has a gain of 10.6 dBi, the 3-dB beamwidth of the proposed antenna is reduced from 54° to 12° along both planes. The measured cross-polarization level is less than -20 dB. The simulated and measured realized gain values versus frequency are also found and plotted in Fig. 3-11. The simulated peak gain is 20.5 dBi at 25 GHz, while the measured one is 19.6 dBi at 25.5 GHz. The measured 3-dB gain bandwidth is 6.7%. The measured aperture efficiency is 25.1% considering the gain calculated by the aperture cross-sectional size. The low efficiency and the small gain bandwidth are due to the use of very thin element model of the conformal TA. As can be seen from Fig. 3-2, the element's phase curve is sharper when the thickness is smaller.

This leads to large phase compensation errors which may reduce the realized gains of TA and limit its gain bandwidth [29].

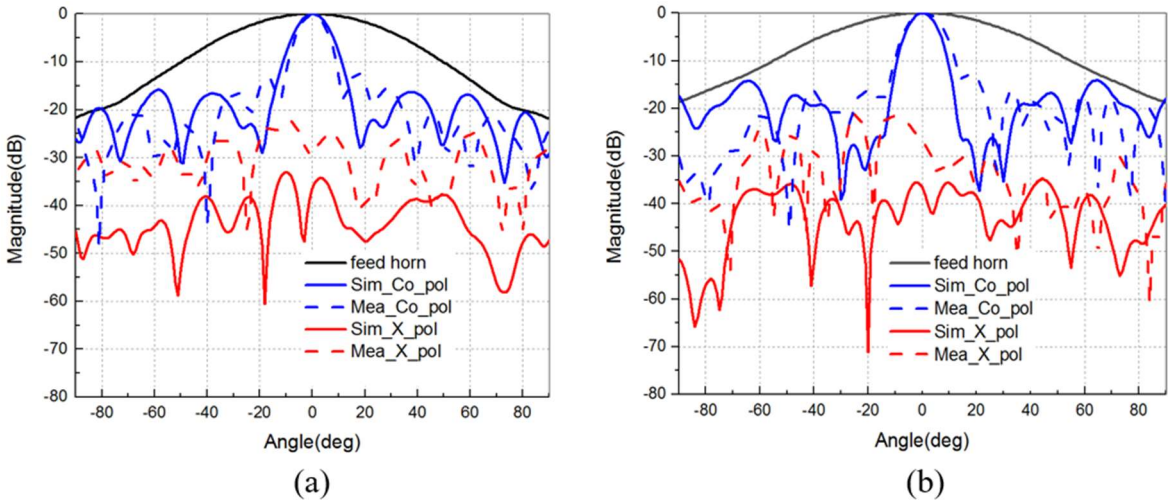


Fig. 3-10 Simulated and measured radiation patterns at 25.5 GHz. (a) E-plane. (b) H-plane.

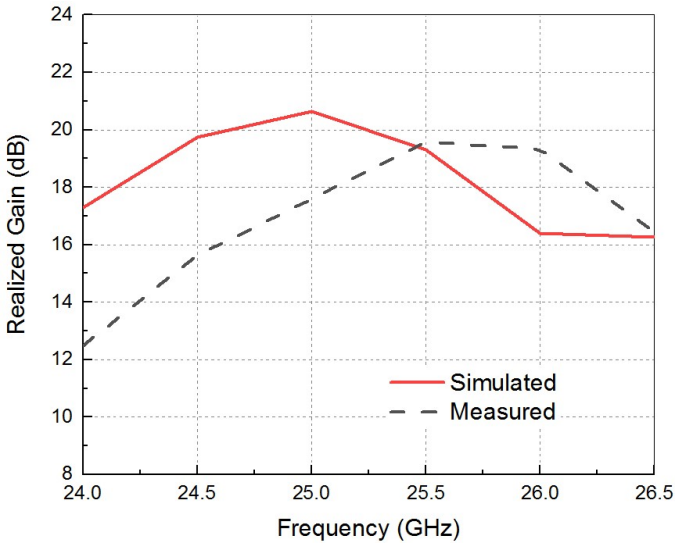


Fig. 3-11 Simulated and measured realized gain values of the conformal TA.

There are some discrepancies in the input reflection coefficients, 2% frequency shift and around 1-dB gain difference of the simulated and measured peak gains. They can be mostly attributed to the following factors. First, there are some inaccuracies in the fabrication process and alignment errors. Second, the PCB board used to fabricate this

antenna is a low-cost one, which could have a varied dielectric constant value and a varied loss tangent value from the datasheet.

To verify the effect of the element thickness on TA aperture efficiency, a TA arranged with a 2.5-mm-thick element is also simulated. It consists of a same number of elements as the previous 0.508-mm-thick TA, which has 13×11=143 elements. Since the optimized element periodicity of the 2.5-mm-thick one has been reduced to 5.13 mm. The cross-sectional size of the transmitting surface is also reduced to 59.5 mm × 56.4 mm. A same standard gain horn LB-28-10-C-KF is used as the feed source and placed in the centre of the cylindrical surface with a -10-dB aperture edge illumination. Simulated realized gain versus frequency is plotted in Fig. 3-12 with a realized gain of 21.1 dBi at 25 GHz. Compared to the previous 0.508-mm-thick TA, the aperture efficiency increases to 43.9% considering the gain calculated by the aperture cross-sectional size, and the 3-dB gain bandwidth increases to 17%.

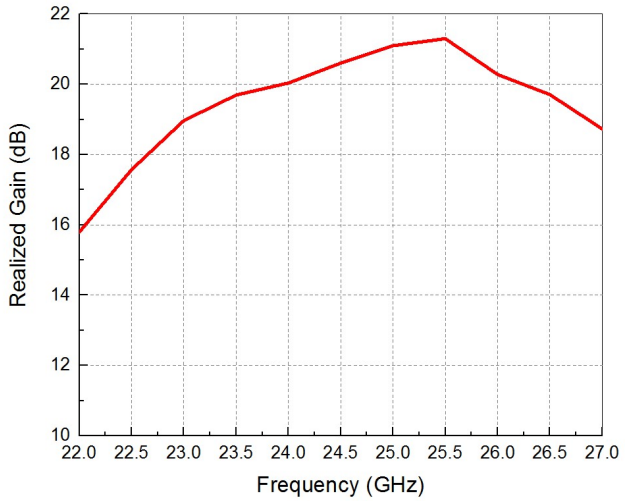


Fig. 3-12 Simulated realized gain of the conformal TA with 2.5-mm-thick elements.

It should be noted that the 0.508-mm-thick element selected in the final fabricated prototype is for the ease of bending of the conformal TA to verify the design concept. In principle, a conformal TA using 2.5-mm-thick elements could be fabricated using direct

ink printing technology, but this would be far beyond our budget and our access to the technology.

## 3.2 Mechanically Reconfigurable Conformal TA

For the conformal TA discussed in section 3.1, it can only radiate a beam towards a fixed direction. Electronic beam scanning can be achieved by employing active components, such as PIN diodes or varactor diodes, to change transmission phases of the array elements according to the beam direction required [34]-[37]. Usually, electronically reconfigurable TAs will involve a large number of active elements as the phase of each element needs to be changed independently. This may lead to extra loss, cost and complicated control networks. Furthermore, for conformal TA designs, if the curvature is very large, it might be difficult to integrate active elements on a curved surface.

This section demonstrates a method to achieve a mechanical beam scanning of the conformal TA reported in section 3.1. The method employed is to rotate the feed source only rather than simply rotating the entire transmitting surface and the feed source together. Actually, for many conformal applications, the transmitting surface, which could be the skin of communication platforms, cannot be easily moved.

### *3.2.1 Scanning Mechanism*

For a non-reconfigurable fixed-beam TA, each array element on the transmitting surface is designed to radiate the beam towards a specific angle, e.g. 0°. In order to achieve the beam scanning by rotating the feed source, the transmitting surface reported in section 3.1 is divided into two parts with respect to the centre line, as shown in Fig. 3-13 (a). If one part of the transmitting surface is designed to direct the beam to $\varphi 1$, and the other part is for $\varphi 2$, the combined beam is directed to $(\varphi 1 + \varphi 2)/2$. It should be pointed out that in order to avoid a split beam, these two beams cannot be separated far away from each other

with narrow beamwidths. It can be seen from Fig. 3-14 that the beam is split into dual beams when the angular step is 40° (means φ1= -20° and φ2=20°)). In this work, it is found that a step of 10° serves as an optimum value based on simulation results.

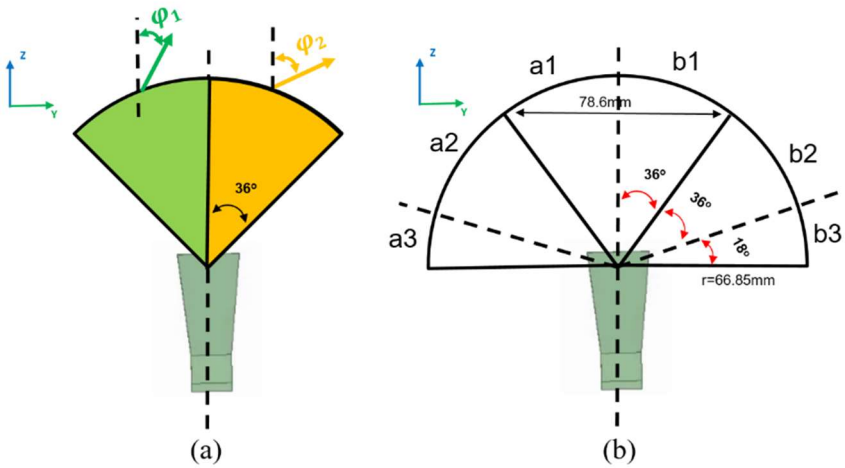


Fig. 3-13 (a) Fixed-beam conformal TA in section 3.1. (b) Beam-scanning conformal TA configuration.

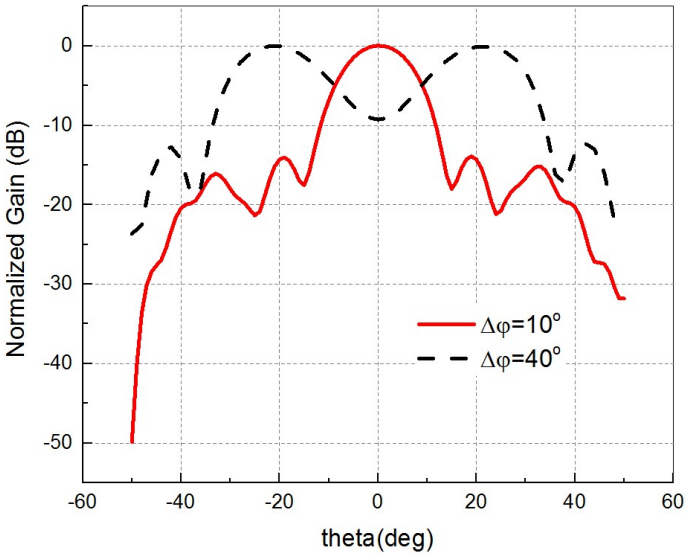


Fig. 3-14 Normalized patterns of the conformal TA with different angular steps for two beams.

The transmitting surface proposed in this work is shown in Fig. 3-13 (b), consisting of six parts marked as *a1*, *a2*, *a3*, *b1*, *b2*, *b3*. They are designed to radiate to different beam directions with respect to *z* axis, as shown in Fig. 3-15.

The subtended angles of the parts *a1*, *a2*, *b1*, *b2* are 36° and they are 18° for *a3* and *b3*. Therefore, the total subtended angle of the whole transmitting surface is 180°, making the surface as a half circle. A feed gain horn LB-28-15-C-KF from A-INFO is placed in the centre with a 12.2-dBi gain at 25 GHz. For each operating state of the TA, a transmitting surface with a 72° subtended angle is illuminated by the standard gain horn, resulting in a -10-dB edge illumination. In this case, the adjacent TA surface parts will have minimum effects on the active surface. The TA element size is the same as that reported in section 3.1. Each 72° transmitting surface consists of 15×13 elements. The cross-sectional size is 78.6 mm × 72.8 mm.

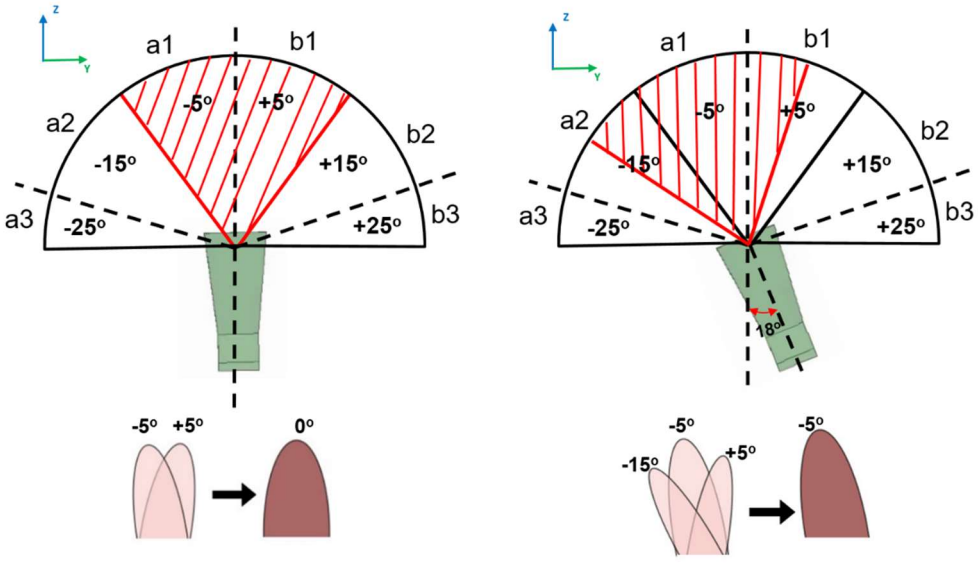


(a) (b)

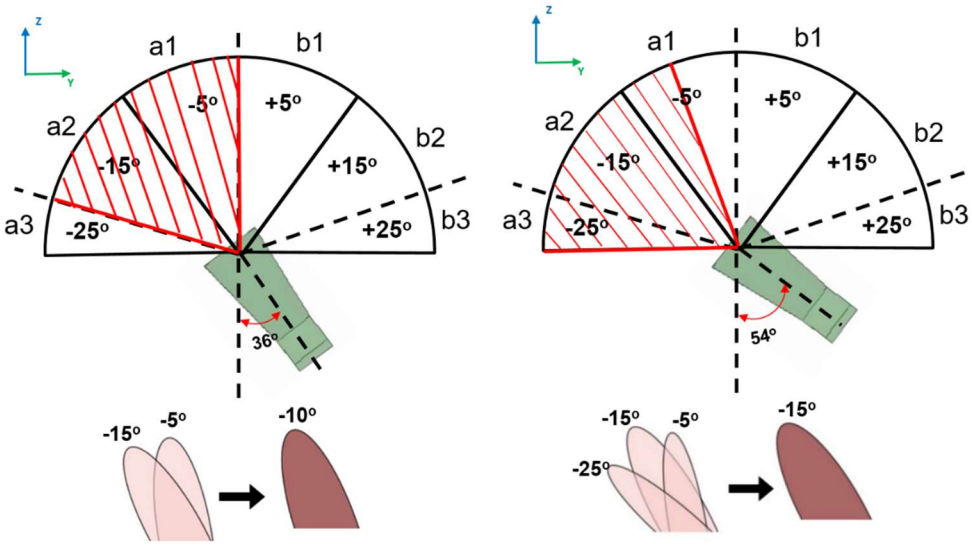


(c) (d)

Fig. 3-15 Different operating states of the beam-scanning conformal TA corresponding to different beam directions. (a) 0°. (b) -5°. (c) -10°. (d) -15°.

When the feed horn is pointed to the centre, the central two parts of the surface are illuminated as indicated with red stripe lines shown in Fig. 3-15 (a). As the two parts direct the beams to -5° and 5°, respectively, the combined beam is towards 0°. If the horn is rotated anti-clock-wisely by 18°, the active surface would change as shown in Fig. 3-15 (b). In this case, three parts are illuminated, namely, a1, half of a2, and half of b1. Then the combined beam will be directed to $(\varphi_{a1} + \varphi_{a2}/2 + \varphi_{b1}/2)/2 = (-5° + -15°/2 + 5°/2)/2 = -5°$.

Using the same principle, when the feed horn continues to be rotated by another 18°, as shown in Fig. 3-15 (c), the transmitting surface a1 and a2 will be active and the beam will be directed to -10°. The beam will be directed to -15° when the feed horn is rotated by a further 18° as shown in Fig. 3-15 (d). When the feed horn is rotated clock-wisely, main beam of the antenna can be directed to 5°, 10°, 15°, respectively, due to structural symmetries.

### *3.2.2 Experimental Results*

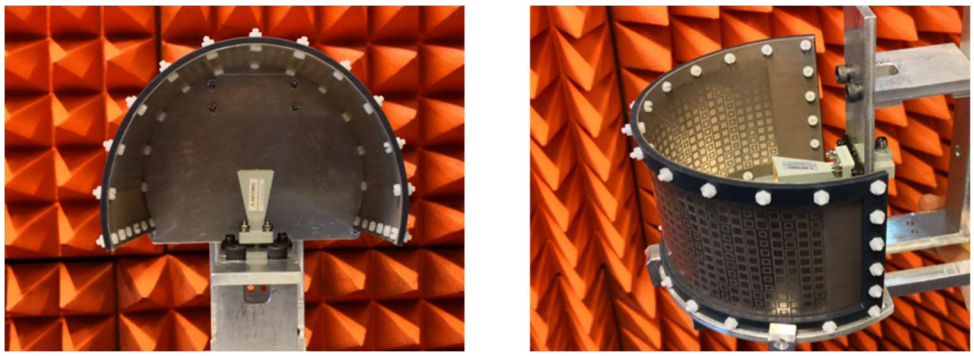

Fig. 3-16 Photograph of the reconfigurable TA prototype.

To verify the design concept discussed above, a reconfigurable conformal TA prototype working at 25 GHz is designed and fabricated. The array is fabricated on a Rogers DiClad 880 substrate (Dielectric Constant 2.2, tanδ=0.001) using the same method as the fixed-beam conformal TA in section 3.1. The two-layer surface is mounted on a platform with a rotatable gain horn. An angle square is printed at the back of the platform so that the gain horn can be rotated to any required angle. Photograph of the prototype is shown in Fig. 3-16.

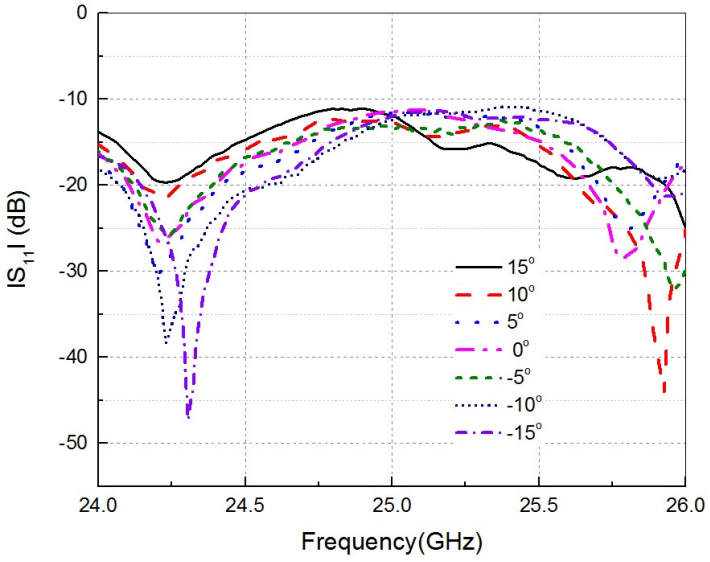


Fig. 3-17 Measured input reflection coefficients of the reconfigurable conformal TA.

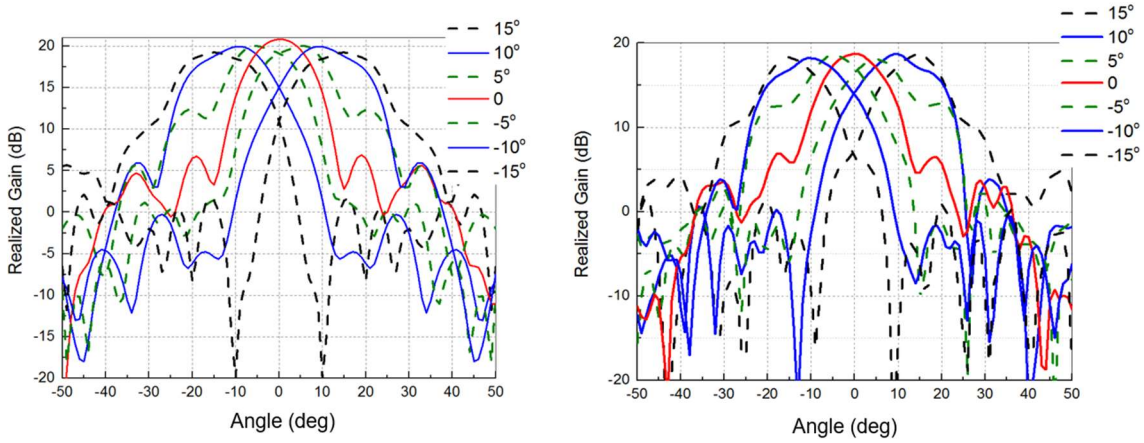


(a) (b)

Fig. 3-18 H-plane radition patterns at 25 GHz for different states of TA. (a) Simulated results. (b) Measured resutls.

Input refelction coefficients and radiation patterns were measured for seven different positions of the gain horn. It is seen from Fig. 3-17 that the measured input refelction coefficients are below -10 dB for all seven states from 24 GHz to 26 GHz. Measured and simulated patterns in H-plane are compared at 25 GHz in Fig. 3-18. The simulated gain at boresight is 20.3 dBi and around 19.5 dBi for other scanning angles. While for measured results, a stable gain value of about 18.7 dBi is achieved at all angles. Therefore, the scanning loss of this mechnically reconfigurable conformal TA is very small. As the beam in E-plane is not changed, the patterns are ommited here. They are similar to that of the fixed-beam TA given in Fig. 3-10. The absolute values of cross-polarization levels at 25 GHz are given in Fig. 3-19. The maximum cross-polarization level is 5 dBi at 15° scanning angle, which makes the relative cross-polarization level lower than -14 dB. It can be observed that the patterns in Fig. 3-19 are asymmetric for positive and negative scanning angles. This is attributed to the asymmertic structure along the direction of cross polarization for different angles. The cross-polarization levels at other frequency points in the operating bandwidth are similar to Fig. 3-19. For each working state with a 72°

transmitting surface, the simulated aperture efficiency is 17.8%, while the measured one is 14.8%. The efficiency of the scanned TA is lower than that of the fixed one. This is mainly due to the beam combination used to generate the steered beams. As a result, the realized gain of the scanned array is lower than that of the fixed one.

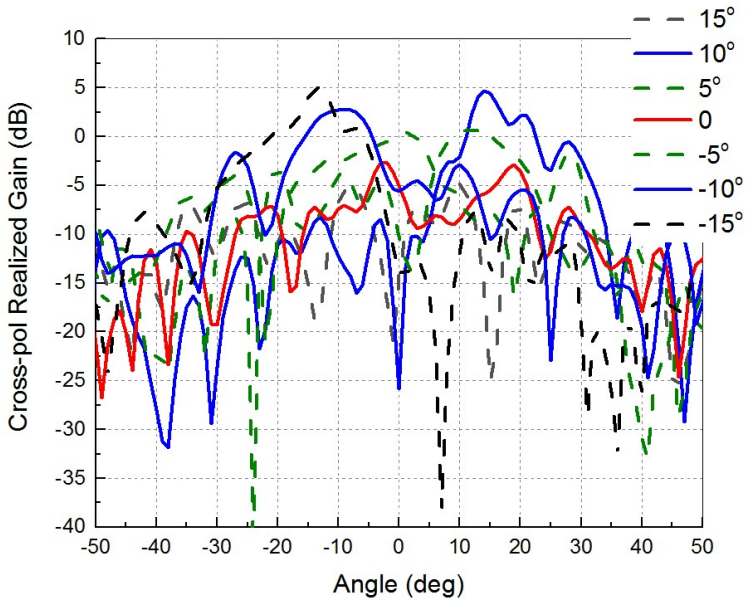


Fig. 3-19 Measured cross-polarization level in H-plane at 25 GHz for different states of conformal reconfigurable TA.

### 3.3 Discussion

This section discusses the beam scanning range of the proposed conformal TA. As described in the last section, each main beam of the array is a combination of the beams of two or three parts on the transmitting surface. Therefore, as illustrated in Fig. 3-20, the beam scanning range is related to the beam direction of each part $\theta_{rn}$ (with respect to $z$ axis), the subtended angle of each part $\theta_h$ and the number of the parts $2(n+1)$ (total $n+1$ parts for each half of the transmitting surface). For the *n-th* part of the transmitting surface $b_n$, the radiation direction $\theta_{rn}$ should satisfy (3-4).

$$\theta_{nS} < \theta_{rn} < \theta_{nL} \tag{3-4}$$

$$\theta_{nL} = 90^o + (n-1) * \theta_h \tag{3-5}$$

$$\theta_{nS} = n * \theta_h - 90^o \tag{3-6}$$

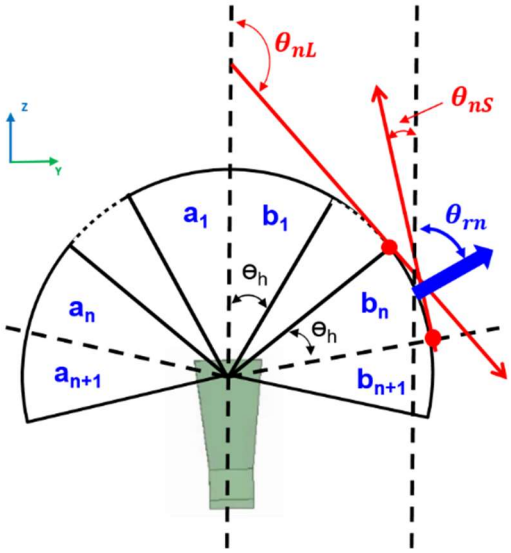


Fig. 3-20 Beam-scanning conformal TA configuration with 2(n+1) parts.

In the previous design, $\theta_h$ is chosen as 36° to satisfy a -10-dB edge illumination. The beam directions for the parts *a1* and *b1* are chosen to be -5° and 5°, respectively, resulting in a 10° step. If this step is increased, the combined beam will tend to be split and the gain will drop. If the step is decreased, the total scanning range will be reduced. Therefore, the 10° step serves as an optimum trade-off value based on a few simulated results. Following this angular step, we have the parts *a2* and *a3* radiating to -15° and -25°, respectively. Note that -25° ($\theta_{r\_a3}$) is with respect to the *z* axis. If considering the centre axis of the part *a3* (which is -*y* axis), it is 65° as shown in Fig. 3-21. As known, the directivity will drop significantly when the beam is scanning away too much from the direction perpendicular to the transmitting surface. For this reason, the beam combined from *a2* and *a3*, which should point to -20°, has a reduced gain and is not used in this array. As a result, only half of *a3* is used in the array for a -15° beam direction (as seen from Fig. 3-15 (d)). Therefore, the subtended angles of *a3* and *b3* are half of the other parts. Also,

there is no need to include more parts for larger beam angles as the gain will be reduced further. One possible method to increase the beam scanning range is to reduce the subtended angle of each transmitting surface part so that more surface parts can be included, and (3-4) can be referred for angle limits estimation.

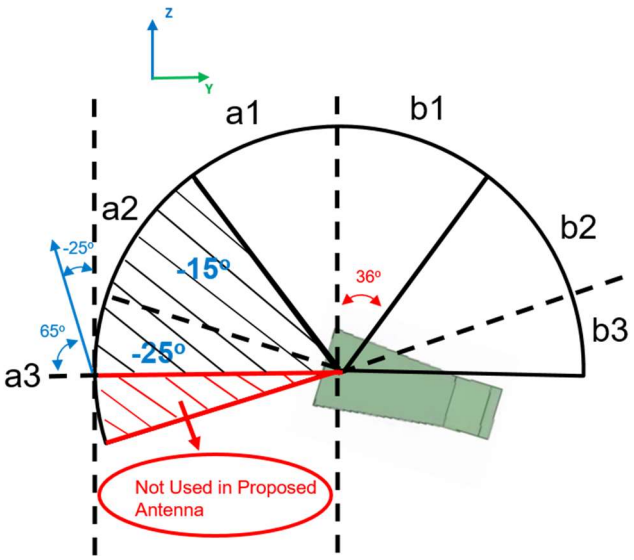


Fig. 3-21 Beam steering range limit of the proposed conformal tranmsitarray antenna.

Comparing to a fixed-beam conformal TA consisting of two parts, for example, *a1* and *b1*, the total size of the reconfigurable one is only about 2.5 times larger; but seven beam directions have been achieved. For some communication platforms where the size of the surface is not a primary constraint, the reported beam scanning method can be applied.

It should be noted that a straightforward way to achieve beam scanning is to employ several identcial transmitting surfaces and rotate the feed horn to the centre of each surface, as shown in Fig. 3-22. But the number of the beam direction is dependent on the number of the TA antenna used and the angular step is usually large and inflexible. For example, if three identical transmitting surfaces consisting of *a1* and *b1* are used as shown in Fig. 3-22, three beams pointing to -72°, 0°, and 72° are achieved when the feed horn is switched to the centre of each surface.

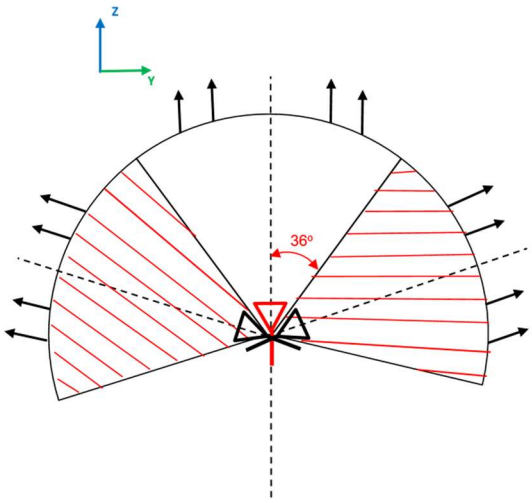


Fig. 3-22 Three TAs combined for three beam directions, -72°, 0°, and 72°.

## 3.4 Conclusion

A conformal TA and its beam steering are presented in this chapter. First, a thin array element is developed, consisting of three layers of identical square-ring slots. The total thickness of the element is 0.508 mm which is $0.04\lambda_0$ at 25 GHz. A transmission phase range of 330° is realized with a maximum 3.6 dB loss. Second, a curved TA that is conformal to a cylindrical structure is designed using the proposed elements. A peak measured gain of 19.6 dBi at 25.5 GHz is obtained. Third, by combing transmitting surfaces with different beam directions and rotating the feed horn, beam steering of a conformal TA is realized. The size of the reconfigurable TA is approximately 2.5 times of that of the array with a fixed beam, while it can switch the beam to ±15°, ±10°, ±5° and 0° with a stable realized gain of 18.7 dBi. Measured results agree well with simulated ones. The developed TA and its beam steering may find wide applications in communication systems where conformal structures are demanded.

# Chapter 4: A High-Efficiency Conformal Transmitarray Antenna Employing Dual-Layer Ultra-Thin Huygens Element

Although the thickness of some reported planar TA elements has been considerably reduced, most of them are three-metal-layer structures. Precise alignment and attachment of multilayers would be very challenging and costly, especially at high frequencies. This is one of the main reasons that many dual-layer RAs, i.e. one metal layer printed on a grounded substrate, are developed [76]-[78]. However, only several reports on dual-layer TA elements have been published [32], [79]. They either contain vias in the element model or provide a low aperture efficiency. The element thickness of these models is around $0.1\lambda_0$, making them only suitable for conformal TAs operating at above 30 GHz ($\lambda_0$ =10 mm) for the ease of bending. Also, elements with vias are not preferable for conformal designs. However, TAs working below 30 GHz are highly desired by many applications, e.g., 5G systems and satellite systems. Therefore, an ultra-thin element without any vias which can be employed for conformal TAs operating below 30 GHz is desperately needed. It should be noted that although using high dielectric substrate may be able to reduce the thickness of the array element, the antenna efficiency will be significantly affected due to the loss and the total cost of the array will be increased. Another straightforward method is to compress the total thickness of the multi-layer

element. However, as demonstrated in Chapter 3, this will reduce the antenna efficiency significantly as the element loss is increased. Therefore, a key challenge for conformal TAs is to develop ultra-thin array elements with a high aperture efficiency.

In this chapter, Huygens metasurface theory is employed to develop an ultra-thin dual-layer element for high-efficiency conformal TAs. Huygens elements [80] can be used for TAs as they are capable of realizing non-reflection and total transmission with sub-wavelength thickness, making it be a good candidate to provide high efficiencies with low profiles in TAs. However, most of the currently reported Huygens elements have multi-layer structures. In [81], the element consists of three metal layers using two vias to connect the first and the third layer to create a current loop for a magnetic response. The second layer is for an electric response. The total thickness is 3 mm at 10 GHz ($0.1\lambda_0$ at 10 GHz). The elements in [82] consist of three-layer patterned metallic surfaces to mimic one electric dipole and one magnetic dipole printed on two bonded substrates. The thickness of the element is 0.4 mm ($0.1\lambda_0$ at 77 GHz). In addition, there are some two-layer Huygens elements [83]-[84] that can introduce electric and magnetic currents on two metal layers separately. However, the main limitation is that discrete printed circuit board tiles have to be made for each array element and the boards are stacked into an array. Compared with fully planar structures [81]-[82], this makes it more difficult to assemble a large surface.

From the above discussions, one can conclude that innovation is needed to develop dual-layer ultra-thin Huygens elements for high-efficiency TAs, especially the conformal ones. In this chapter, we developed a two-layer Huygens element without any metallic vias first. The element's thickness $h$ is 0.5 mm ($\lambda_0/60$ at 10 GHz). It consists of a pair of symmetrical 'I' shape patches on top and bottom layers and double 'T' shape strips

located on the margins of two layers to mimic a magnetic dipole and an electric dipole, respectively. Second, for TA applications, we design eight elements with different dimensions to cover a quantized 360$^{o}$ phase range, and the highest element loss is 1.67 dB. Third, a cylindrically conformal TA is developed employing the proposed Huygens elements. The measured aperture efficiency is found to be 47%, which is much higher than the conformal TA previously developed in Chapter 3 and other reported planar TAs with similar thickness. To the authors' best knowledge, the developed conformal TA is the first one with a high aperture efficiency and the thinnest profile.

The rest of this chapter is organized as follows. In section 4.1, a detailed element design procedure is developed based on Huygens surface theory. A cylindrically conformal TA based on the proposed element is simulated and analysed in section 4.2. As a verification, a prototype is fabricated and measured in section 4.3. The chapter concludes in section 4.4.

## 4.1 Huygens Element Design

### *4.1.1 Huygens Surface Theory*

As shown in Fig. 4-1 (a), when an incidence wave impinges on a Huygens surface, both the surface electric current Js and the magnetic current Ms would be induced, resulting in reflection and transmission waves which depend on the electric and magnetic current densities. Once E-current and M-current are excited, each of them can be taken as a source to generate electromagnetic fields on both sides of the surface. The Huygens surface can be analysed from electric and magnetic sources separately, and the generated waves from two sources in $z<0$ and $z>0$ regions are shown in Fig. 4-1 (b).

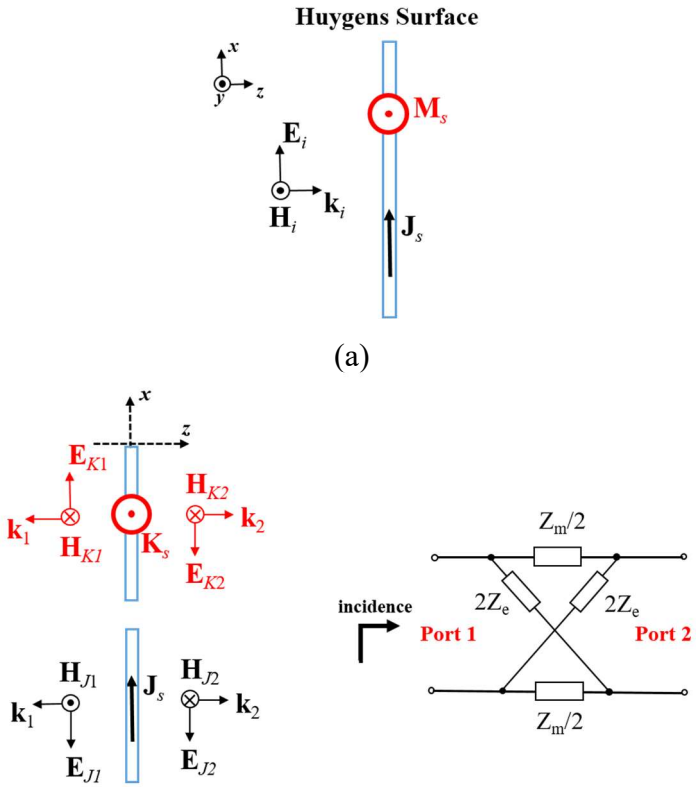


Fig. 4-1 Huygens surface. (a) Field sketch with macro-perspective. (b) Fields generated by E-current and M-current separately. (c) Equivalent circuit model.

For a single E-current surface, it would satisfy the boundary conditions:

$$\boldsymbol{z} \times [\boldsymbol{E}_e(z = 0_+) - \boldsymbol{E}_e(z = 0_-)] = 0 \tag{4-1}$$

$$\boldsymbol{z} \times [\boldsymbol{H}_e(z = 0_+) - \boldsymbol{H}_e(z = 0_-)] = \boldsymbol{J_s} = \frac{1}{Z_e} \cdot \boldsymbol{E}_{te}(z = 0) \tag{4-2}$$

where $\boldsymbol{E}_e$ and $\boldsymbol{H}_e$ denote the electric and magnetic field intensities generated from E-current, respectively. $\boldsymbol{E}_{te}$ is the tangential part of $\boldsymbol{E}_e$, and $Z_e$ represents surface electric impedance. By inserting the fields generated from $\boldsymbol{J_s}$, as denoted in Fig. 4-1 (b), into (4-1) and (4-2), we can get

$$\boldsymbol{E}_{J1} = \boldsymbol{E}_{J2} \tag{4-3}$$

$$\boldsymbol{z} \times (\boldsymbol{H}_{J2} - \boldsymbol{H}_{J1}) = \boldsymbol{J_s} = \frac{\boldsymbol{E_{te}}(z=0)}{Z_e} \tag{4-4}$$

The tangential electric field on the surface is:

$$\boldsymbol{E}_{te}(z=0) = \boldsymbol{E}_{J1} + \boldsymbol{E}_i \,, or \;\; \boldsymbol{E}_{J2} + \boldsymbol{E}_i \tag{4-5}$$

where $\boldsymbol{E}_{J1}$and $\boldsymbol{H}_{J1}$are the fields generated by $\boldsymbol{J_s}$ in z<0 region, while $\boldsymbol{E}_{J2}$ and $\boldsymbol{H}_{J2}$ are the ones in z>0 region, and $\boldsymbol{E}_i$ refers to the incident field which exists in the whole area. Then, we can derive

$$\boldsymbol{E}_{J1} + \boldsymbol{E}_i = Z_e \cdot \boldsymbol{J_s} = Z_e \cdot \boldsymbol{z} \times (\boldsymbol{H}_{J2} - \boldsymbol{H}_{J1}) = \frac{-2Z_e}{\eta} \cdot \boldsymbol{E}_{J1} \tag{4-6}$$

$$\boldsymbol{E_{J1}} = \frac{-\eta}{2Z_e + \eta} \boldsymbol{E_i} \tag{4-7}$$

where $\eta$ denotes the wave impedance in free space. For a single M-current surface, it would satisfy the following boundary conditions:

$$-\boldsymbol{z} \times [\boldsymbol{E}_m(z=0_+) - \boldsymbol{E}_m(z=0_-)] = \boldsymbol{M_s} = Z_m \cdot \boldsymbol{H}_{tm}(z=0) \tag{4-8}$$

$$\boldsymbol{z} \times [\boldsymbol{H}_m(z=0_+) - \boldsymbol{H}_m(z=0_-)] = 0 \tag{4-9}$$

where $\boldsymbol{E}_m$ and $\boldsymbol{H}_m$ denote the electric and magnetic field intensities generated from M-current, respectively. $\boldsymbol{H}_{tm}$ is the tangential part of $\boldsymbol{H}_m$, and $Z_m$ represents surface magnetic impedance. With the similar derivation process to the E-current surface, we can obtain

$$\boldsymbol{E}_{M1} = \frac{Z_m}{Z_m + 2\eta} \boldsymbol{E}_i \tag{4-10}$$

Finally, for a complete Huygens surface with both E-current and M-current, as shown in Fig. 4-1 (a), we denote reflection and transmission coefficients as *R* and *T*, respectively, as given in [83], [85]. Then one obtains

$$R = \frac{(\boldsymbol{E}_{J1} + \boldsymbol{E}_{M1}) \cdot \hat{\boldsymbol{x}}}{\boldsymbol{E}_i \cdot \hat{\boldsymbol{x}}} = \frac{-\eta}{2Z_e + \eta} + \frac{Z_m}{Z_m + 2\eta} \tag{4-11}$$

$$T = \frac{(\boldsymbol{E}_{J2} + \boldsymbol{E}_{M2} + \boldsymbol{E}_i) \cdot \hat{\boldsymbol{x}}}{\boldsymbol{E}_i \cdot \hat{\boldsymbol{x}}} = \frac{2Z_e}{2Z_e + \eta} - \frac{Z_m}{Z_m + 2\eta} \tag{4-12}$$

After doing some transformations of equations (4-11)-(4-12), we get

$$Z_e = \frac{\eta}{2} * \frac{1 + R + T}{1 - R - T} \tag{4-13}$$

$$Z_m = 2\eta * \frac{1 + R - T}{1 - R + T} \tag{4-14}$$

Therefore, Huygens surface is capable to realize non-reflection and full-transmission with variable transmission phases $\varphi_t$, referred as $R = 0, T = e^{j\varphi_t}$, as long as it satisfies

$$Z_e = \frac{j\eta}{2tan(\varphi_t/2)} \tag{4-15}$$

$$Z_m = -j2\eta \tan\left(\frac{\varphi_t}{2}\right) \tag{4-16}$$

It can be seen from (4-15) and (4-16) that the electric and magnetic surface impedances are related to the transmitting phase. In another words, for each specific transmitting phase, there are corresponding surface impedances. In the next sub-section, we will develop Huygens elements for the specified transmitting phases. As indicated in [86]-[87], the whole Huygens surface can be equivalent to a circuit model as shown in Fig. 4-1 (c), and $Z_e$ and $Z_m$ can be defined by Z matrix from microwave network theory:

$$Z_e = 1/2 * (Z_{11} + Z_{21}) \tag{4-17}$$

$$Z_m = 2 * (Z_{11} - Z_{21}) \tag{4-18}$$

### *4.1.2 Element Synthesis*

The schematics of the developed Huygens element are given in Fig. 4-2. It consists of two metallized layers printed on two sides of a 0.5 mm-thick substrate (Dielectric

Constant 3.55, tanδ = 0.0027). The substrate thickness is selected as 0.5 mm in this work in order to make it bendable. The 'I' shape patches on the centre of top and bottom layers have exactly the same dimensions. Besides, one pair of head-to-head 'T' shape stubs are printed on each side of the substrate but at different positions. The distance between 'T' stubs and the boundary of the element is 0.8 mm. The periodicity of the element *P* is 8.5 mm.

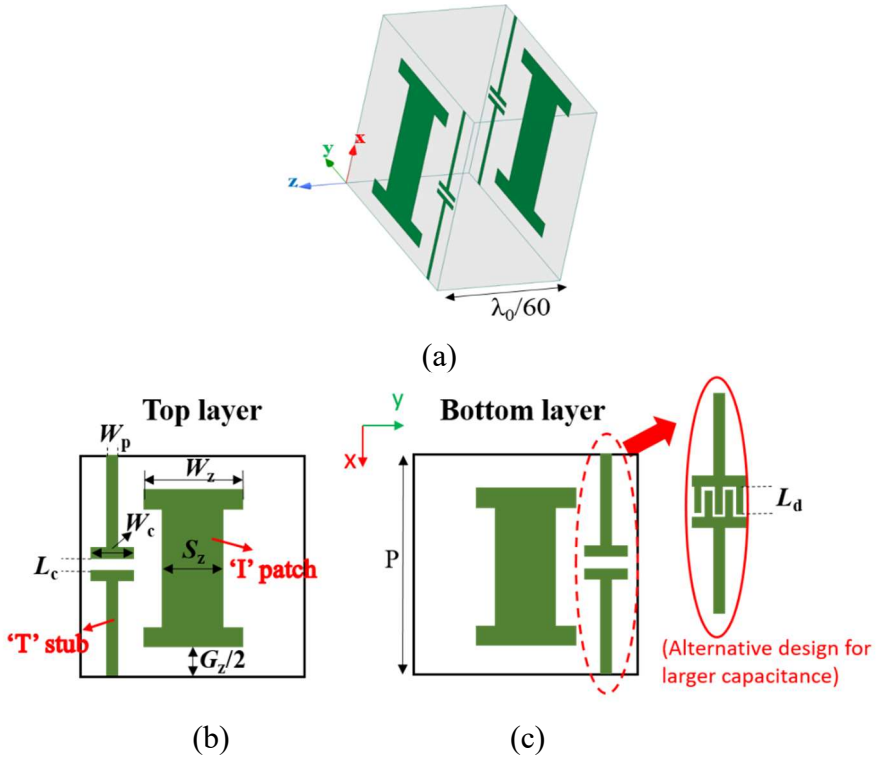


Fig. 4-2 Developed two-layer Huygens element model. (a) 3-D structure. (b) Top and bottom layers.

For many three-layer Huygens elements, the metal traces on the first and third layers are used to generate a current loop to be equivalent to a magnetic dipole, while the trace in the middle layer is for introducing an electric dipole. In our developed element, only two metal layers are used and the substrate is significantly thinner. When an *x*-polarized wave impinges on the element, the 'I' shape patches on the top and bottom layers produce

currents with opposite directions, thereby generating a current loop, which can be equivalent to a magnetic dipole. This will be verified in the current distributions shown in the following part. One pair of head-to-head 'T' shape stubs will produce currents along *x*-axis with the same direction, thereby introducing an electric dipole. These 'T' shape stubs will not affect the magnetic response, while the 'I' shape patches have some influence on the electric response. Therefore, the 'I' shape patches will be designed first for desired magnetic responses. Then, the 'T' shape stubs will be designed to control the electric response.

The magnetic response related to the magnetic surface impedance $Z_m$ can be adjusted by changing the capacitive or inductive properties of the 'I' shape patches, which are related to the patch dimensions $W_z$, $G_z$ and $S_z$. The electric response related to the electric surface impedance $Z_e$ can be manipulated by varying the values of $L_c$, $W_c$ and $W_p$. In some cases where large capacitance between the two 'T' shape stubs is needed, e.g., the element is illuminated under large oblique incidence angles which would be discussed in section 4.2, the interdigital parasitic strips with length $L_d$ will be adopted for each pair, as shown in the inset of Fig. 4-2 (b). For an *x*-polarized incident wave, the transmitting phase of the Huygens element can be varied by changing the element's dimensions. However, it cannot be continuously changed if varying only one or two dimensions of the element. An optimization on the element's entire dimensions would be required to achieve a continuous phase change, which may make the design of TAs very complicated and time-consuming. Instead, a quantized phase distribution is employed. In this work, eight elements are designed to achieve a 3-bit quantized phase distribution. The detailed phase points and corresponding $Z_m$ and $Z_e$ values calculated from (4-15) and (4-16) are listed in Table 4-1.

Table 4-1 Huygens properties from theoretical calculation with quantized 360° phase cover

| Element No. | Phase | Im($Z_e$)/kΩ | Im($Z_m$)/kΩ |
|---|---|---|---|
| 1 | -15° | -1.43 | 0.1 |
| 2 | -60° | -0.33 | 0.44 |
| 3 | -105° | -0.14 | 0.98 |
| 4 | -150° | -0.05 | 2.81 |
| 5 | -195° | 0.02 | -5.72 |
| 6 | -240° | 0.11 | -1.31 |
| 7 | -285° | 0.25 | -0.58 |
| 8 | -330° | 0.7 | -0.2 |

As discussed in the last paragraph, the dimensions of the 'I' shape patches of the element will be determined first for the magnetic response. At this step, only the 'I' shape patches are modelled on the element and simulated without the two 'T' shape stubs. Then the two 'T' shape stubs are added to the element and the model is simulated for the electric response.

Floquet ports with master-slave boundaries of 3-D electromagnetic (EM) simulation software HFSS is used for the simulation. In this work, $W_z$ value would be tuned for the magnetic response, while $S_z$ and $G_z$ are set as 2.3 mm and 1.7 mm, respectively, for simulation simplicity. Moreover, $L_c$ and $W_c$ are varied for tuning the electric response with $W_p$=0.2 mm. The dimensions, transmitting phases and amplitudes for the eight elements are given in Table 4-2.

Table 4-2 Properties of Huygens elements

| Element No. | Im($Z_e$) /kΩ | Im($Z_m$) /kΩ | $\lvert S_{21}\rvert$ /dB | $\angle S_{21}$ | Wz /mm | Wc /mm | Lc /mm |
|---|---|---|---|---|---|---|---|
| 1 | -2.3 | 0.13 | -0.16 | -14° | 3.6 | 1.3 | 0.1 |
| 2 | -0.35 | 0.17 | -0.42 | -41° | 3.8 | 1.6 | 0.1 |
| 3 | -0.12 | 0.64 | -1 | -100° | 4.1 | / | / |
| 4 | -0.04 | 1.6 | -1.67 | -153° | 4.19 | 1.2 | 0.6 |
| 5 | -0.02 | -0.44 | -1.66 | -187° | 4.2 | 1.2 | 0.37 |
| 6 | 0.1 | -1.1 | -1.36 | -241° | 4.25 | 1.5 | 0.4 |
| 7 | 0.22 | -0.52 | -0.86 | -284° | 4.3 | 1.62 | 0.4 |
| 8 | 0.94 | -0.25 | -0.5 | -330° | 4.4 | 1.62 | 0.35 |

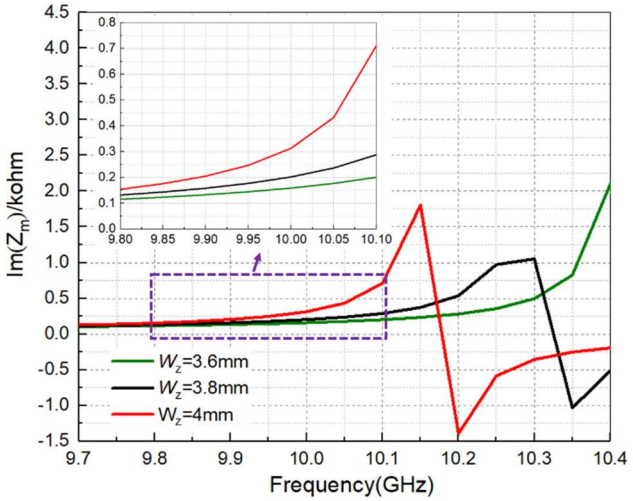


(a)

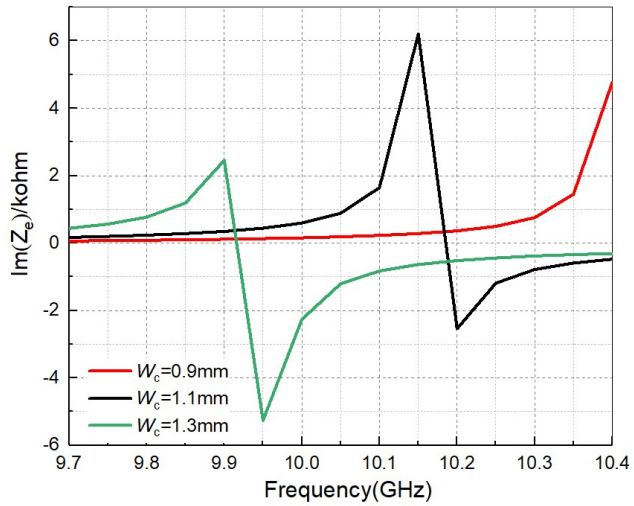


(b)

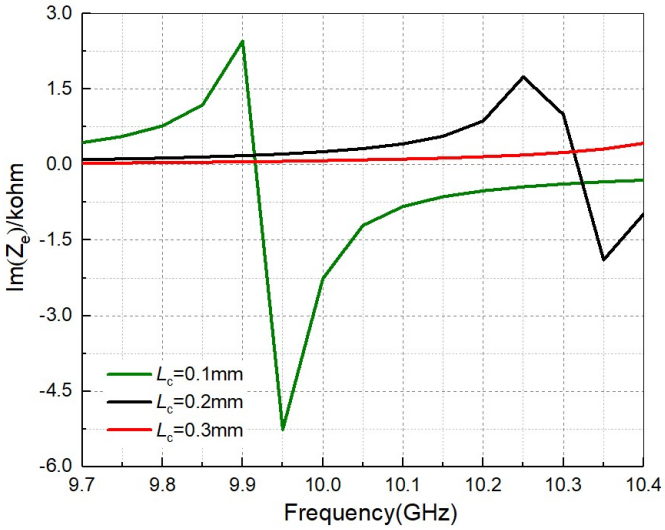


(c)

Fig. 4-3 Parametric studies for element 1. (a) Simulated $Z_m$ with different $W_z$. (b) Simulated $Z_e$ with different $W_c$. (c) Simulated $Z_e$ with different $L_c$.

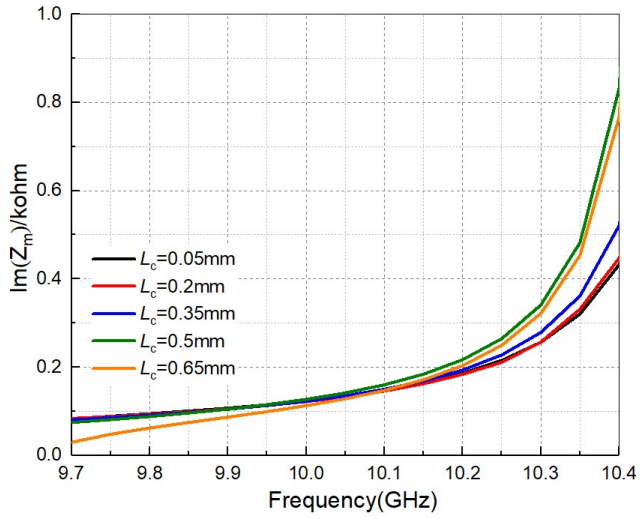


(a)

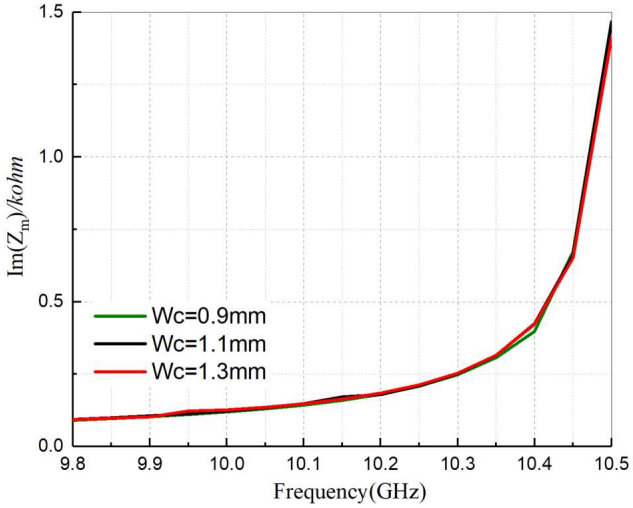


(b)

Fig. 4-4 (a) Simulated $Z_m$ with different $Lc$. (b) Simulated $Z_m$ with different $Wc$.

Fig. 4-3 shows the parametric studies on $W_z$, $L_c$ and $W_c$ based on element 1. When one parameter is studied, the other two are kept unchanged as provided in Table 4-2. As shown in Fig. 4-3 (a), $Z_m$ curve moves to lower band as $W_z$ increases, which provides a higher capacitance between 'I' shape patches of two adjacent elements. Besides, as seen in Fig. 4-3 (b) and (c), the $Z_e$ curve shifts left as $W_c$ increases, and it has the same changing trend when $L_c$ is decreased. This means $Z_e$ would move to lower band when the capacitance between two 'T' shape stubs of each element increases. Furthermore, as seen in Fig. 4-4, $L_c$ has almost no effect on the magnetic response at the desired frequency 10 GHz for a

changing range between 0.05 mm and 0.65 mm. $W_c$ is found to have little influence on the magnetic response either. This is the reason why magnetic and electric responses can be designed independently.

By using the above parametric studies, an iterative method is employed to obtain other elements' dimensions at 10 GHz. First, the Z matrix of an initial element model is simulated under periodic boundary conditions, and the values of $Z_{\mathrm{m}}$ and $Z_{\mathrm{e}}$ can be obtained based on (4-17) and (4-18). Then, the dimensions are further adjusted to make $Z_{\mathrm{m}}$ and $Z_{\mathrm{e}}$ close to the required values listed in Table 4-1 to achieve the desired transmitting phase. For Element 3, the two head-to-head 'T' shape stubs are not needed as the "I" shape patch can provide sufficient electric response. It should be noted that the ideal Huygens elements should realize a full transmission without any losses. However, as the developed elements use two metal layers to mimic a Huygens element and the substrate is lossy, small transmission loss is expected. The losses are found to be comparable to those three-layer Huygens elements [82]. Moreover, for some specific phase values, the transmission loss of the element is larger than 2 dB. In this case, small variations on the phase values are made to lower the loss. For example, for Element 5, the required phase is -195°, while the synthesised phase is -187°. Here, a compromise between phase error loss and amplitude loss should be made. After finding the elements' dimensions for each phase value, the transmission coefficients for each element can be obtained. The $S_{21}$ result for element 1 is given in Fig. 4-5 as an example. It can be seen that the element transmission loss is only 0.16 dB at 10 GHz and its phase value is -14$^{\mathrm{o}}$ which is close to the desired value -15$^{\mathrm{o}}$ listed in Table 4-1.

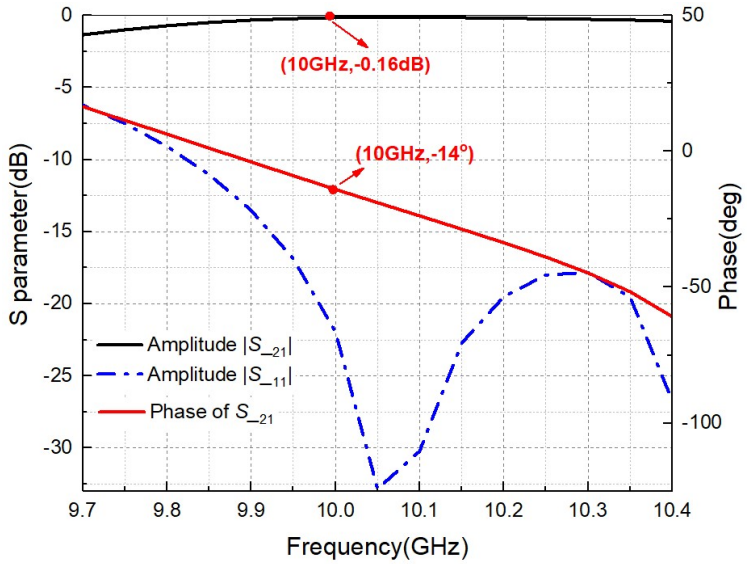


Fig. 4-5 Simulated S-parameter for element 1.

Table 4-3 Dimensions of Element 4 with different substrate thickness

| Thickness *h*/mm | Wp /mm | Wz /mm | Wc /mm | Lc /mm | \|S21\| /dB | $\angle S_{21}$ |
|---|---|---|---|---|---|---|
| 0.254 | 0.2 | 4.19 | 1.2 | 0.35 | -3.2 | -149° |
| 0.5 | 0.2 | 4.19 | 1.2 | 0.6 | -1.67 | -153° |
| 0.8 | 0.5 | 3.97 | 1.2 | 0.6 | -0.6 | -153° |

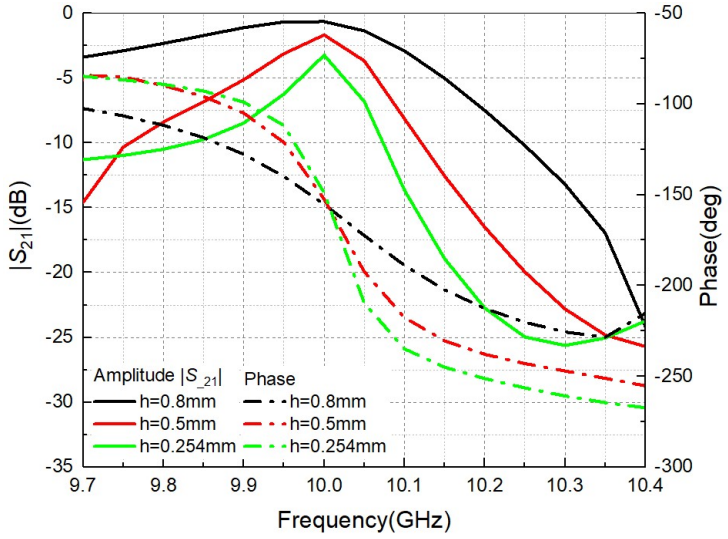


Fig. 4-6 Simulated S parameter of Element 4 with different substrate thickness values.

We examine the effects of the substrate thickness on the transmission loss of the elements. We take Element 4 (with a transmitting phase of -153° from Table 4-2) as an example.

Under three different substrate thickness values, three different models of Element 4 are designed. Their dimensions are given in Table 4-3, and the phase and magnitude of transmission coefficients are compared in Fig. 4-6. It can be seen that as the thickness reduces from 0.8 mm to 0.254 mm, the transmission loss increases from 0.6 dB to 3.2 dB. This is due to the fact that the balanced condition between electric and magnetic responses is broken when the thickness of the substrate is reduced too much. It is known that the magnetic current depends on the area of the current loop [88]. As demonstrated in Fig. 4-7 (b) and (d), the area of current loop is proportional to the thickness of substrate. If the thickness is too small, the magnetic current will become too weak, thereby being unable to balance the electric current. Therefore, in order to make a good balance and minimize the element loss, a thicker substrate should be employed. However, for the ease of bending, 0.5 mm is chosen to balance the thickness and loss. Moreover, we check the current distributions for Element 1 at different times, as shown in Fig. 4-7. It can be seen that the currents on the two 'I' shape patches form loops as at t=T/4 and 3T/4 (T is one time period), which provide the equivalent magnetic response.

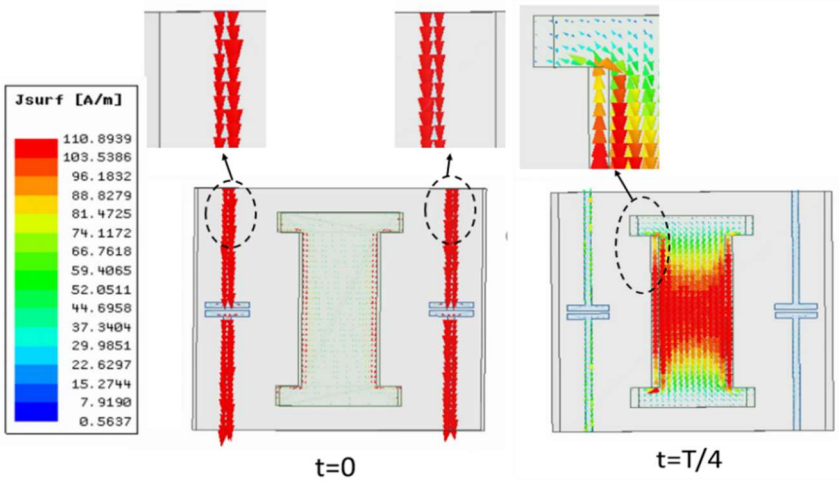


(a) (b)

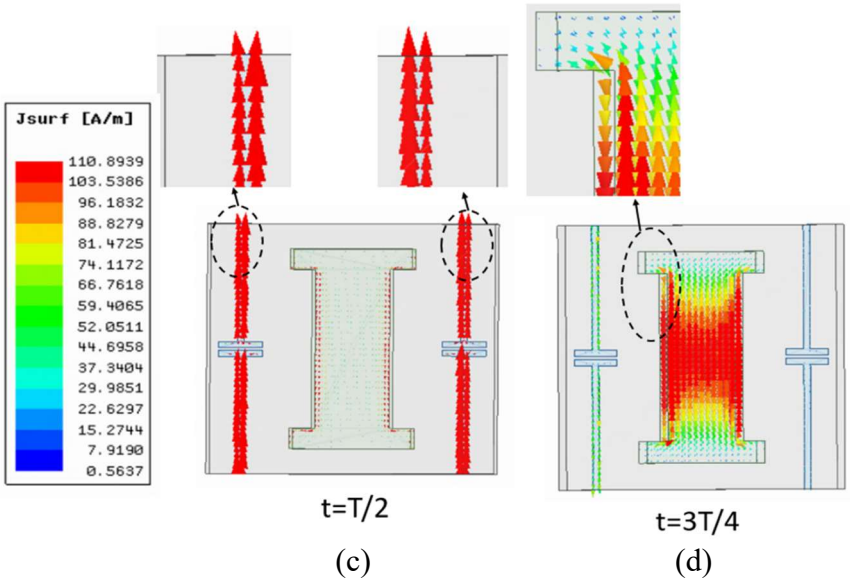


Fig. 4-7 Current distributions at specific times in one period T.

## 4.2 High-Efficiency Conformal TA Design

To verify the feasibility of the Huygens elements designed above, a small cylindrically conformal TA is constructed with 10×11=110 elements, and its contour is provided in Fig. 4-8. The TA aperture is bent along *y0z* plane (H-plane of the gain horn) to make the "I" and "T" shape patches aligned with the E-field of the feed horn, thereby maximizing the realized gain of the TA. A standard gain horn LB-75-10-C-SF from A-INFO is placed at the focal point with an edge illumination of -10 dB. The gain at 10 GHz of LB-75-10-C-SF from the data sheet is 10.15 dBi. The simulated input reflection coefficient of the antenna is below -10 dB from 9.6 GHz to 10.4 GHz, as given in Fig. 4-9 (a), and its realized-gain patterns at 10 GHz along E plane and H plane are plotted in Fig. 4-9 (b). The peak gain is 16.7 dBi, which corresponds to a 47.3% antenna efficiency considering the gain calculated by the aperture cross-sectional size (75.7 mm × 93.5 mm). The simulated cross-polarization levels are very small, lower than -40 dB. For the sake of clarity, they are not given in Fig. 4-9.

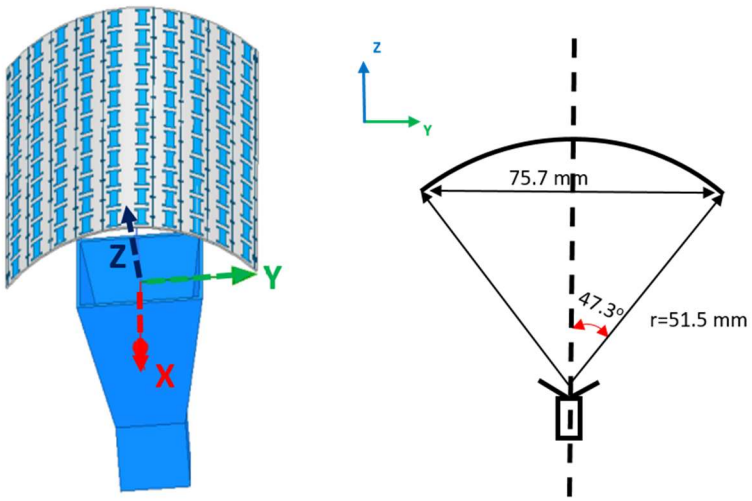


(a) (b)

Fig. 4-8 Conformal TA. (a) 3-D structure. (b) Sketch of front view.

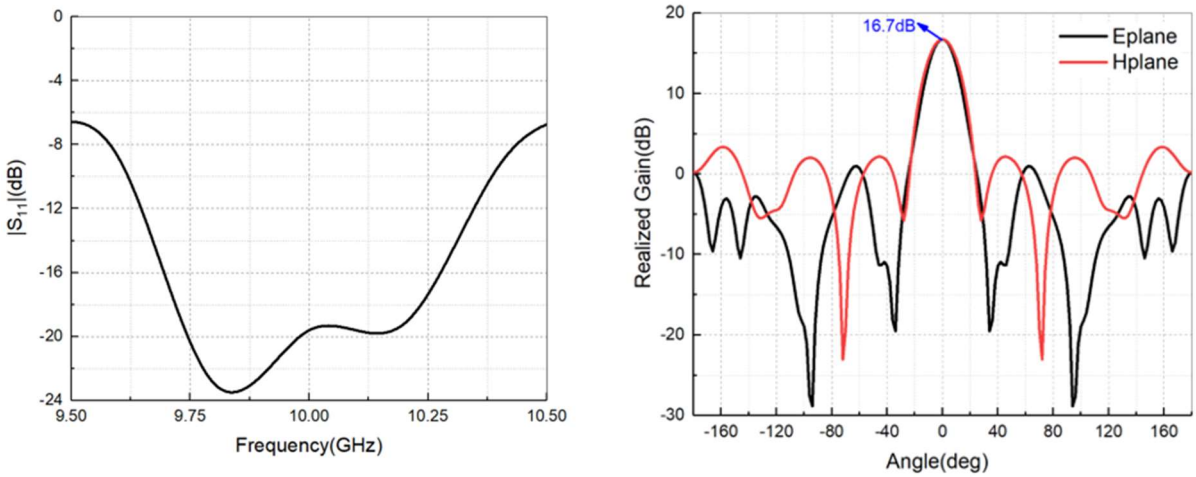


(a) (b)

Fig. 4-9 Simulated results of conformal TA. (a) $|S_{11}|$ versus frequency. (b) E plane and H plane patterns at 10 GHz.

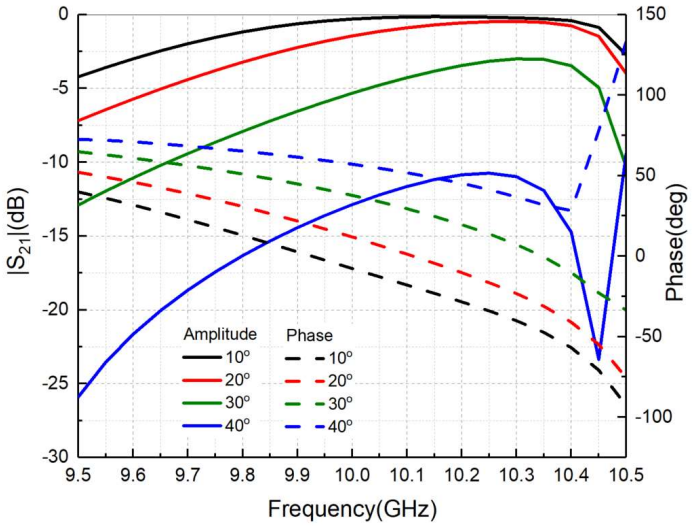


Fig. 4-10 Simulated $S_{21}$ amplitude and phase of element 1 under different oblique incidence angles.

It is known that the performance of Huygens surface is sensitive to the incident angle [86]. As indicated in Fig. 4-10, when Element 1 is simulated under different incidence angles, its amplitude and phase of $S_{21}$ change with the angle. In the previous Huygens element simulation, a normal incidence is adopted. For the conformal TA design, however, different incident angles should be considered for each element synthesis. As shown in Fig. 4-11 (a), along *x0z* plane, we can divide our model into 11 zones. Considering the structure symmetry, there are 6 zones illuminated with different angles $\theta_s$.

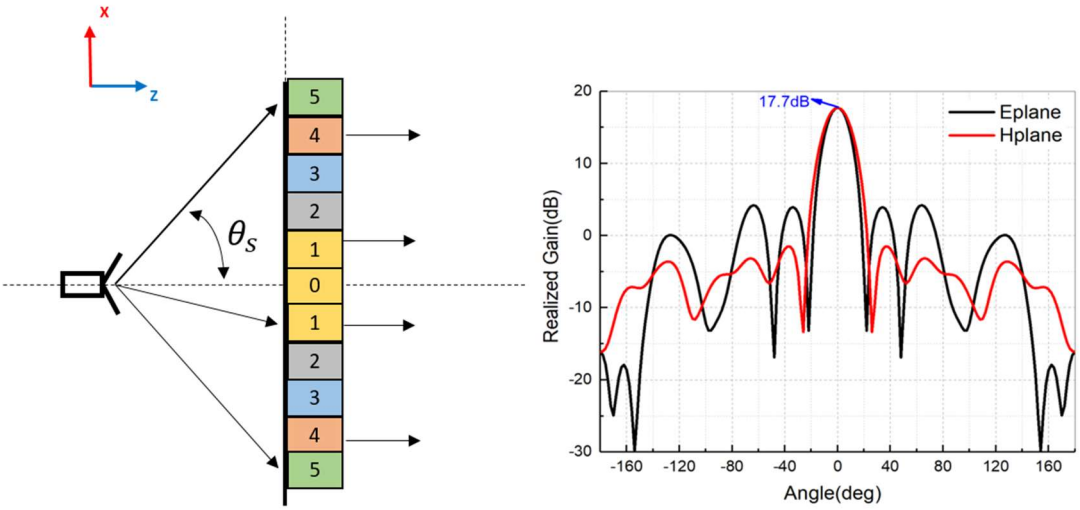


(a) (b)

Fig. 4-11 Conformal TA design with oblique incidence consideration. (a) Schematic with different zones along x0z section. (b) Simulated radiation patterns of E plane and H plane.

For a more accurate design, each Huygens element developed in the last section should be re-designed under specific oblique incidence angles. As the incident angle $\theta_s$ for Zone 1 is very small, it is integrated with Zone 0 and the elements are still simulated using normal incidence wave. For elements in Zones 2-5, their dimensions are re-designed for each corresponding angle. Taking Element 1 with $\angle S_{21}$=-14° as an example, the element model is re-simulated after changing the scan angle value in the master-slave boundary settings of HFSS, and the updated dimensions under each situation are listed in Table 4-4. Compared to the model under the normal incidence with dimensions listed in Table 4-2, $W_c$ and $L_c$ of the element are changed, while $W_z$ is unchanged. As observed in Table 4-4, the larger the incidence angle is, the higher the capacitance from head-to-head 'T stub' is required. In order to increase the capacitance, $L_c$ needs to be reduced and/or $W_c$ needs to be increased. In some cases, additional interdigital parasitic strips are needed to increase

the capacitance (shown as inset of Fig. 4-2). These design rules are also suitable for other seven elements. The dimensions for the other seven elements are given in the Appendix. Finally, along each zone we employ the elements developed at the corresponding incidence angle. The cylindrical TA with new elements is simulated, and the realized-gain patterns are shown in Fig. 4-11 (b). Compared with the results shown in Fig. 4-9, the peak gain at boresight is improved from 16.7 dBi to 17.7 dBi with a significantly reduced back lobe from 0 dBi to -17 dBi, and the aperture efficiency is improved to 58%.

Table 4-4 Properties of element 1 under different oblique incidence angles

| Zone No. | Oblique incidence angle $\theta_s$ | $\lvert S_{21}\rvert$ /dB | $\angle S_{21}$ | Wz /mm | Wc /mm | Lc /mm | Ld /mm |
|---|---|---|---|---|---|---|---|
| 0,1 | 0° | -0.16 | -14° | 3.6 | 1.3 | 0.1 | / |
| 2 | 18° | -0.2 | -11° | 3.6 | 1.4 | 0.1 | / |
| 3 | 26° | -0.14 | -13° | 3.6 | 1.5 | 0.05 | / |
| 4 | 33° | -0.1 | -15° | 3.6 | 1.5 | 0.7 | 0.6 |
| 5 | 39° | -0.18 | -12° | 3.6 | 1.5 | 0.9 | 0.8 |

## 4.3 Experimental Verification

Finally, in order to validate the developed ultra-thin Huygens element and its feasibility in conformal TAs, an array with a larger aperture than the one discussed in the last section is designed, fabricated and measured. It includes 16×17=272 elements, and its dimensions are given in Fig. 4-12. The cross-sectional size of the transmitting surface is 121.3 mm×144.5 mm. As discussed in last section, the oblique incidence angles are considered for the array design by dividing the straight section into 5 zones denoted as A, B, C, D and E, as given in Fig. 4-12 (b). Then, each element listed in Table 4-2 is re-simulated under 4 oblique angles, i.e. 14° (Zone B), 25° (Zone C), 33° (Zone D), 39° (Zone E). The unfolded transmitting surface is fabricated using standard PCB technology on low-cost Wangling F4B substrates (Dielectric Constant 3.55, tanδ = 0.0027). Due to its ultra-thin

profile which is only 0.5 mm ($\lambda_0/60$ at 10 GHz), it can be easily bent onto a 3-D printed cylindrical frame. Photographs of the TA prototype are shown in Fig. 4-13.

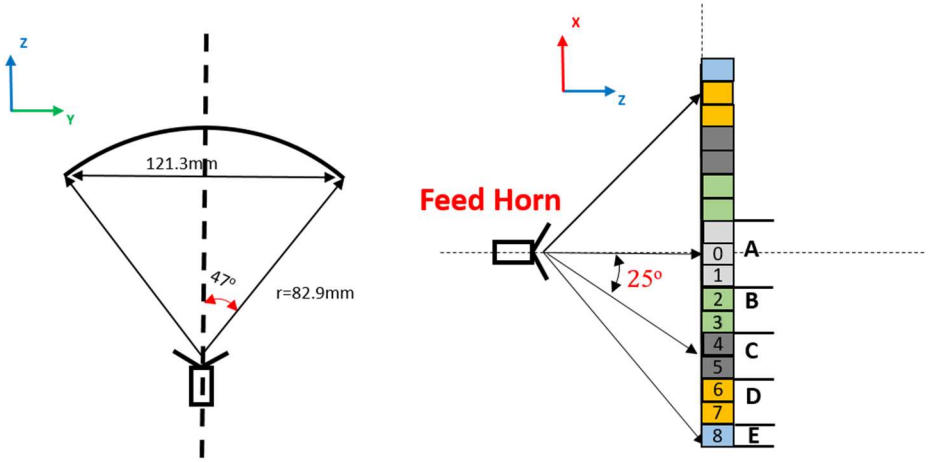


Fig. 4-12 Sketch of the cylindrical TA with larger aperture size. (a) Circular section. (b) Straight section.

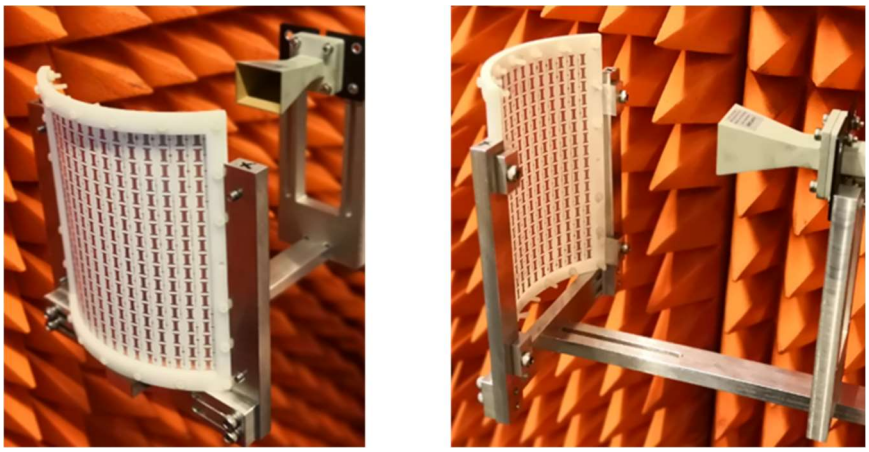

(a) (b)

Fig. 4-13 Photographs of the conformal TA prototype. (a) Front View. (b) Back View.

The input reflection coefficients of the TA are measured and compared with the simulated one, as plotted in Fig. 4-14. It can be seen that they are below -10 dB from 9.5 GHz to 10.5 GHz. Far-field radiation patterns are measured using a Microwave Vision Group

(MVG) compact range antenna measurement system located at University of Technology Sydney, Australia.

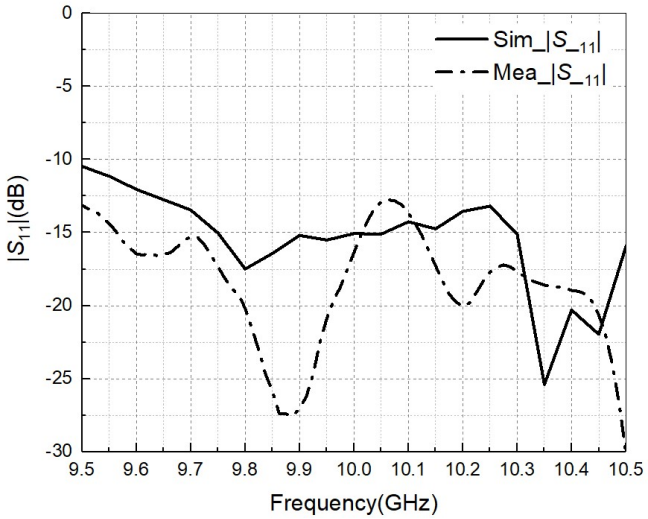


Fig. 4-14 Simulated and measured results of input reflection coefficients.

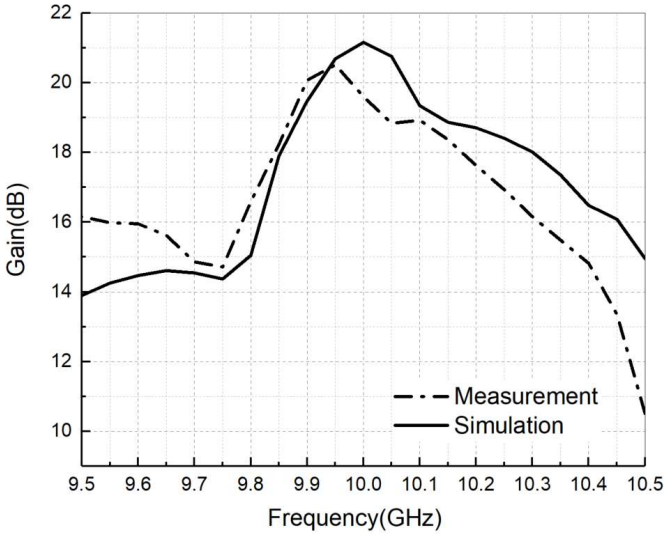


Fig. 4-15 Simulated and measured gains at boresight versus frequency.

The simulated and measured realized gains versus frequency are also found and plotted in Fig. 4-15. The peak gain appears at 10 GHz in simulation with 21.2 dBi, achieving a 54% antenna efficiency. For the measured results, the maximum gain is at 9.95 GHz with a value of 20.6 dBi, corresponding to a 47% antenna efficiency. The 3-dB gain bandwidth

is 3.7% (9.83 GHz -10.2 GHz). As discussed in Section 4.1, Huygens element for a specific transmission phase corresponds to a unique pair of electric and magnetic surface impedance values. Since the electric and magnetic surface impedance usually vary with the frequency, the Huygens element with a specific transmission phase can only be maintained in a very narrow bandwidth. Therefore, due to the phase compensation requirement, the 3-dB bandwidth of the TA is narrow. The simulated and measured E- and H- plane radiation patterns at 9.95 GHz are compared in Fig. 4-16 (a) and (b), respectively. Good agreement can be found except for a slight beam tilt of about 1°. The measured cross-polarization levels for two planes are both lower than -15 dB. The simulated cross-polarization levels are very low, so they are not shown in the figures.

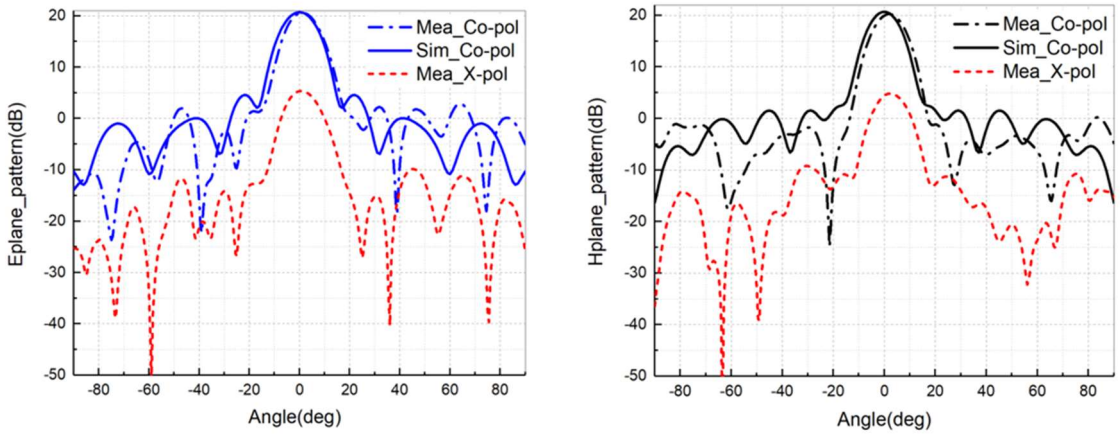


(a) (b)

Fig. 4-16 Simulated and measured patterns. (a) E plane. (b) H plane.

The slight beam tilt and the discrepancy on the realized gains can be mostly attributed to the fabrication inaccuracies in the 3-D printed cylindrical frame that have effects on the curvature of the transmitting aperture. Furthermore, there would be some alignment errors and the low-cost PCB board may have a varied dielectric constant from the datasheet.

To the best of the authors' knowledge, this is the first conformal TA with the thinnest element and a high aperture efficiency ever reported. The dual-layer structure without any vias is also an important innovation suitable for other TAs where a thin transmitting panel is needed. We compare the results of the developed work with those of other reported TAs with thin elements, as given in Table 4-5. It can be seen that the proposed one has the thinnest structure while a very high aperture efficiency.

Table 4-5 Comparison of proposed design with referenced TAs

| Ref. No. | Dielectric Constant | Number of layers | Electrical thickness | Vias | Array Contour | Aperture Efficiency |
|---|---|---|---|---|---|---|
| [5] | 2.2 | 3 | $\lambda_0/5$ | N. | Planar | 40.7% |
| [13] | 3.55 | 3 | $\lambda_0/14$ | N. | Planar | 30% |
| [32] | 2.55 | 2 | $\lambda_0/10$ | Y. | Planar | 40% |
| [79] | 4.3 | 2 | $\lambda_0/10$ | N. | Planar | 26% |
| Chapter 3 | 2.2 | 3 | $\lambda_0/25$ | N. | Cylindrical | 25.1% |
| **This work** | 3.55 | 2 | $\lambda_0/60$ | N. | Cylindrical | 47% |

## 4.4 Conclusion

In order to meet the low-profile demand on array elements for conformal TA designs, Huygens metasurface theory is employed in this work to achieve both an ultra-thin array element and a high aperture efficiency. The developed Huygens element consists of two metal layers with an entire thickness of 0.5 mm ($\lambda_0/60$ at 10 GHz) and without any metallic vias. By tuning magnetic and electric responses properly, eight elements are designed to cover a quantized 360$^o$ phase range with a maximal 1.67 dB loss. Based on these elements, a small conformal TA is constructed, where the oblique incidence on the array aperture is considered to enhance the antenna's performance. Finally, a cylindrically conformal TA with a larger aperture size is simulated and fabricated with a 20.6 dBi measured gain and a 47% aperture efficiency.

# Chapter 5: Ultrawideband Conformal Transmitarray Employing Connected Slot-Bowtie Elements

Even though there are some reported works on UWB planar TAs [46]-[47], the reported array elements consist of dual-layer radiators connected by microstrip lines or vias with a ground plane in the middle, thereby requiring a high alignment accuracy. This could be a potential issue for higher frequency TA designs and conformal designs.

In this chapter, inspired by the potential performance of "infinite bandwidth" from connected array theory [89]-[92], an UWB TA using connected slot-bowtie is presented for the first time. Since the ground plane is not essential in the TA element, it naturally keeps the "infinite bandwidth" property of connected arrays. The proposed element can achieve a high transmission efficiency (higher than -3 dB) from 6 GHz to 17 GHz with a 360° phase shifting range at the highest frequency point. The reduced bandwidth compared to "infinite" is due to the requirement of phase compensations for TA elements, where in this design vertical meander slot-lines are used. A planar UWB TA based on the proposed elements from 6 GHz to 17 GHz is theoretically simulated and measured with an array size of $4.3\lambda_0$ by $4.3\lambda_0$ ($\lambda_0$ is the free space wavelength at 17 GHz). The radiation patterns of the prototype are measured from 8.5 GHz to 17 GHz due to the limitation of our university facilities. Good agreement has been obtained between simulation and experiment. The measured antenna efficiency is from 38% to 60% with a peak gain of 20.2 dBi. Compared to [46], the proposed planar TA can achieve a similar gain but with

a smaller size, thereby achieving a higher efficiency. Furthermore, due to the simple structure of the proposed element, it is suitable for conformal TAs. Subsequently, a conformal prototype is also fabricated and measured, showing good agreement with the simulated patterns from 8.5 GHz to 17 GHz. To the best of the authors' knowledge, this is the first reported conformal TA with an UWB property.

The chapter is organized as follows. In section 5.1, a detailed connected array element design is developed and applied to a planar TA. A conformal TA based on the proposed element is simulated and analysed in section 5.2. A discussion on the feed sources of both planar and conformal TAs is presented in section 5.3. The chapter concludes in section 5.4.

## 5.1 Ultrawideband Planar TA

### *5.1.1 Ultrawideband TA Theory*

As introduced before for TAs, a phase compensation needs to be applied along the aperture to transform an incident spherical wave into a planar wave to a desired direction (Fig. 5-1).

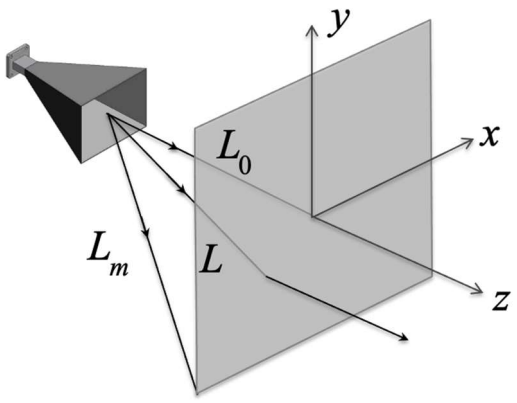


Fig. 5-1 TA geometry.

To achieve the UWB performance, TA calls for an UWB element with two properties. First, the element should operate with a high transmission efficiency within the band, i.e., the amplitude of transmission coefficient should be greater than -3 dB. Second, assuming the beam transmitted by the array is directed to the boresight, the relative phase compensation value along the array should be a linear function to both frequency and spatial delay, as illustrated in Fig. 5-1. Their relationship is given in (5-1),

$$\Delta\varphi = k(L_m - L_0) = \frac{L_m - L_0}{c} f\ 2\pi \tag{5-1}$$

where $c$ is the light speed, $f$ is the frequency and $k$ is the free space wavenumber. If we denote $\Delta L = (L_m - L_0)$, and we normalize the phase difference to frequency, we have the phase delay as follows:

$$\Delta\varphi_f = \frac{\Delta\varphi}{f} = 2\pi\frac{\Delta L}{c} \tag{5-2}$$

We can achieve consistent beam characteristics in a large frequency range, as long as the phase delay keeps a linear relation with the size variation and has a constant gradient ($2\pi/c$) across the whole operating frequency band.

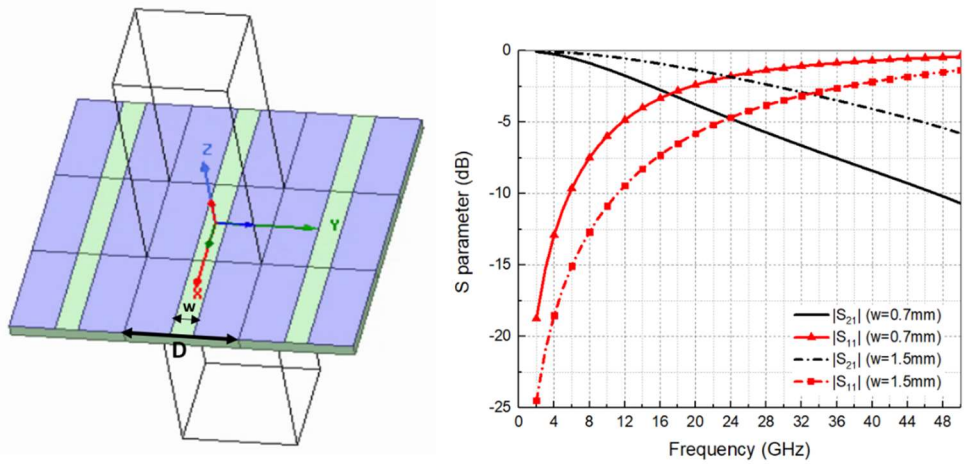


(a) (b)

Fig. 5-2 Traditional connected array element with a constant slot width. (a) Schematic. (b) S parameters.

### *5.1.2 Ultrawideband TA Element Design*

At the first step, the connected array theory is employed to design the element providing an ultra-wide passband because of its almost infinite bandwidth [90]. For a traditional connected slot-array along x-axis as shown in Fig. 5-2 (a), its element is analysed in a periodic boundary condition with a y-polarized incident wave. The substrate thickness is chosen as 1 mm with a dielectric constant $\varepsilon_r = 2.2$ and loss tangent of 0.0009.

Generally, it shows low-pass filter characteristics with an ultra-wide band, and its stop frequency point is related to the slot width *w*. As shown in Fig. 5-2 (b), under the same periodicity *D*=4 mm, the wider the slot is, the wider the transmission bandwidth ($|S_{21}| \geq$ -3 dB) will be. The -3-dB stop frequency points for *w*=0.7 mm and *w*=1.5 mm are 16 GHz and 32 GHz, respectively. For the TA design, however, the slots cannot be too wide as they will be connected to vertical meander slot lines with the same slot width as will be shown in the following paragraphs. If the slot width *w* is too large, the whole volume of the meander slot line would increase in order to produce a 360° phase range. Thus, the dimension of the slot should be chosen as a compromise between these two opposite needs. Alternatively, one can increase the bandwidth by using a bowtie shape as described in Fig. 5-3 (a).

The results of transmission and reflection coefficients in Fig. 5-3 (b) are referred to the connected slot-bowtie with the periodicity *D*=4 mm. The slot-bowtie is still connected along x axis, and the slot width *w* is linearly tapered from 0.7 mm to 3.6 mm from the centre to the edge of the element; at the element boundary, the profile has a discontinuity with a width of *ws*=1.8 mm, which gives an additional degree of freedom in the design. Under the incident wave conditions as the one in Fig. 5-2, the amplitude of $|S_{21}|$ possesses a -3-dB ultra-wide band from 2 GHz to 35 GHz (Fig. 5-3 (b)).

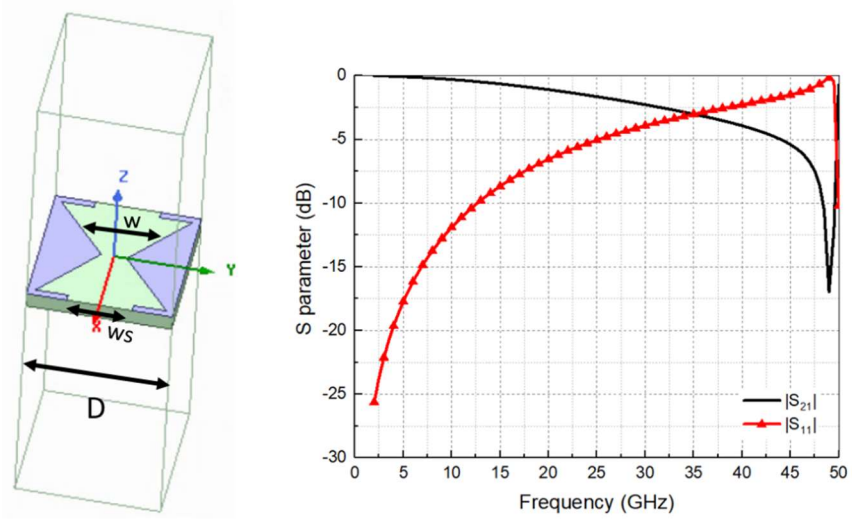


(a) (b)

Fig. 5-3 Connected slot-bowtie dipole. (a) Schematic. (b) Simulated S parameters.

For compensating the phase, we adopt the true-time-delay-line concept which allows phase controls over a wideband [25]. To this end, a vertical meander slot-line is introduced in *y0z* plane as shown in Fig. 5-4 (a), where horizontal slot offset-length *a* can be varied in order to change the transmission phase in a range of 360° across the operating bandwidth.

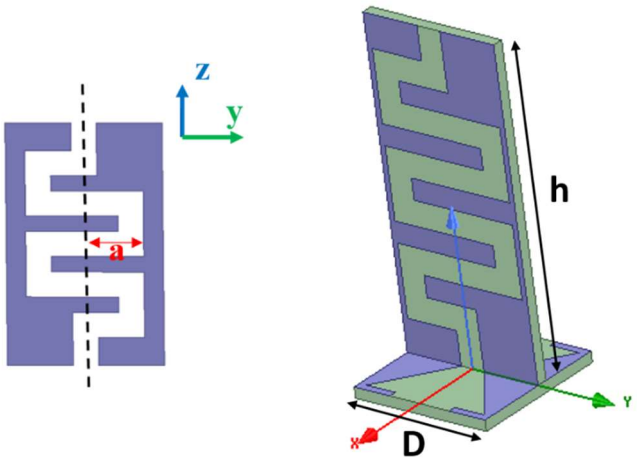


(a) (b)

Fig. 5-4 (a) Schematic of the meander slot-line. (b) Final TA element.

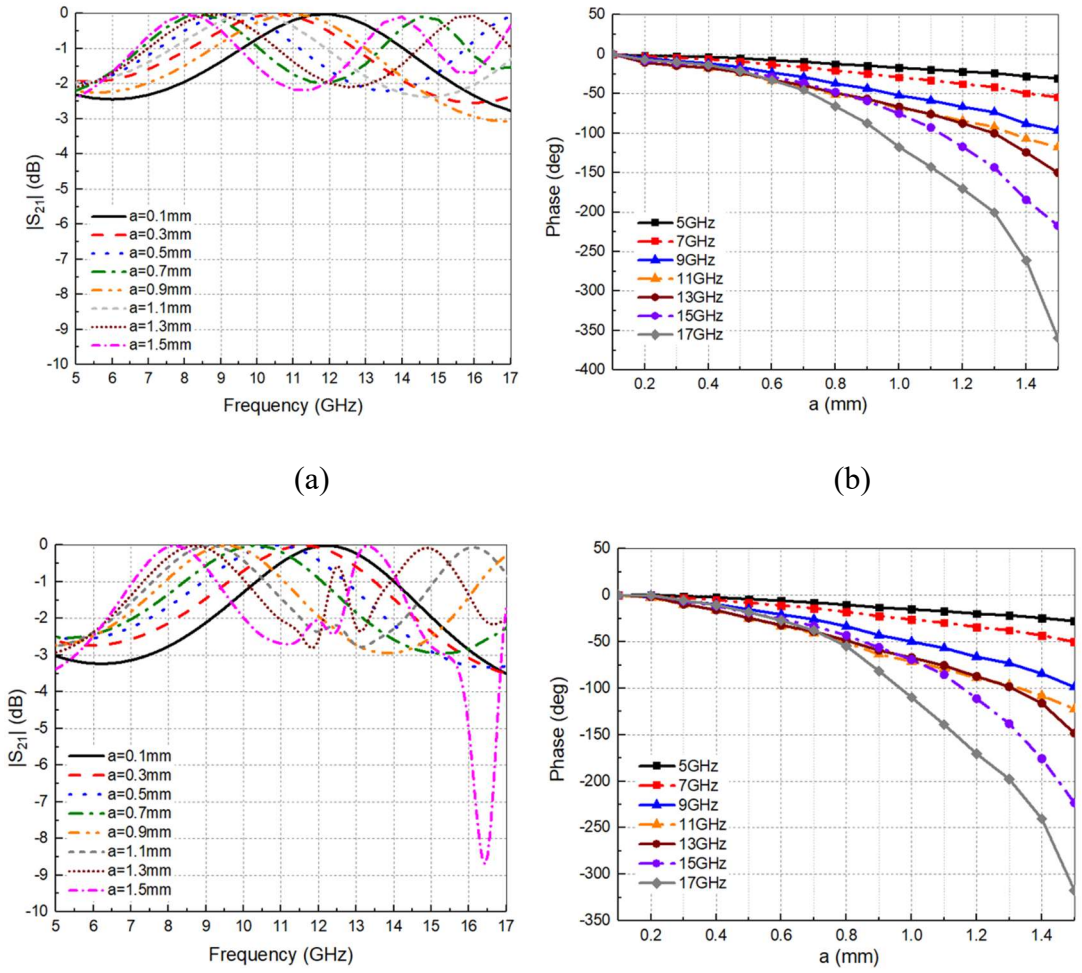


Fig. 5-5 (a) |S21| of final TA element with different meander line lengths. (b) Phase variation Δφ versus element size a. (c) |S21| under 30° incidence angle. (d) Phase variation Δφ under 30° incidence angle.

The final 3-D element model is shown in Fig. 5-4 (b). The connected slot-bowtie, used to achieve UWB transmission characteristics, is vertically connected to a meander slot-line, where the meander slot width matches the orthogonal slot-bowtie centre width. Both metal sheets are printed on a 1-mm-thick substrate with a dielectric constant $\varepsilon_r = 2.2$ and loss tangent of 0.0009, then they are soldered together. The periodicity $D$ is optimized as 4 mm (around $\lambda_0/4$ at the highest operating frequency 17 GHz), and the vertical height $h$

is 9 mm ($0.5\lambda_0$ at 17 GHz). Simulated amplitudes and phases of transmission coefficients are compared in Fig. 5-5.

Due to the effect of the meander slot-line, the bandwidth of the 3-dB transmission loss is reduced to the range of 5 GHz to 17 GHz as shown in Fig. 5-5 (a) compared to the pure connected slot-bowtie which is 2 GHz-35 GHz. The 360° full phase range can be achieved at the highest frequency point 17 GHz as shown in Fig. 5-5 (b). To consider the effects of oblique incidence on the element performance, these elements are also simulated under a 30° oblique incidence angle. The $S_{21}$ amplitude and phase results are shown in Fig. 5-5 (c) and (d). Comparing with Fig. 5-5 (a) and (b), it can be seen that the transmission amplitude deteriorates slightly, but it is still in the 3-dB range for almost all the frequency points. For the transmission phase, only the phase range at 17 GHz is reduced from 360° to 320°, while it is almost unchanged for other frequencies. Then we normalize the phase compensation values to the frequency according to (5-2), the phase delays at different frequencies (Fig. 5-6) show a quasi-linear dependency to the slot length, and the values at different frequencies for each slot length *a* change slightly, satisfying the UWB requirements as discussed before. It should be noted that the meander lines may have effects on the radiation properties of the slot-bowtie elements, however, their effects are taken into consideration in the 3-D simulation and negligible impacts on the overall antenna performance are observed.

From Fig. 5-5 (b), it is obvious that the total phase range would be smaller when the frequency is lower, which is due to the fact that the variation of horizontal slot length *a* is electrically smaller at lower frequency, e.g., *a* is varied from $0.0017\lambda_{5GHz}$ to $0.025\lambda_{5GHz}$ at 5 GHz. Consequently, the phase delays are not calculated for frequency points below 7 GHz, and they are not plotted for normalizations in Fig. 5-6. At lower frequencies, since the electrical size of the entire TA aperture is small compared to the wavelength, the phase

variation range required is much less than 360°. Therefore, at the lower band the structure can still provide the needed phase compensation. To make the structure profile as low as possible, the slot-line is tightly meandered, which may introduce interference and coupling between adjacent slots. As a result, the phase delay at higher frequency deviates from the average relation line as shown in Fig. 5-6.

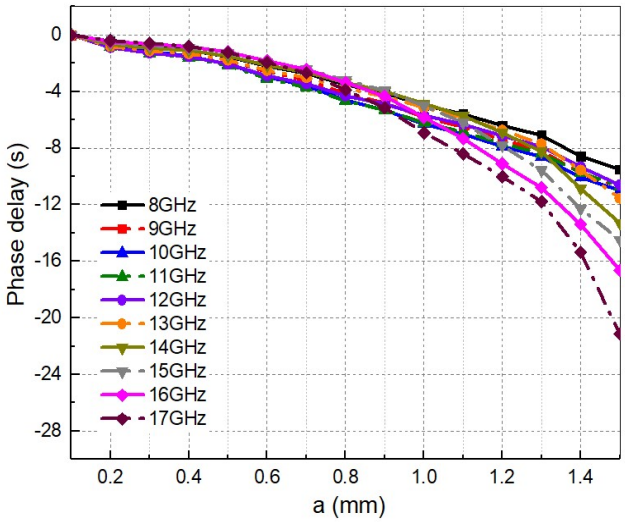


Fig. 5-6 Frequency-normalized phase $\Delta\varphi_f$ versus a.

For completeness, an ideal true-time-delay straight slot-line element model in Fig. 5-7 (a) has been simulated by full-wave analysis. Fig. 5-7 (b) shows the phase delay $\Delta\varphi_f$, changing the height $h$ of the vertical slot-line for phase tuning. The phase delay $\Delta\varphi_f$ at different frequency points provide an ideal linear relation with $h$ and an almost unchanged gradient. Nevertheless, this model can only provide a 283° phase range at 17 GHz when $h$ increases to 18 mm which is already twice the thickness of the structure shown in Fig. 5-4 (b). Therefore, the height $h$ needs to be increased further to achieve the full 360° phase range. Despite the linearity of the phase versus $h$ over the bandwidth, this solution is not convenient in practice since it increases the overall volume of the element significantly.

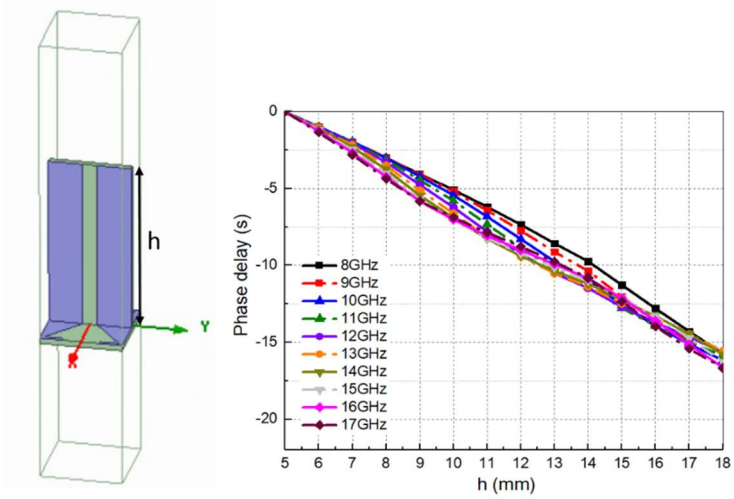


(a) (b)

Fig. 5-7 Element with true-time-delay slot-line. (a) Schematic. (b) Frequency-normalized phase $\Delta\varphi_f$ versus h.

### *5.1.3 Planar TA*

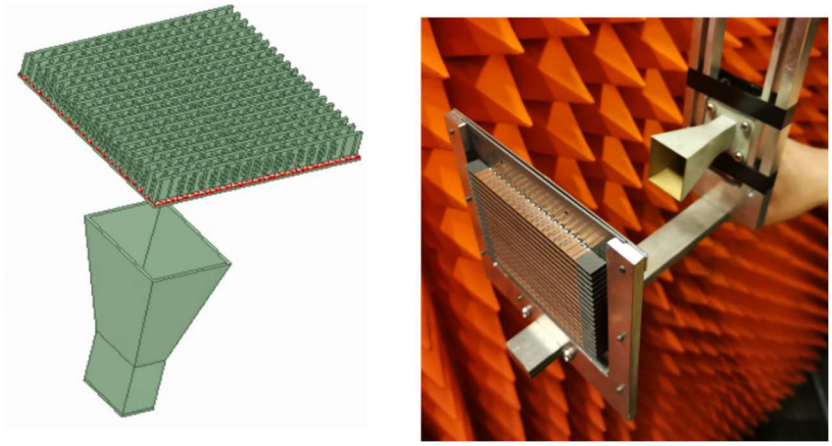

(a) (b)

Fig. 5-8 TA structure. (a) Model in HFSS. (b) Photo of the fabricated prototype.

A planar TA with 19×19=361 elements is constructed to verify the proposed UWB element; the model from HFSS and the photo of the fabricated prototype are shown in Fig. 5-8 (a) and (b), respectively. The horizontal and vertical boards are fabricated separately using a standard PCB technology. Then, each vertical board is assembled and

soldered on the horizontal base. Therefore, the smaller the distance between two adjacent vertical boards is, the harder the soldering would be. In this design, the distance between each board is the periodicity of element models, which is 4 mm. The size of the array is 76 mm by 76 mm which is $4.3\lambda_0$ by $4.3\lambda_0$ ($\lambda_0$ is the free space wavelength at 17 GHz). Two different standard gain horns, LB-112-10-C-SF (working from 6 GHz) and LB-75-10-C-SF (working from 10 GHz ) from A-INFO, are utilized to cover the lower and higher bands, respectively. The focal length is chosen as 58 mm, making the flare angle from the focal point to the edges of TA around ±33°. Because the -10-dB beamwidth of two feed horns would vary at different frequency points, the flare angle is chosen to match -10-dB beamwidth of the standard gain horn LB75-10 at 13.5 GHz. The input reflection coefficients of the TA have been simulated and measured from 6 GHz to 17 GHz, with results shown in Fig. 5-9 (b). Since the TA is a single-port device, the reflection coefficient is defined as how much of the incident power at the input port of the feeding antenna is reflected, as sketched in Fig. 5-9 (a). In the simulation, the reflection coefficient is calculated as the ratio of the power reflected back at the waveguide port of the feed horn and the input power. In measurement, we connect the feed horn of the TA to one-port of the vector network analyser (VNA) to obtain $|S_{11}|$. It can be seen that the measured amplitude of $S_{11}$ is below -10 dB from 6 GHz to 17 GHz. The average value is accurately reproduced by the simulation; the inaccuracies are probably due to the inaccuracies during the fabrication and implementation process.

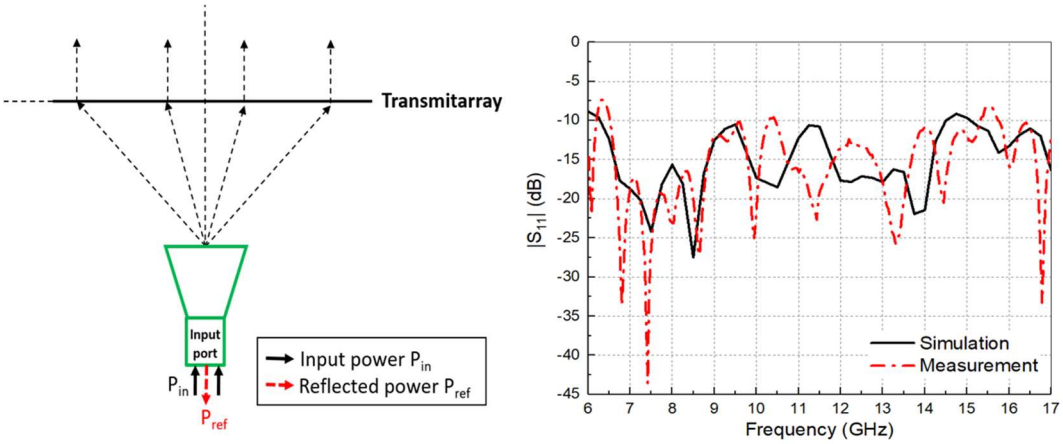


(a) (b)

Fig. 5-9 (a) The sketch of TA system. (b) Simulated and measured input reflection coefficients.

Besides, far-field radiation patterns were measured at University of Technology Sydney (UTS), Australia, using a compact range antenna measurement system designed by Microwave Vision Group (MVG). The simulated and measured E- and H- plane patterns at different frequency points are given in Fig. 5-10. Due to the limit of the operating frequency range of the measurement system, only patterns from 8.5 GHz to 17 GHz are obtained. It can be seen that consistent boresight radiation patterns are achieved across the band. The measured cross-polarization level is around -15 dB across the whole operating band. The simulated cross polarizations are not shown as they are very small. The measured cross-polarization level is usually higher than the simulated one due to the fabrication tolerance and the chamber dynamic range limitation.

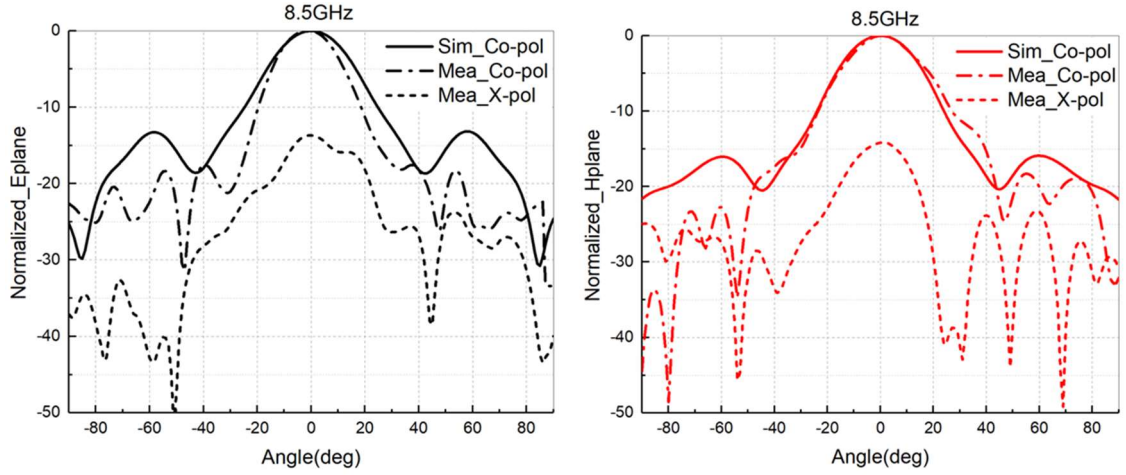
8.5GHz
Sim_Co-pol
Mea_Co-pol
Mea_X-pol
Normalized_Eplane
Angle(deg)
8.5GHz
Sim_Co-pol
Mea_Co-pol
Mea_X-pol
Normalized_Hplane
Angle(deg)

(a)

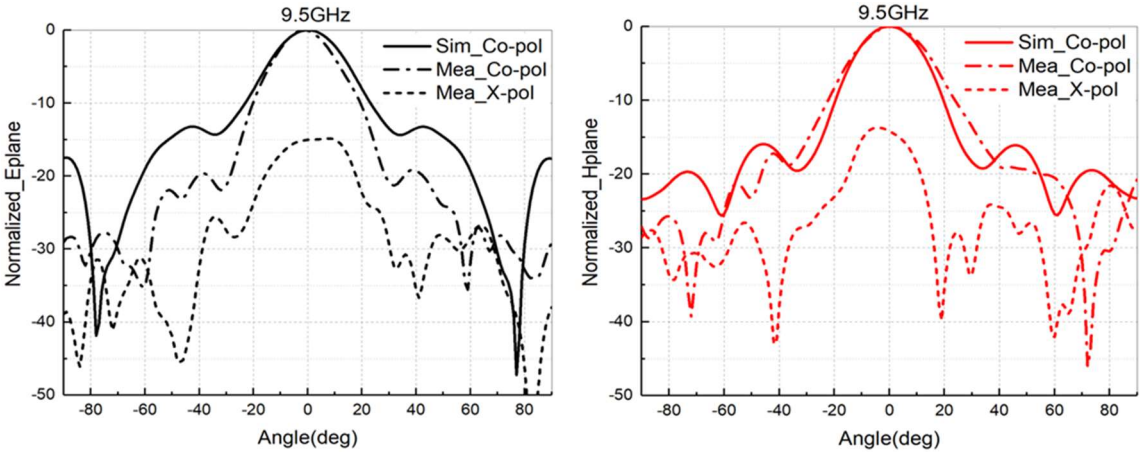
9.5GHz
Sim_Co-pol
Mea_Co-pol
Mea_X-pol
Normalized_Eplane
Angle(deg)
9.5GHz
Sim_Co-pol
Mea_Co-pol
Mea_X-pol
Normalized_Hplane
Angle(deg)

(b)

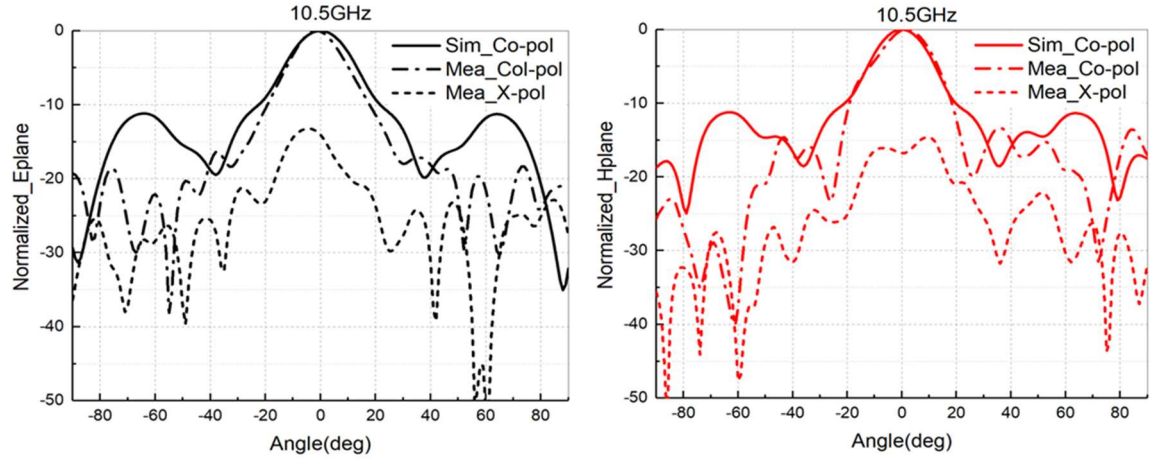
10.5GHz
Sim_Co-pol
Mea_Col-pol
Mea_X-pol
Normalized_Eplane
Angle(deg)
10.5GHz
Sim_Co-pol
Mea_Co-pol
Mea_X-pol
Normalized_Hplane
Angle(deg)

(c)

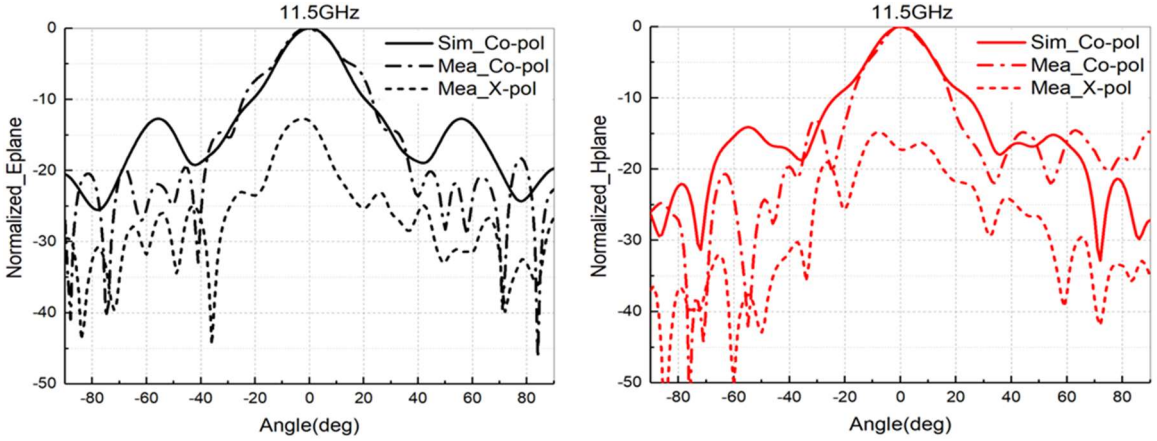
11.5GHz
Sim_Co-pol
Mea_Co-pol
Mea_X-pol
Normalized_Eplane
Angle(deg)
11.5GHz
Sim_Co-pol
Mea_Co-pol
Mea_X-pol
Normalized_Hplane
Angle(deg)

(d)

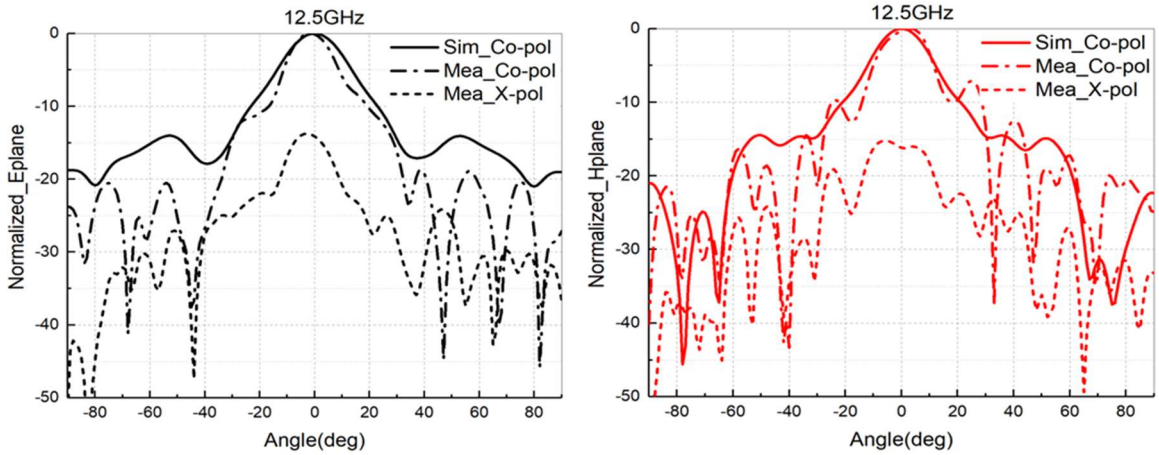
12.5GHz
Sim_Co-pol
Mea_Co-pol
Mea_X-pol
Normalized_Eplane
Angle(deg)
12.5GHz
Sim_Co-pol
Mea_Co-pol
Mea_X-pol
Normalized_Hplane
Angle(deg)

(e)

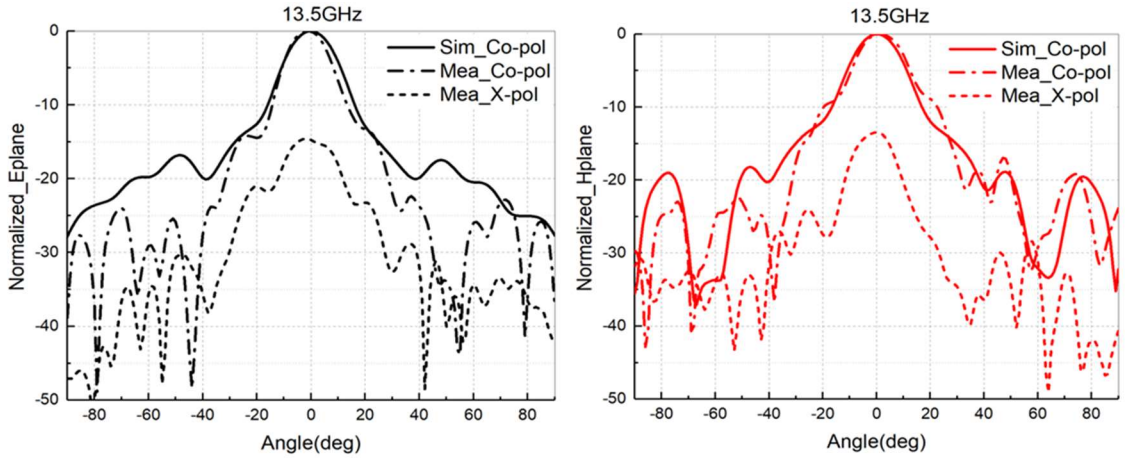
13.5GHz
Sim_Co-pol
Mea_Co-pol
Mea_X-pol
Normalized_Eplane
Angle(deg)
13.5GHz
Sim_Co-pol
Mea_Co-pol
Mea_X-pol
Normalized_Hplane
Angle(deg)

(f)

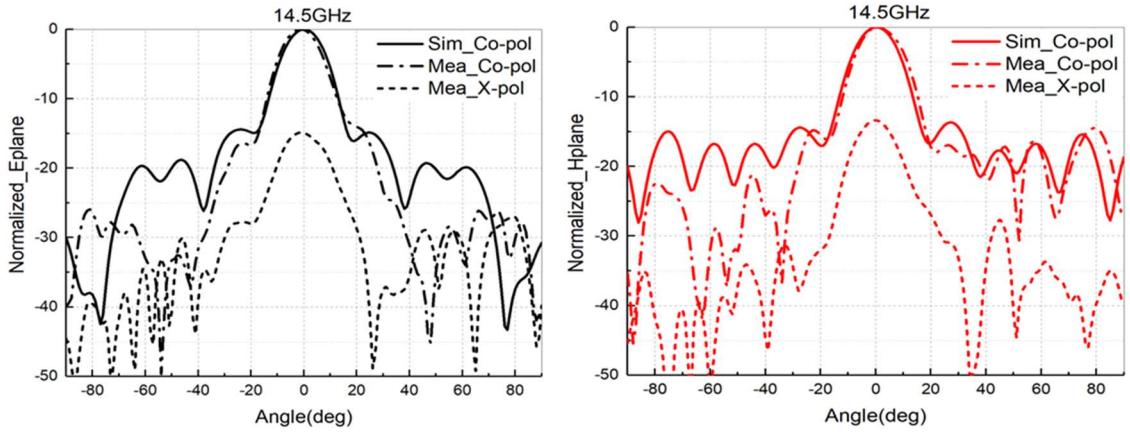


(g)

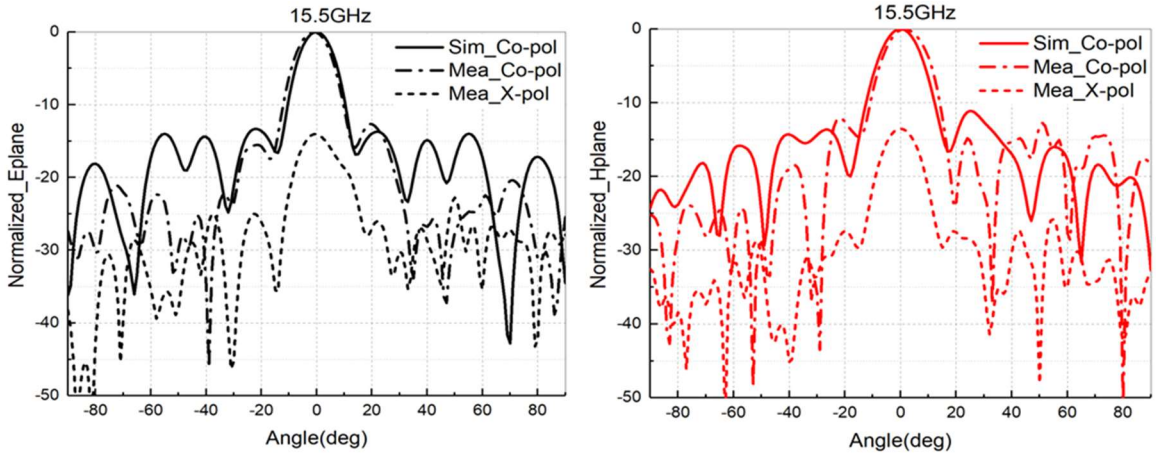


(h)

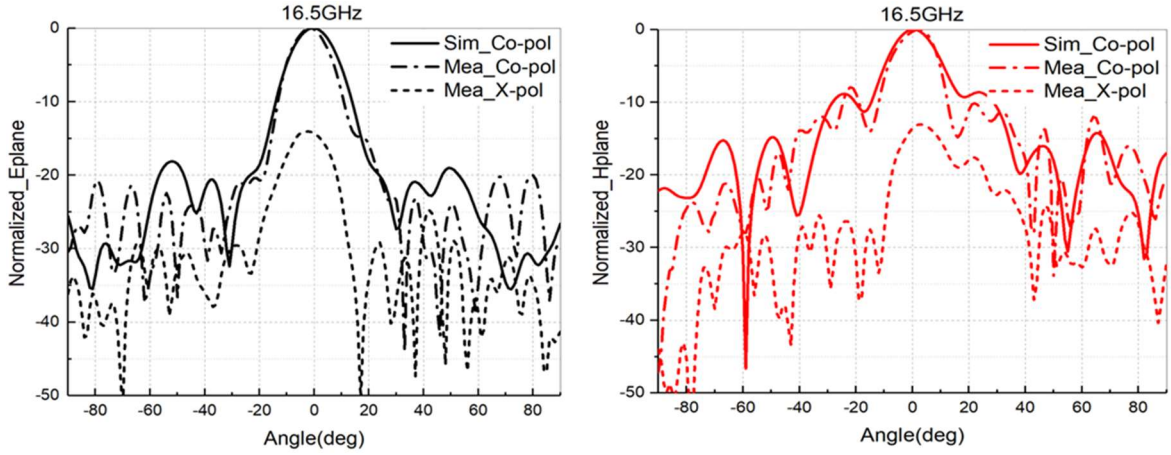


(i)

Fig. 5-10 Simulated and measured E-plane and H-plane patterns. (a) 8.5GHz. (b) 9.5GHz. (c) 10.5GHz. (d) 11.5GHz. (e) 12.5GHz. (f) 13.5GHz. (g) 14.5GHz. (h) 15.5GHz. (i) 16.5GHz.

The gain and efficiency versus frequency are shown in Fig. 5-11. The efficiency of the antenna is defined as the ratio of the gain and the maximum directivity of the array aperture, the latter obtained as $4\pi$ times the physical aperture area on square wavelength. The simulated and measured results agree reasonably well. It can be observed that the gain increases with frequency with some fluctuations. Ideally, for the TA with a fixed physical aperture size, the peak gain should increase monotonically with frequency to achieve a relatively stable antenna efficiency. The reasons for the undesired fluctuations include the variation of the aperture tapering efficiency over the bandwidth obtained from two feed horns, the variation of the element loss and phase compensation errors over frequency bands. This can be partially addressed by designing an UWB feed antenna with steady illumination efficiency. The measured antenna efficiency is from 38% to 60% with a peak gain of 20.2 dBi.

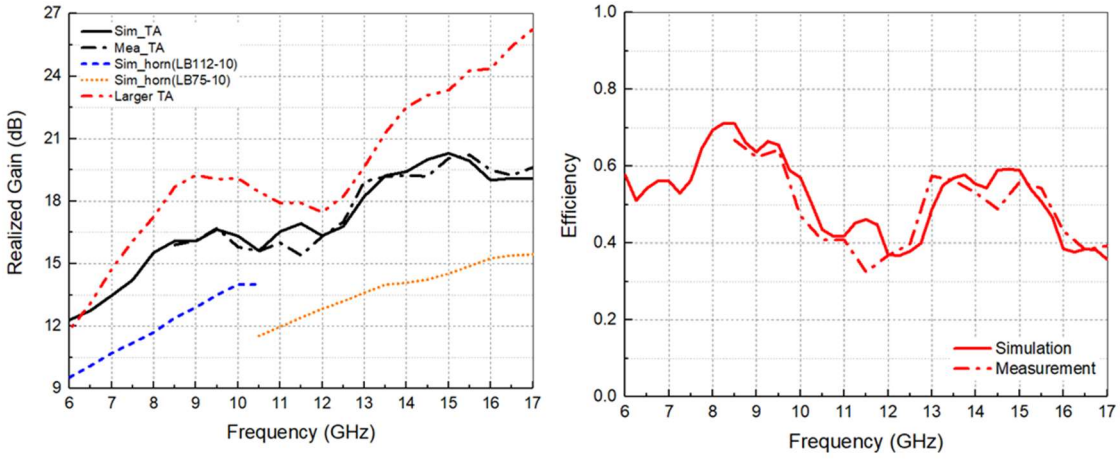


(a) (b)

Fig. 5-11 Simulated and measured results. (a) Realized gain versus frequency. (b) Efficiency versus frequency.

It can be noticed from Fig. 5-11 (a) that the gain enhancement is about 1.5-5.5 dB from 6 GHz to 17 GHz. This enhancement can be further increased by using a larger size of TA. To show this, a planar TA with 38×38 elements ($8.6\lambda_{highest} \times 8.6\lambda_{highest}$) has been designed

with the focal length chosen as 160 mm. The gain curve of this larger one is introduced for comparison in Fig. 5-11 (a). The gain improvement of 2.3-10.8 dB with respect to the feed horn is obtained with this larger array in the bandwidth of 6 GHz-17 GHz.

## 5.2 Ultrawideband Conformal TA

Since the TA element developed in this work has a simple structure and the substrate thickness of the connected slot-bowtie dipole array can be very thin, it is suitable for conformal TAs. The modified element model is shown in Fig. 5-12 (a). The connected slot-bowtie is printed on a substrate with 0.5 mm thickness, which is thin enough for conformal fabrication. The dielectric constant is 2.2 and loss tangent is 0.0009. The substrate thickness for supporting vertical meander slot-lines is still 1 mm. From the whole conformal array perspective, each element has negligible curvature, so its transmission performance is almost unchanged from the planar one. For validation, a cylindrical TA is constructed in ANSYS HFSS, as shown in Fig. 5-12 (b). Two different standard gain horns, i.e., LB-112-10-C-SF and LB-75-10-C-SF from A-INFO, are utilized to cover the lower and higher bands, respectively (the same used for the planar structure).

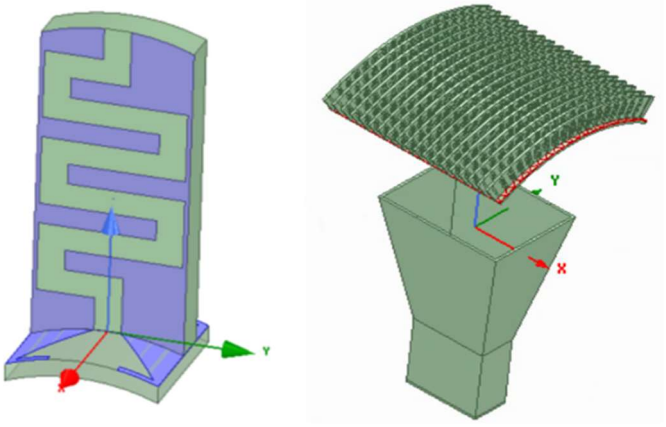

(a) (b)

Fig. 5-12 Conformal TA structure. (a) Curved element model. (b) Conformal array model in HFSS.

The sketch of the conformal TA is shown in Fig. 5-13 (a) and its fabricated prototype is shown in Fig. 5-13 (b). The flare angle of array is ±33° with 19×19 elements wrapped on the surface. The element periodicity $D$ is 4 mm and the focal length $r$ is 66 mm. Therefore, the curvature of single element is only 3.5°, as calculated from (5-3). In practical applications, the size of conformal TAs would be even larger with a greater focal length $r$ in order to achieve a higher gain. In that case, the element curvature would become smaller, making it negligible in affecting the array performance.

$$\alpha = \frac{D}{\pi r} \cdot 180^{o} \tag{5-3}$$

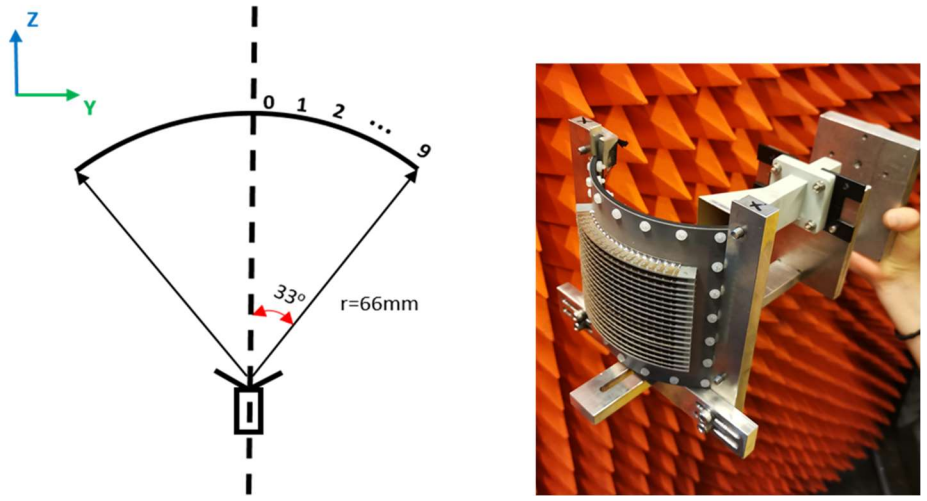


(a) (b)

Fig. 5-13 (a) Sketch of the conformal TA. (b) Fabricated prototype.

The input reflection coefficients of TA are simulated and measured from 6 GHz to 17 GHz, as shown in Fig. 5-14. It can be seen that the measured $|S_{11}|$ is below -10 dB from 6 GHz to 17 GHz. The simulated and measured E- and H- plane patterns at different frequency points are given in Fig. 5-15. Due to the limit of the operating frequency range

of the measurement system, only 8.5 GHz-17 GHz results are measured. It can be seen that consistent boresight radiation patterns are achieved across the band with lower than -15-dB cross-polarization levels. The gain and efficiency versus frequency with different feed horns are shown in Fig. 5-16. The simulated and measured results agree reasonably well. The measured realized gain is from 12 dBi to 20.2 dBi, and the measured efficiency is from 39% to 76%.

For both planar and conformal TAs, the measured efficiency fluctuates with frequency. This is partially because the gain and beamwidth of the standard horns are not stable with frequencies, thereby resulting in different illumination efficiencies. To address this issue, a feed source antenna with a stable beamwidth across the ultra-wide band can be adopted. The reason to use two standard gain horns in this work is to validate the feasibility of the technology using connected elements to achieve UWB performance.

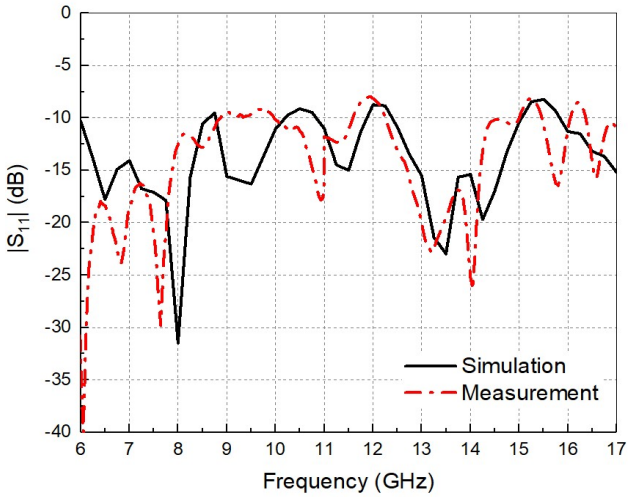


Fig. 5-14 Simulated and measured input reflection coefficients.

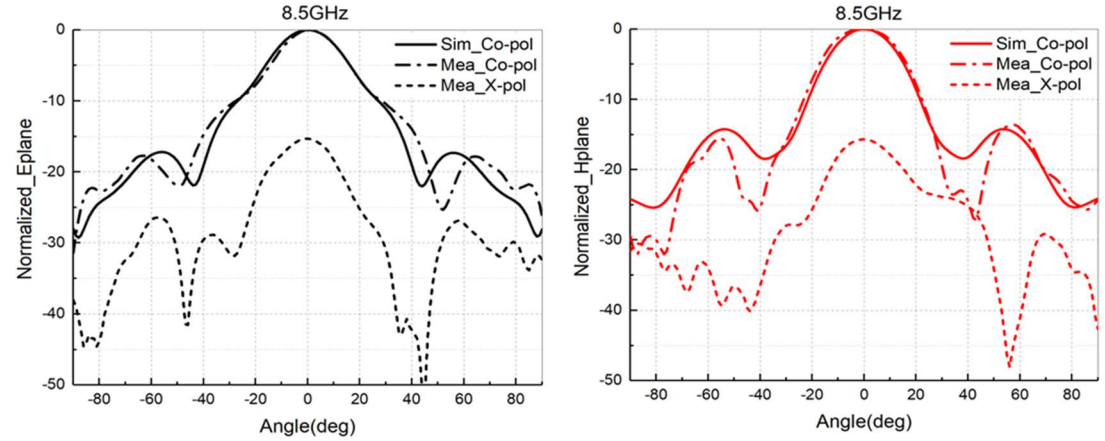
8.5GHz
Sim_Co-pol
Mea_Co-pol
Mea_X-pol
Normalized_Eplane
Angle(deg)
8.5GHz
Sim_Co-pol
Mea_Co-pol
Mea_X-pol
Normalized_Hplane
Angle(deg)

(a)

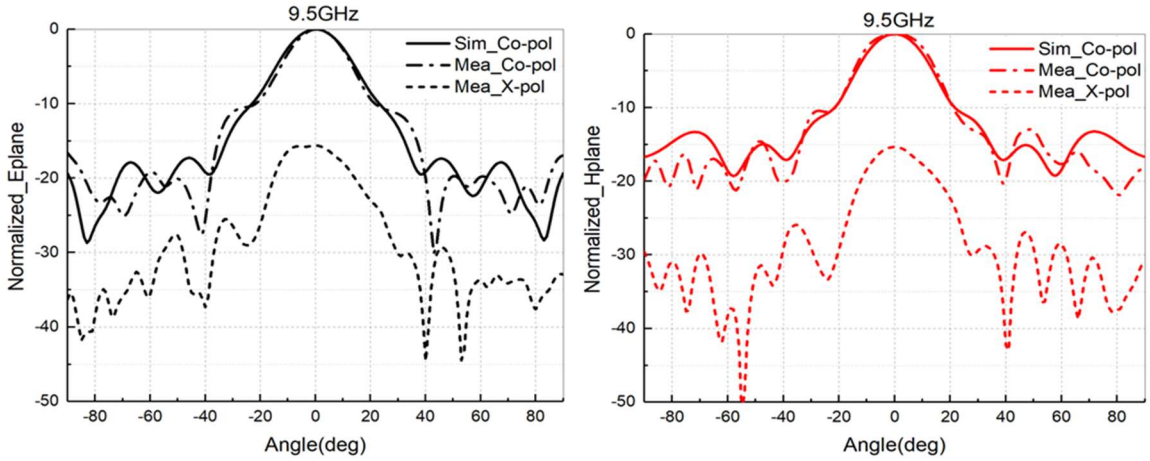
9.5GHz
Sim_Co-pol
Mea_Co-pol
Mea_X-pol
Normalized_Eplane
Angle(deg)
9.5GHz
Sim_Co-pol
Mea_Co-pol
Mea_X-pol
Normalized_Hplane
Angle(deg)

(b)

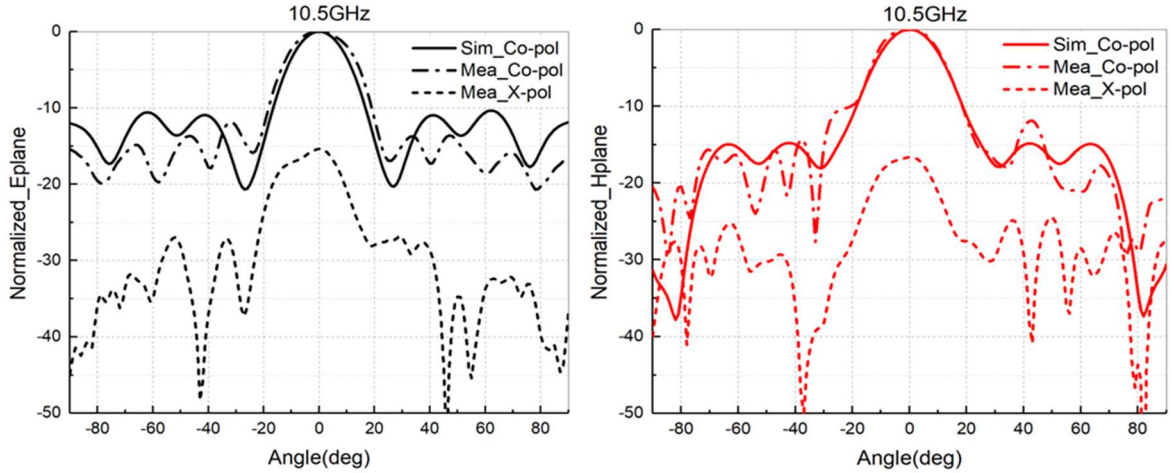
10.5GHz
Sim_Co-pol
Mea_Co-pol
Mea_X-pol
Normalized_Eplane
Angle(deg)
10.5GHz
Sim_Co-pol
Mea_Co-pol
Mea_X-pol
Normalized_Hplane
Angle(deg)

(c)

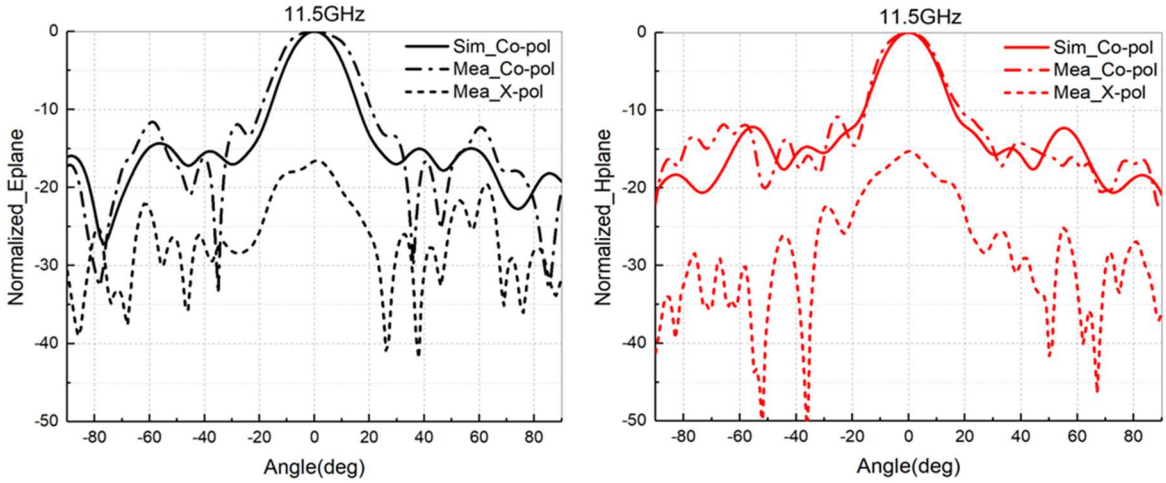
11.5GHz
Sim_Co-pol
Mea_Co-pol
Mea_X-pol
Normalized_Eplane
Angle(deg)
11.5GHz
Sim_Co-pol
Mea_Co-pol
Mea_X-pol
Normalized_Hplane
Angle(deg)

(d)

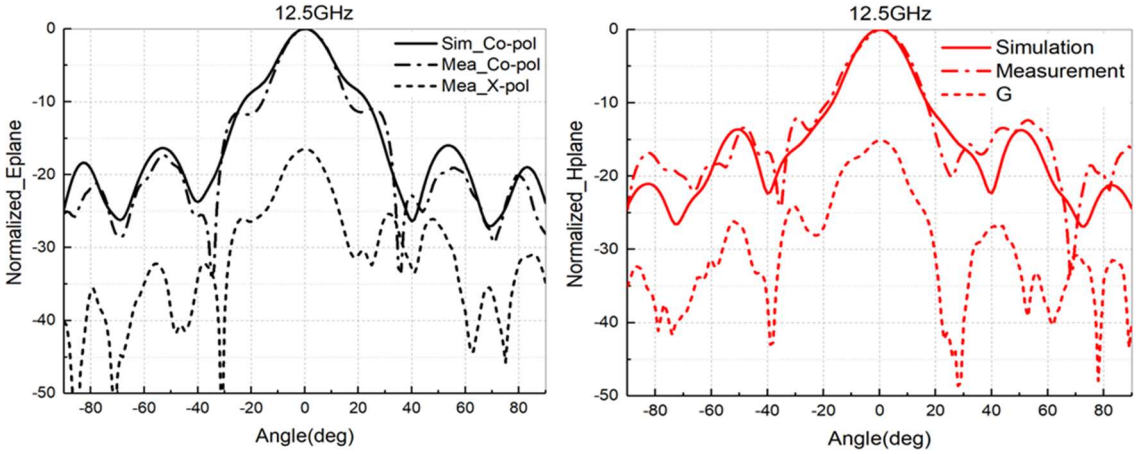
12.5GHz
Sim_Co-pol
Mea_Co-pol
Mea_X-pol
Normalized_Eplane
Angle(deg)
12.5GHz
Simulation
Measurement
G
Normalized_Hplane
Angle(deg)

(e)

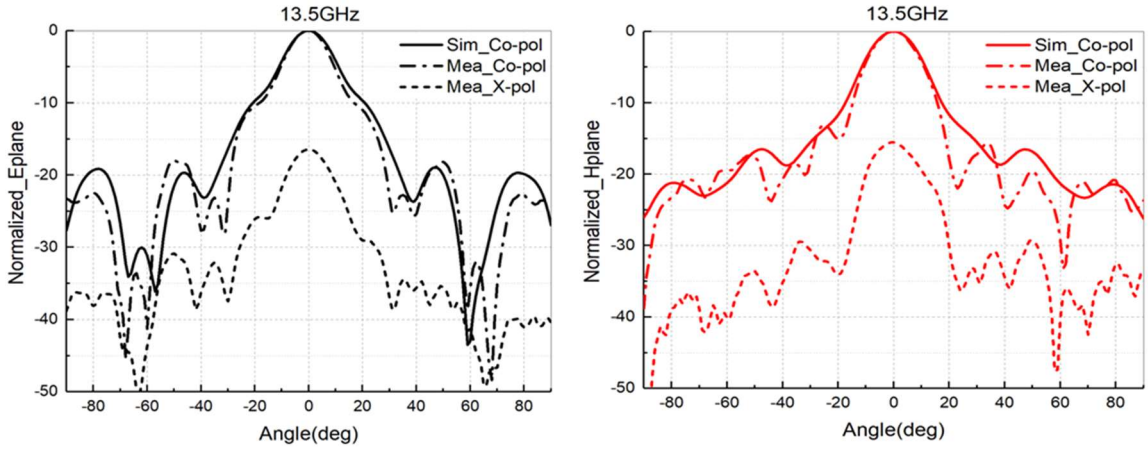
13.5GHz
Sim_Co-pol
Mea_Co-pol
Mea_X-pol
Normalized_Eplane
Angle(deg)
13.5GHz
Sim_Co-pol
Mea_Co-pol
Mea_X-pol
Normalized_Hplane
Angle(deg)

(f)

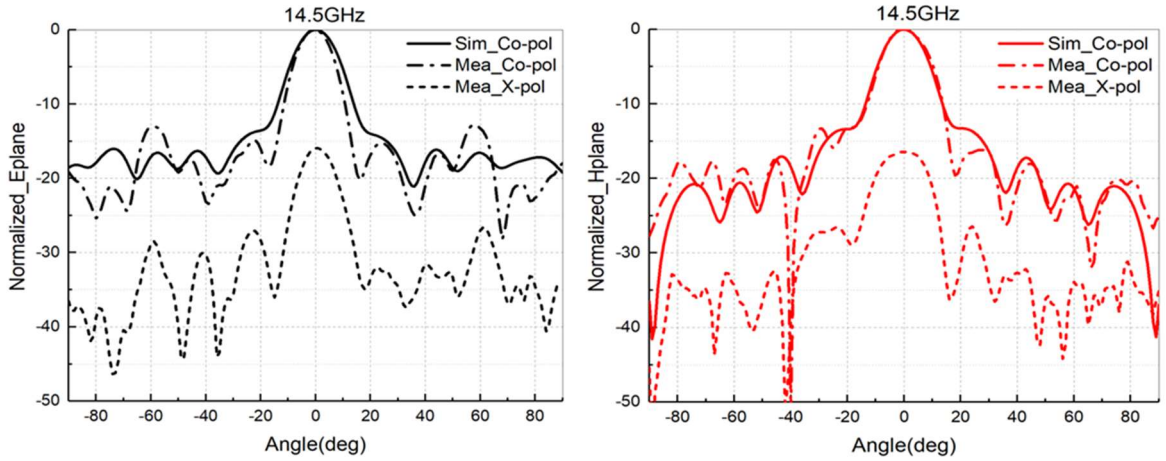
14.5GHz
Sim_Co-pol
Mea_Co-pol
Mea_X-pol
Normalized_Eplane
Angle(deg)
14.5GHz
Sim_Co-pol
Mea_Co-pol
Mea_X-pol
Normalized_Hplane
Angle(deg)

(g)

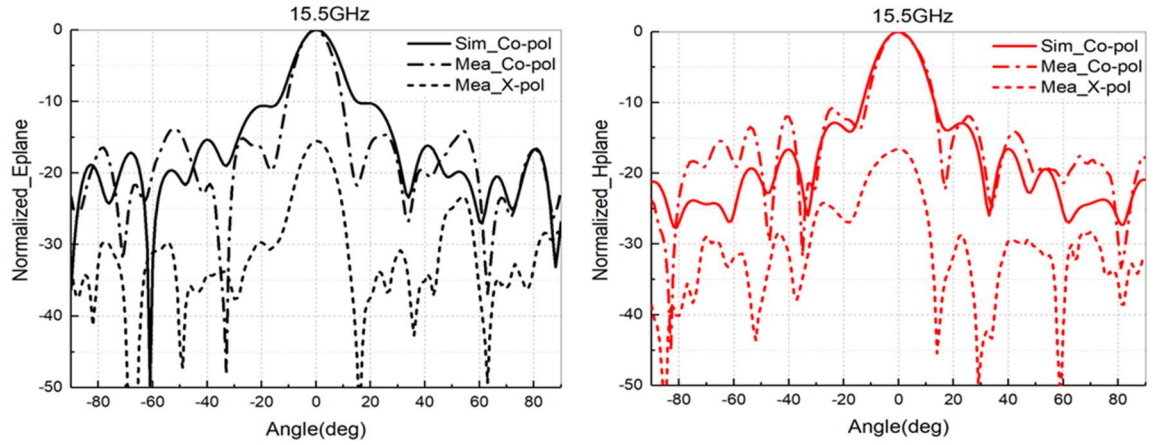
15.5GHz
Sim_Co-pol
Mea_Co-pol
Mea_X-pol
Normalized_Eplane
Angle(deg)
15.5GHz
Sim_Co-pol
Mea_Co-pol
Mea_X-pol
Normalized_Hplane
Angle(deg)

(h)

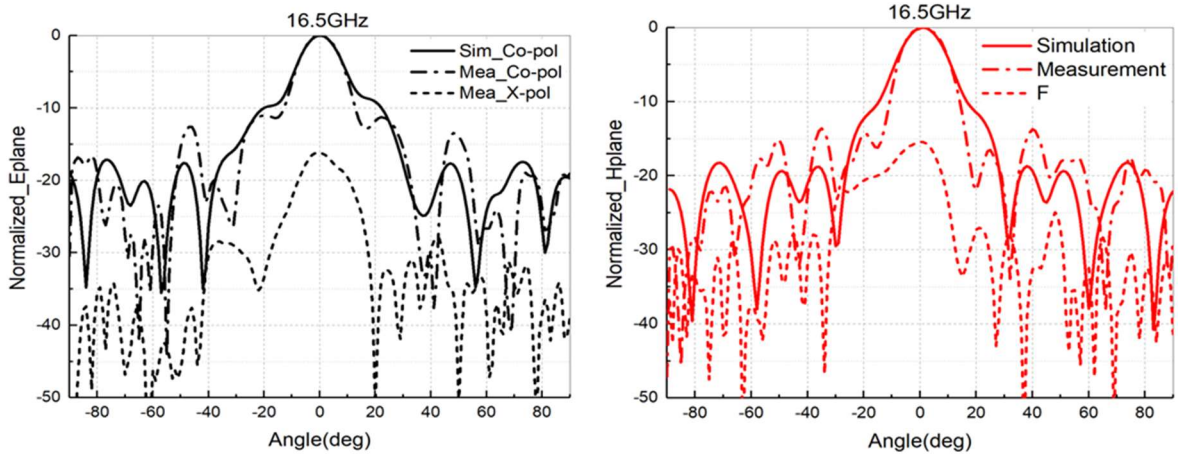
16.5GHz
Sim_Co-pol
Mea_Co-pol
Mea_X-pol
Normalized_Eplane
Angle(deg)
16.5GHz
Simulation
Measurement
F
Normalized_Hplane
Angle(deg)

(i)

Fig. 5-15 Simulated and measured E-plane and H-plane patterns of conformal TA. (a) 8.5GHz. (b) 9.5GHz. (c) 10.5GHz. (d) 11.5GHz. (e) 12.5GHz. (f) 13.5GHz. (g) 14.5GHz. (h) 15.5GHz. (i) 16.5GHz.

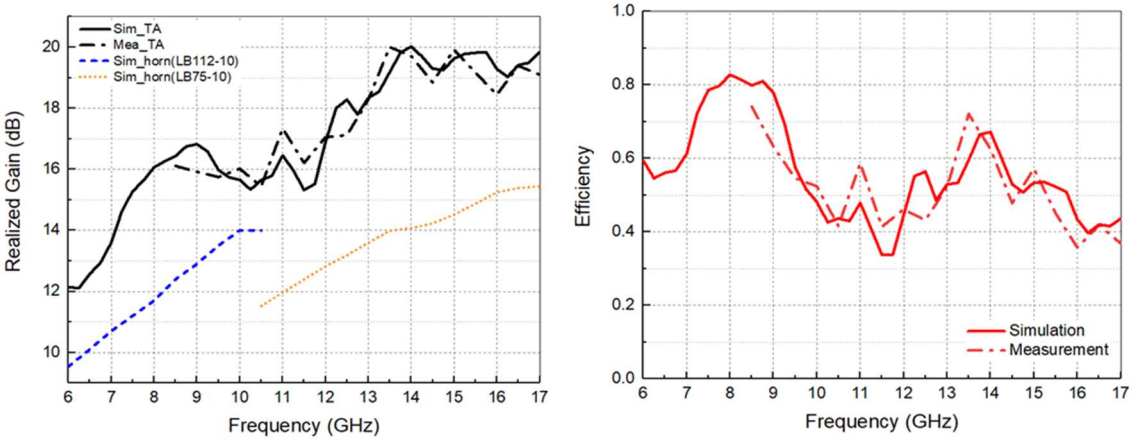


(a) (b)

Fig. 5-16 Simulated and measured results. (a) Realized gain versus frequency. (b) Aperture efficiency versus frequency.

## 5.3 Discussion

In practical applications, a wideband low-gain antenna can be applied as the feed source instead of multiple gain horns. This way, the proposed TA antenna is capable of covering a wide band with high gains. To this end, a log-periodic dipole antenna (LPDA) has been designed as the feed for a planar connected TA with the size of $4.3\lambda_{highest} \times 4.3\lambda_{highest}$ as shown in Fig. 5-17 (a) and (b). The array still consists of 19×19 elements with the same size of the original design. It should be noted that a wide range of low-gain UWB antennas can be applied as the feed source here, e.g., LPDA, spiral antennas and Vivaldi antennas, etc. We chose LPDA to verify the developed transmitarray theory as an example. The LPDA has an almost constant gain across the frequency band, thereby having a stable beamwidth. The distance between the feed and the TA aperture is 31.5 mm,

corresponding to a flare angle of ±50°, which matches the -10 dB beamwidth of the LPDA. The dimensions of the LPDA are given in Table 5-1. The simulated $|S_{11}|$ of the LPDA and the planar TA are provided in Fig. 5-18 (a), which are both lower than -10 dB. The simulated realized gains of the planar TA and LPDA are given in Fig. 5-18 (b). It is seen that the realized gain can be increased by about 2.5-10.5 dB from 6 GHz to 17 GHz. This enhancement is comparable to the work in [46].

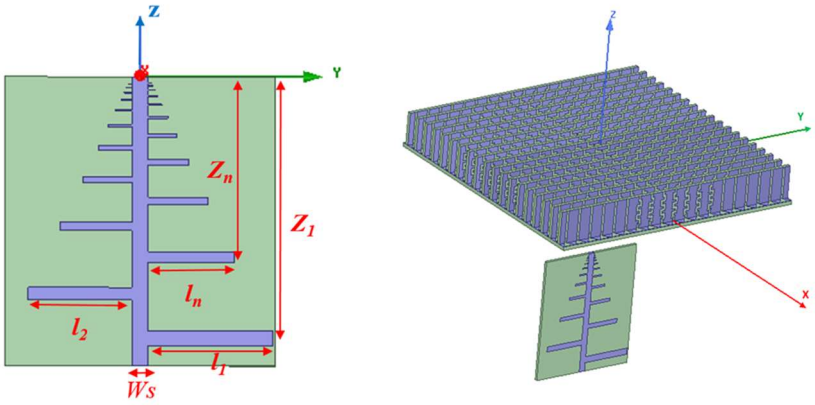


(a) (b)

Fig. 5-17 (a) Log-periodic dipole antenna (LPDA). (b) Planar TA with the LPDA as the feed source.

Table 5-1 Parameters of LPDA

| $l_1$ | $Z_1$ | $W_S$ | $\tau\ (\tau = \frac{l_{n+1}}{l_n} = \frac{Z_{n+1}}{Z_n})$ |
|---|---|---|---|
| 13.835 mm | 30mm | 1.8 mm | 0.83 |

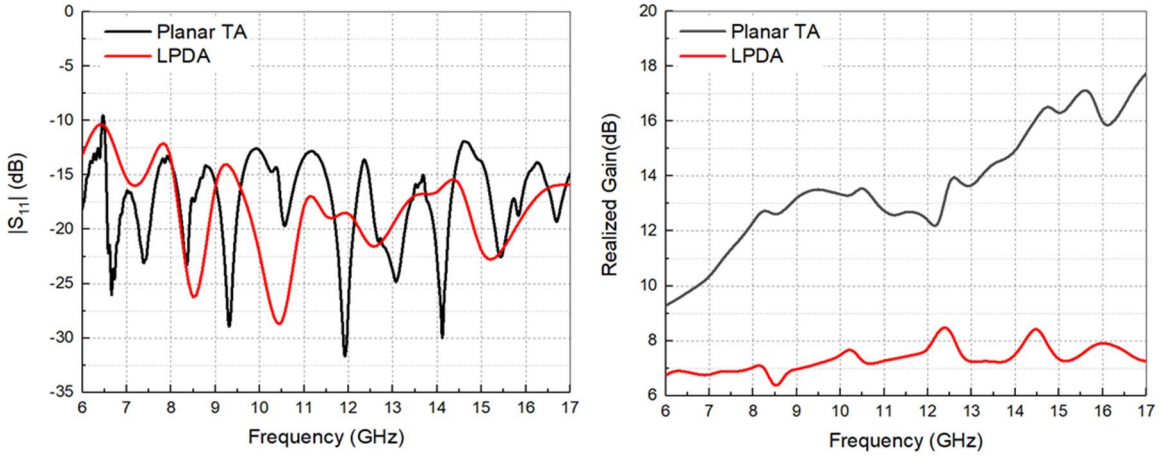


(a) (b)

Fig. 5-18 (a) Simulated $|S_{11}|$of feed LPDA and whole TA system. (b) Simulated gain of feed LPDA and whole TA system.

The LPDA is also applied to feed a conformal connected TA with 19×19 elements, as shown in Fig. 5-19. The simulated $|S_{11}|$ of the conformal TA is given in Fig. 5-20 (a), showing less than -10 dB values. The realized gains of the conformal TA are compared with LPDA gain values in Fig. 5-20 (b), providing 3-9.5 dB gain enhancement from 6 GHz to 17 GHz. For both planar and conformal structures in this section, despite the transmitarray models are the same with the previous fabricated ones in Fig. 5-8 and Fig. 5-13, the fixation for the LPDA and transmitarrays should be reconsidered. This demands refabrication and reassembly of the transmitarrays by adding fixable margins. Since the simulation and measurement results have agreed well in Section 5.1 and 5.2, only simulation results are provided here as a theoretical verification to save budget.

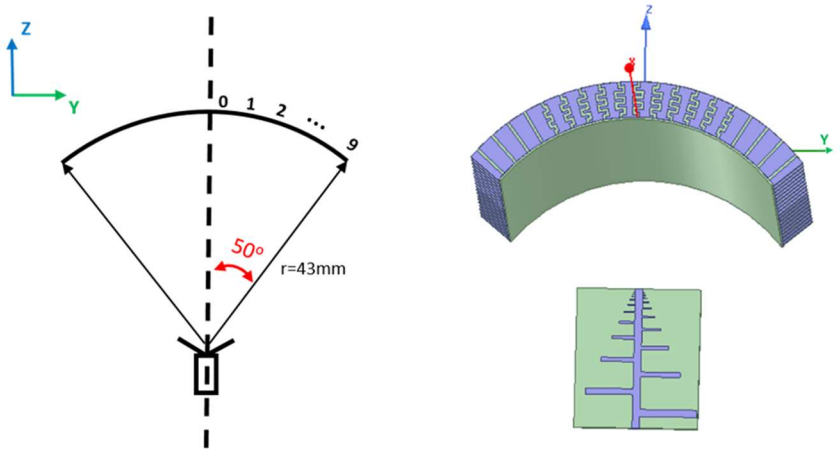


(a) (b)

Fig. 5-19 (a) Sketch of conformal TA. (b) Conformal TA with LPDA as the feed source.

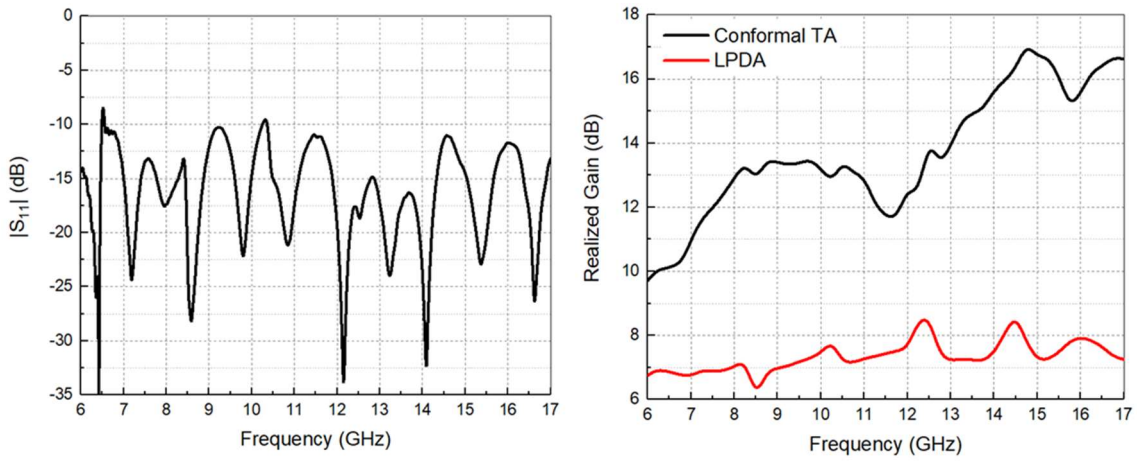


(a) (b)

Fig. 5-20 (a) Simulated $|S_{11}|$ of conformal TA. (b) Simulated gain of feed LPDA and conformal TA.

## 5.4 Conclusion

A TA element based on connected slot-bowtie is developed in this chapter for UWB operations. The element can achieve lower than 3-dB transmission losses in a frequency range from 6 GHz to 17 GHz and is capable of realizing a 360° phase tuning range. Employing this element, two UWB TAs with planar and cylindrical contours are simulated, fabricated and measured, achieving stable boresight radiation patterns across

the whole band. The simulated and measured performance agree reasonably well and the measured efficiencies are found to be much higher than state-of-the-art UWB TAs. The TAs can be employed for bandwidth hungry applications such as radio telescopes, satellite communications, and advanced radar systems.

# Chapter 6: An Elliptical Cylindrical Shaped Transmitarray for Wide-Angle Multibeam Applications

Based on the literature review in section 2.6 for state-of-the-art research progress on mm-wave multibeam TAs, it is noticeable that most of them only provide an overall beam coverage of around 60° (or ±30°), which will hinder its applications for wide angle point-to-point/multi-point-to-multi-point communications. Besides, all of those mentioned designs work at lower mm-wave bands, while a multibeam TA at above 50 GHz is still desirable for high-data-rate wireless communications. Moreover, most of the efforts have been devoted to planar TAs. The technologies for shaped multibeam TAs are still lacking. A curved cylindrical TA is demonstrated in [93], providing a simulated beam scanning range of 82° with a 3.9-dB scanning loss. In Chapter 3, the cylindrical TA achieves a mechanical beam scanning range of ±15° using a superposition method. The feed horn is rotated to illuminate different sectors at each time, thereby pointing the main beam of the array to a specific direction. Unfortunately, it cannot support multibeam radiation as its feed horn is rotated at a fixed position.

In this chapter, inspired by the 2-D wide-angle scanning metal-plate lenses introduced by Ruze [94], an elliptical cylindrical transmitting aperture is developed for the first time for multibeam applications. The phase compensation across the 3-D aperture is implemented with a combined method of refocusing the feed and utilizing a virtual focal length in calculation. Compared to the state-of-the-art planar multibeam TAs, where the multibeam

radiation performance is mainly dependent on the phase compensation on the transmitting aperture, the proposed method utilizes the shape of the aperture as an additional degree of freedom. The aperture shape and the phase compensation are jointly designed according to the desired maximum beam direction, thereby leading to a much wider beam coverage with a smaller gain loss. To validate the concept of the proposed multibeam system, a prototype is designed with a standard feed horn placed at different positions to radiate the corresponding beams. The TA realizes a measured peak boresight gain of 27 dBi at 70.5 GHz and a beam coverage up to ±43° along the elliptical arc plane with a 2.7-dB scanning loss. To the best of the authors' knowledge, this represents one of the most advanced mm-wave multibeam TAs with a large beam coverage and a low scanning loss ever reported.

The rest of this chapter is organized as follows. In section 6.1, detailed design methods for multibeam TAs are introduced. These developed methods are verified through simulations in section 6.2. In section 6.3, a multibeam TA prototype is fabricated and measured, and simulation and measurement results are compared. The chapter concludes in section 6.4.

## 6.1 Multibeam TA Design

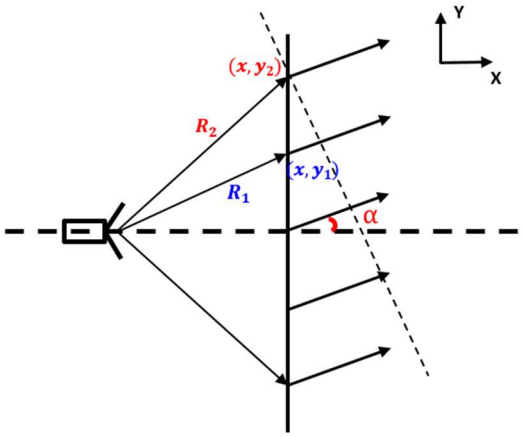


Fig. 6-1 Schematic of a TA with lateral view.

To realize a planar wave front in a desired direction for TAs, as illustrated in Fig. 6-1, the transmission phase values $\varphi(x,y)$ of two different elements ($x$, $y_1$) and ($x$, $y_2$) on the aperture can be calculated from (6-1) and (6-2), both of which are composed of a spatial phase delay and a phase compensation value $\varphi_t(x,y)$ for each element.

$$\varphi(x,y_1) = -k_0R_1 + \varphi_t(x,y_1) \tag{6-1}$$

$$\varphi(x,y_2) = -k_0R_2 + \varphi_t(x,y_2) \tag{6-2}$$

where $k_0$ is the propagation constant in free space, $R_1$ and $R_2$ are the distances of these two elements to the focus. The transmission phase difference between them is related to the beam direction $\alpha$ as follows:

$$\begin{aligned} &\Delta\varphi = (\varphi_t(x,y_1) - \varphi_t(x,y_2)) - k_0(R_1 - R_2) = \\ &\Delta\varphi_t + \Delta\varphi_{spatial} = k_0(y_2 - y_1)\sin\alpha \end{aligned} \tag{6-3}$$

One finds that two methods can be employed for scanning the beam of TAs. The first method is to integrate active components with TA elements to change the phase compensation values, i.e., changing $\Delta\varphi_t$. This is particularly useful for an electronic beam scanning. The second method is to vary the spatial phase difference $\Delta\varphi_{spati}$ by relocating the feed source relatively to the aperture. This can be employed to achieve either mechanical beam scanning or multiple beams.

In this section, based on the 2-D Ruze lens theory, we introduce an innovative method for realizing multiple beams with a wider beam coverage.

### *6.1.1 TA Contour and Phase Calculation*

The phase compensation along the TA aperture is calculated based on the predefined largest beam angles. As illustrated in Fig. 6-2, we assume that $O_1$ and $O_2$ are the focal points for two symmetrical radiation beams in *x0y* plane. These two beams are

respectively denoted as *beam1* and *beam2* at ±$\alpha$ angles, where $\alpha$ *(0<$\alpha$<90°)* is the maximum beam angle measured with respect to +*x*-axis. They are equal to the feed offset angles.

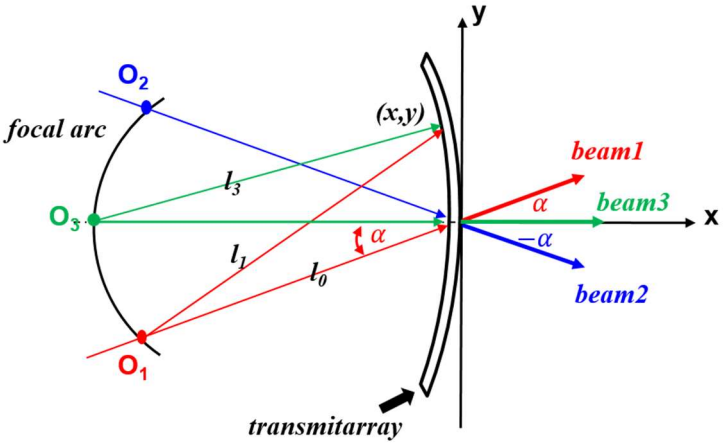


Fig. 6-2 Cross section in x0y plane of TA.

For *beam1* radiation, the element phase compensation must satisfy:

$$k_0 l_1 - \varphi_{t1}(x,y) = k_0(l_0 + x\cos\alpha + y\sin\alpha) - \varphi_{t1}(0,0) \tag{6-4}$$

where $l_1$ represents the distance between the focal point and a random element ($x$, $y$) on the aperture, and $l_0$ is the focal length of $O_1$. $\varphi_{t1}(x,y)$ is the element phase compensation value at ($x$, $y$). $\varphi_{t1}(0,0)$ is the element phase compensation at point (0, 0). We can calculate $l_1$ with:

$$l_1 = \sqrt{(x + l_0\cos\alpha)^2 + (y + l_0\sin\alpha)^2} \tag{6-5}$$

By substituting (6-5) in (6-4), and define $u$ as:

$$u = \frac{\Delta\varphi_{t1}}{k_0} = \frac{\varphi_{t1}(x,y) - \varphi_{t1}(0,0)}{k_0} \tag{6-6}$$

we can obtain:

$$(x + l_0\cos\alpha)^2 + (y + l_0\sin\alpha)^2 = (l_0 + x\cos\alpha + y\sin\alpha + u)^2 \tag{6-7}$$

After some transformations, we can get:

$$x^2\sin^2\alpha + y^2\cos^2\alpha - 2xy\sin\alpha\cos\alpha = u^2 + 2ul_0 + 2uy\sin\alpha + 2ux\cos\alpha \tag{6-8}$$

Then, considering the focal point at $O_2$ with $-\alpha$ radiation *beam2*, we can achieve:

$$x^2\sin^2\alpha + y^2\cos^2\alpha + 2xy\sin\alpha\cos\alpha = u^2 + 2ul_0 - 2uy\sin\alpha + 2ux\cos\alpha \tag{6-9}$$

Combining (6-8) and (6-9), we would obtain the phase compensation equation along the *x0y* coordinate and the ideal TA contour in (6-10) and (6-11), respectively:

$$\Delta\varphi_{t1} = k_0 u = -k_0 x\cos\alpha \tag{6-10}$$

$$(\frac{x}{l_0\cos\alpha} + 1)^2 + (\frac{y}{l_0})^2 = 1 \tag{6-11}$$

As can be seen from (6-11), along the multibeam radiation coordinate (horizontal plane), the TA shows an elliptical contour. While along *x0z* plane (vertical plane), it will show a straight contour, i.e., the proposed TA has an elliptical cylindrical shape.

### *6.1.2 Refocusing*

For a multibeam radiation with multiple feeds, initially we assume that the feed sources would be placed along the focal arc, as shown in Fig. 6-2, with a radius of $l_0$ and the pivot at (0, 0) point. As discussed in the last sub-section, the phase compensation along the TA is calculated from the maximal oblique radiation angles at $\pm\alpha$ rather than 0°. Therefore, there is a phase error for the feed source located at $O_3$ of the focal arc, which generates a beam pointing towards 0°. Here, we would discuss the phase error for 0° radiation with the feed point at $O_3$. The beam for this direction is referred to *beam3* as shown in Fig. 6-2.

With the elliptical contour of the TA aperture along *x0y* plane derived previously, we can calculate the ideal phase compensation value for *beam3* with:

$$k_0 l_3 - \varphi_{t3}(x,y) = k_0(l_0 + x) - \varphi_{t3}(0,0) \tag{6-12}$$

where $l_3$ denotes the distance from the focal point to a random point ($x$, $y$) on the aperture, and $l_0$ is the focal length of $O_3$. $\varphi_{t3}(x,y)$ is the required element phase compensation value at point ($x$, $y$). We can calculate $l_3$ with:

$$l_3 = \sqrt{(x + l_0)^2 + (y)^2} \tag{6-13}$$

Therefore, the relative phase compensation value would be:

$$\Delta\varphi_{t3} = \varphi_{t3}(x,y) - \varphi_{t3}(0,0) = k_0(\sqrt{(x + l_0)^2 + y^2} - x - l_0) \tag{6-14}$$

Then we can calculate the phase error at $O_3$ point:

$$\delta = \Delta\varphi_{t3} - \Delta\varphi_{t1} = k_0(\sqrt{(x + l_0)^2 + y^2} - (1 - \cos\alpha)x - l_0) \tag{6-15}$$

Considering the relation between $x$ and $y$ in (6-11) and employing Taylor series expansion for the variant $y$ in (6-15) at (0, 0) point, it is noticeable that the first-order and third-order derivatives are both zero, so we can approximate (6-15) with a second-order term as (6-16).

$$\delta \approx \delta_1 = k_0 \frac{\sin^2\alpha}{2l_0} y^2 \tag{6-16}$$

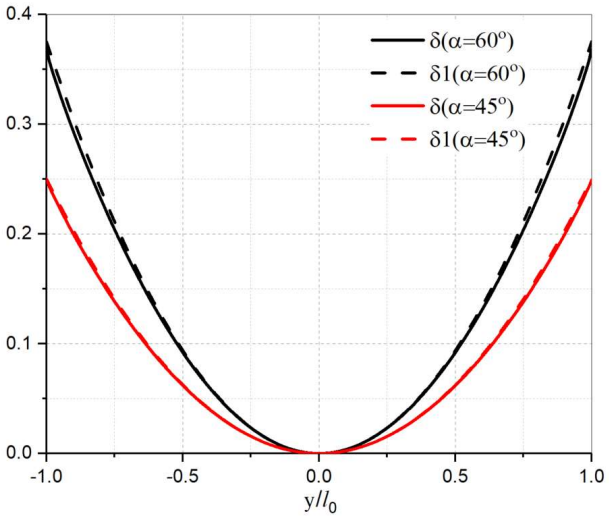


Fig. 6-3 Phase errors before and after Taylor series expansion.

Here, we consider two cases with the maximal radiation angle $\alpha$ as 60° and 45°, respectively. The curves of $\frac{\delta}{k_0 l_0}$ and $\frac{\delta_1}{k_0 l_0}$ versus $\frac{y}{l_0}$ are shown in Fig. 6-3. It is observed that there is good agreement between $\delta$ and $\delta_1$, thereby showing that the approximation given in (6-16) is acceptable.

To address the phase error at $O_3$, we moved the feed point $O_3$ away from the TA aperture by $\tau l_0$ as illustrated in Fig. 6-4. The value of the parameter $\tau$ should be chosen to eliminate the phase error. Its detailed determination process is provided as follows.

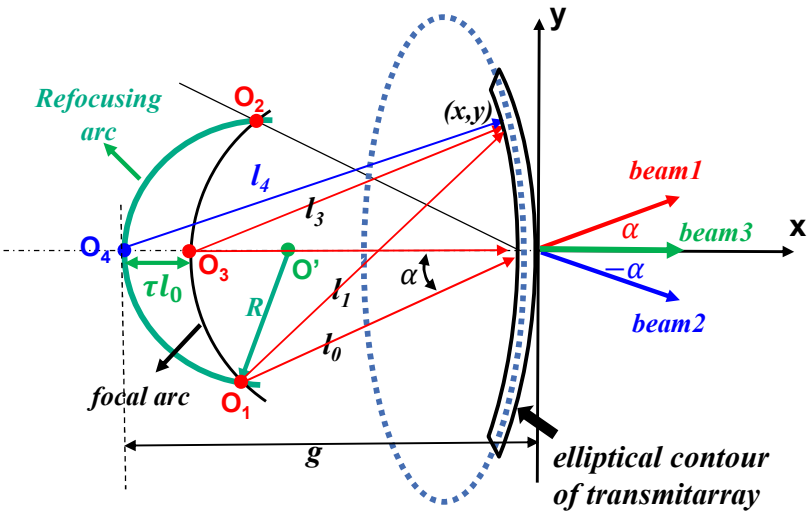


Fig. 6-4 Refocusing schematic.

The relative phase compensation value at $O_4$ can be calculated as:

$$\Delta\varphi_{t4} = \varphi_{t4}(x,y) - \varphi_{t4}(0,0) = \\ k_0(\sqrt{(x+(1+\tau)l_0)^2 + y^2} - x - (1+\tau)l_0) \tag{6-17}$$

The phase correction from the refocusing can be obtained:

$$\sigma = \Delta\varphi_{t4} - \Delta\varphi_{t3} = \\ k_0(\sqrt{(x+(1+\tau)l_0)^2 + y^2} - \sqrt{(x+l_0)^2 + y^2} - \tau l_0) \tag{6-18}$$

We can also do the Taylor series expansion for (6-18) and get:

$$\sigma \approx \sigma 1 = -k_0 \frac{\tau}{(1+\tau)2l_0} y^2 \tag{6-19}$$

Therefore, the phase aberration for boresight radiation *beam3* can be ideally fixed by refocusing the feed source from $O_3$ to $O_4$, as long as $\sigma 1 = -\delta 1$, resulting in

$$\tau = \tan^2 \alpha \tag{6-20}$$

Then we would achieve a new focal arc, marked as refocusing arc in Fig. 6-4, and the pivot moves from (0, 0) to O' (*R-g,* 0), where *g* is the new focal length at $O_4$ with a value of $(1+\tau)l_0$, and *R* can be calculated from cosine law as:

$$R = \frac{2gl_0\cos\alpha - {l_0}^2 - g^2}{2l_0\cos\alpha - 2g} \tag{6-21}$$

When the feed source is moved along the refocusing arc, the beam of the TA can be directed to different angles.

### *6.1.3 Phase Compensation along z Axis*

Since this multibeam TA shows an elliptical cylindrical contour, the phase compensation calculation is divided into two parts, i.e., along *x0y* plane (elliptical arc in horizontal plane) and along z axis (vertical straight plane). We number the elements along *x0y* and *x0z* coordinates as *i* and *j* respectively, as shown in Fig. 6-5, where multiple feed horns, numbered as -*N* to +*N*, are used in the z=0 plane. The distance between each horn and the element at (0, 0) is labelled as $d_{00}^{-N}$ to $d_{00}^{+N}$. The distance between each horn and the element along *x0z* plane is labelled as $d_{0j}^{-N}$ to $d_{0j}^{+N}$. In sub-sections 6.1.1 and 6.1.2, the phase distribution along the elliptical transmitting aperture on *x0y* plane is investigated, where feeds at different positions would radiate beams to different angles. On the other hand, along *x0z* plane, boresight beams are radiated for all the different feed sources. The phase distribution along this plane will be studied in this sub-section.

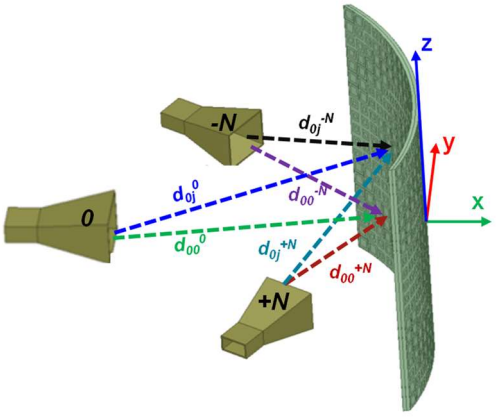


(a)

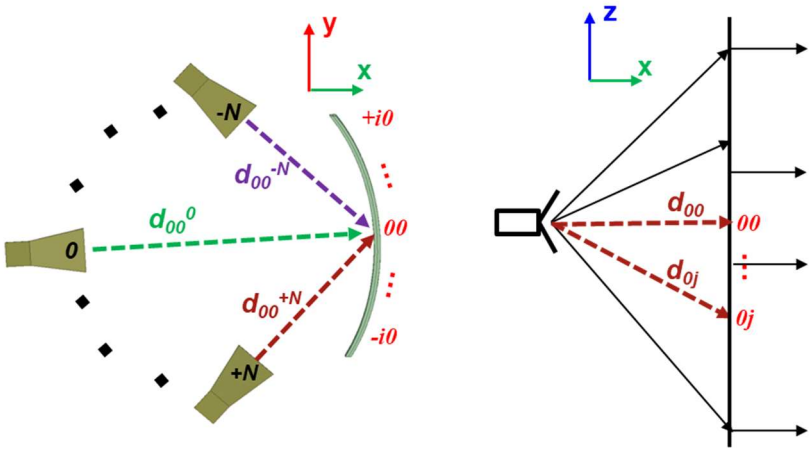


(b) (c)

Fig. 6-5 TA configuration with multiple feeds. (a) 3-D schematic. (b) Top view. (c) Front view.

For the boresight radiation on *x0z* plane, taking the *zero* column (central column along z axis) as an example, the phase compensation along z axis, as illustrated in Fig. 6-5 (c), can be calculated with (6-22), which is related to the focal length $d_{00}$.

$$\Delta\varphi_s = k_0(d_{0j} - d_{00}) \tag{6-22}$$

As shown in Fig. 6-5 (b), after refocusing, the focal length of horn *0* ($d_{00}^{0}$) is different from that of the horns -*N* ($d_{00}^{-N}$) and +N ($d_{00}^{+N}$). As a result, for each gain horn, the calculated phase distribution along z axis would be different. Therefore, a virtual value

of $d_{00}$ in (6-22) needs to be decided according to the system requirements. For example, if the goal is to maximize the gain of the boresight beam, then the $d_{00}$ needs to be close to $d_{00}^{0}$. On the other hand, if the goal is to minimize the gain difference between the boresight beam and other beams, then $d_{00}$ should be a value of about the average of $d_{00}^{0}$ and $d_{00}^{+N}$.

For other straight columns parallel with z axis, the selected $d_{i0}$ may be different from the chosen $d_{00}$ for central column. Ideally, $d_{i0}$ should be calculated for each column individually according to the system requirements as discussed above. For simplicity, the value of $d_{00}$ for the central column is used here as $d_{i0}$ for other columns.

## 6.2 Concept Verification through Simulation

### *6.2.1 Unit Cell*

In this chapter, the unit cell employed for the TA is a triple-layer structure with three identical square-ring slots printed on two substrates, as the one shown in Fig. 3-1 in sub-section 3.1.1. The substrate has a dielectric constant $\varepsilon_r$=2.2 and loss tangent of 0.0009. Since the TA has an elliptical cylindrical contour, the easiest and most cost-effective way is to bend a planar aperture onto a 3-D printed frame. This method has been validated in the conformal TAs from Chapter 3 to Chapter 5. As analysed in Chapter 3, there is always a trade-off between the element thickness and the phase range. Therefore, in this work, the overall thickness $h$ is chosen as 0.508 mm ($0.12\lambda_0$ at 72 GHz). The element periodicity is $P$=2 mm, and the optimized slot width is $w$=0.3 mm. By simulating the element with the master-slave boundary and Floquet ports in ANSYS HFSS, its amplitude and phase performance versus $L$ are achieved for a normal incidence wave, as plotted in Fig. 6-6. A 340° phase variation range is realized with a maximum 3-dB transmission loss by tuning

slot length $L$ from 1.2 mm to 1.88 mm at 72 GHz. For oblique incidence waves, the performance is found to be acceptable previously. It is not repeated in this chapter.

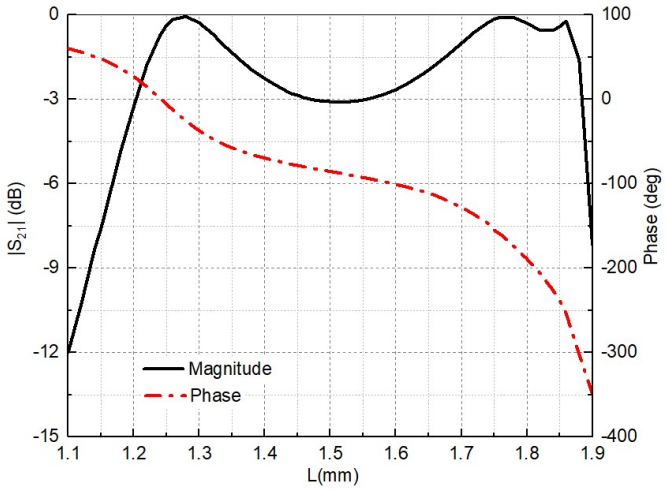


Fig. 6-6 Simulated element performance at 72 GHz.

### *6.2.2 TA Contour and Refocusing for Boresight Radiation*

A multibeam TA with an elliptical cylindrical shape is designed with maximal beam radiation angles of ±45°, and the focal length $l_0$ is chosen to be 30 mm at $O_1$ and $O_2$. The focal length is chosen by considering the aperture size and the radiation properties of the feed gain horn. Then, the contour along *x0y* plane can be obtained from (6-11) as:

$$(\frac{x}{15\sqrt{2}}+1)^2+(\frac{y}{30})^2=1 \tag{6-23}$$

The phase compensation along this contour is:

$$\Delta\varphi_e=-\frac{2\pi}{\lambda_0}\cdot\frac{\sqrt{2}}{2}x \tag{6-24}$$

To precisely arrange elements on this TA aperture and calculate the phase compensation value for each element, we need to make the elliptical arc length as the integral multiples of the element periodicity $P$ and to specify the element positions along the arc. If the $x$ and $y$ in (6-23) are expressed as:

$$\begin{cases} x = 15\sqrt{2}(\cos\varphi - 1) \\ y = 30\sin\varphi \end{cases} \tag{6-25}$$

then we can connect the element position information to the related arc length:

$$l = \int_0^{\varphi} \sqrt{(15\sqrt{2})^2 \sin^2\phi + (30)^2 \cos^2\phi} d\phi \tag{6-26}$$

For example, for the *i-th* element with the arc length $l=iP$ along the *x0y* plane, the related phase compensation value $\Delta\varphi_e$ can be achieved by combining (6-24)-(6-26).

To eliminate the phase error for the radiation at boresight, a refocusing method is adopted as illustrated in Fig. 6-4. In this design, the feed position $O_4$ can be obtained from (6-20) as $\tau$=1, resulting in $g=2l_0$=60 mm. For multibeam realizations, multiple feed horns need to be arranged along the refocusing arc as marked in Fig. 6-4.

### *6.2.3 Phase Distribution on Multibeam TA*

As mentioned before, the calculation of the phase distribution for the whole structure is divided into two parts. For the elliptical arc on the horizontal *x0y* plane, (6-24) is used for the phase calculation. To achieve the phase compensation along the vertical straight plane, as introduced in the sub-section 6.1.3, a virtual focal length $d_{00}$ needs to be decided for desired radiation performance. In this design, an elliptical cylindrical TA with 25×23=575 cells is constructed using the element model demonstrated in sub-section 6.2.1 at 72 GHz. A standard gain horn LB-12-15-A from A-INFO is placed at each focal point as the feed source, which operates from 60 GHz to 90 GHz. Its gain is 15.35 dBi at 72 GHz as noted from the datasheet. The size of the TA aperture cross section is 46.4 mm×46 mm. The size of the aperture projection on *y0z* plane is 46.4 mm×46 mm=11.1$\lambda_0$×11$\lambda_0$ (at 72 GHz), which is used to calculate the aperture efficiency. These dimensions were chosen to make the aperture edge illumination about -10 dB when the horn is located at feed points $O_1$ and $O_2$.

The feed positions for the boresight radiation and -45° radiation are ($x$, $y$) = (-60 mm, 0 mm) and (-21.2 mm, 21.2 mm), respectively. In this case, $d_{00}^{0}$=60 mm and $d_{00}^{-N}$ =30 mm. As illustrated in the sub-section 6.1.3, to balance the radiation performance at 0° and ±45°, a virtual focal length $d_{00}$=36 mm is chosen to calculate the phase compensation along z axis with (6-22). This virtual focal length is chosen by optimizing the scanning loss between 0° and ±45° with a target of less than 3 dB. After combining the vertical phase compensation with the elliptical one given in (6-24), the whole TA configuration is determined.

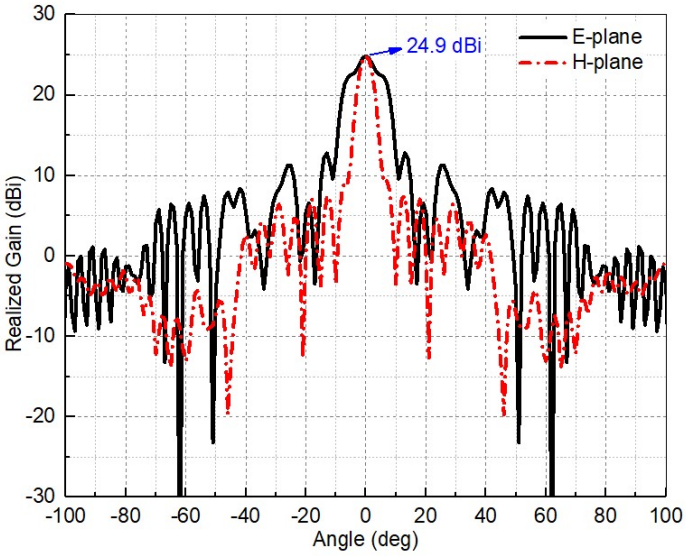


Fig. 6-7 Boresight radiation patterns with $d_{00}^{0}$=60 mm.

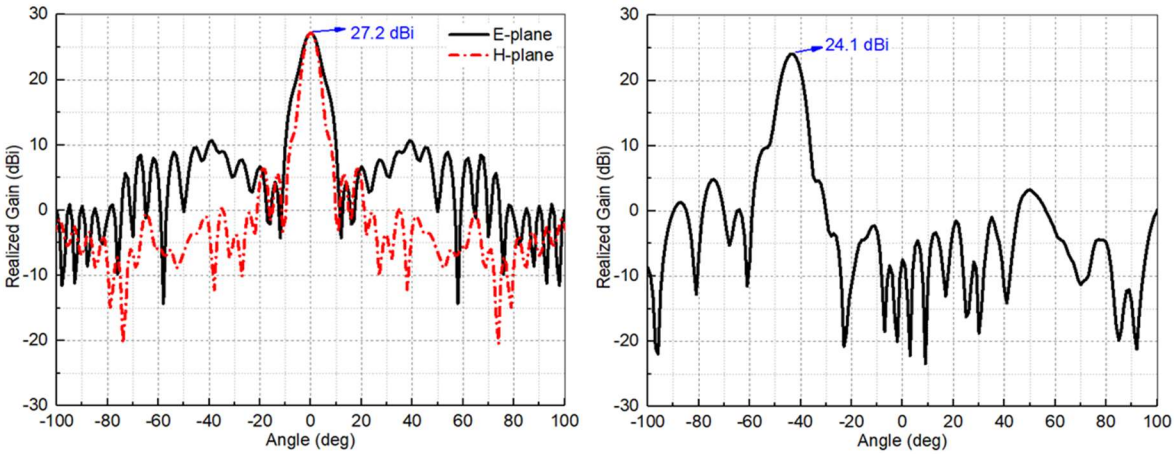


(a) (b)

Fig. 6-8 (a) Boresight radiation patterns with $d_{00}^{0}$=48 mm. (b) -45° radiation pattern.

Then, we simulated the antenna's boresight radiation patterns in *x0y* (H-plane) and *x0z* (E-plane) planes as given in Fig. 6-7. It can be noticed that the 3-dB beamwidth in E-plane is wider than that of the H-plane. This is because the chosen virtual focal length $d_{00}$ for calculating the phase compensation in vertical plane deviates a lot from the actual focal length for 0° radiation in the elliptical horizontal plane ($d_{00}^{0}$=60 mm). Therefore, the refocusing position (-*g*, 0) for horn *0*, i.e., the gain horn for boresight radiation, needs to be optimized to balance the E-plane and H-plane radiation performance. By optimizing *g* (g=$d_{00}^{0}$) to 48 mm, which means moving the gain horn of the boresight beam towards the aperture, the radiation pattern along E-plane is improved as shown in Fig. 6-8 (a), making the peak gain increase from 24.9 dBi to 27.2 dBi. The gain horn positions are unchanged for ±45° beam directions. The radiation pattern at -45° is given in Fig. 6-8 (b). In this case, the final refocusing position for horn *0* is decided as *(-g*, 0) = (-48 mm, 0), which is referred as $O_4$' in Fig. 6-9.

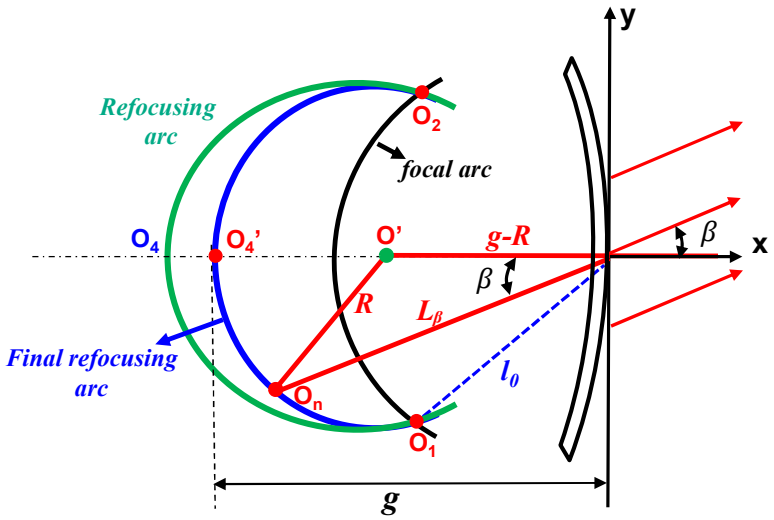


Fig. 6-9 Schematic for feed position calculation.

### *6.2.4 Feed System for Multibeam Realization*

Finally, the refocusing arc is developed from three feed positions of $O_1$, $O_2$ and $O_4$'. The next step is to specify the feed position for each desired beam. As illustrated in Fig. 6-9, for the beam radiation to a random angle $\beta$, the related feed $O_n$ shows the same offset angle as $\beta$, and its focal length is denoted as $L_\beta$. With $g$=48 mm, $l_0$=30 mm, and designed maximal radiation angle $\alpha$=45°, we can calculate the radius of the refocusing arc from (6-21), as $R$=21.8 mm. Then the focal length $L_\beta$ can be derived from law of cosines with $R$, $g$-$R$ and $\beta$. The feed position can be expressed with ($-L_\beta \cos\beta$, $-L_\beta \sin\beta$).

As a demonstration here, radiation beams at 0°, ±10°, ±20°, ±30°, ±40°, ±45° are given, and the corresponding feed positions are listed in Table 6-1 (only positive angles are shown due to structure symmetry).

Table 6-1 Feed positions for different beam radiations

| **Radiation angle ($\beta$)** | **$L_\beta$/mm** | **$O_n$ ($x_n$, $y_n$)/(mm, mm)** |
|---|---|---|
| 0° | 48 | (-48, 0) |
| 10° | 47.12 | (-46.4, -8.2) |
| 20° | 44.49 | (-41.8, -15.2) |
| 30° | 40.11 | (-34.7, -20) |
| 40° | 33.91 | (-26, -21.8) |
| 45° | 30 | (-21.2, -21.2) |

By shifting the feed horn to different positions according to Table 6-1, multiple beams are achieved at 72 GHz, as shown in Fig. 6-10. Peak realized gain values at different angles are listed in Table 6-2. It is noticed that the beam can be scanned to ±43° with an only 3.1-dB drop from the maximum realized gain. The side lobe levels are lower than -15 dB for all the beams. As can be seen from Table 6-2, for some large beam radiation angles, there is a 1° or 2° difference between the 3-D simulated angles and the predefined ones. This can be attributed to the phase errors due to the virtual focal length. As discussed

in sub-section 6.1.3, we introduce a virtual focal length when calculating the phase compensation along the vertical planes. This virtual focal length is different from the actual focal length for achieving the oblique beams. This could bring some phase errors for large-angle beams.

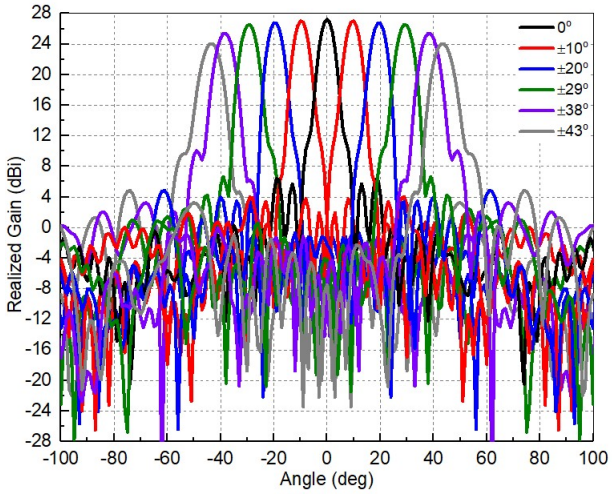


Fig. 6-10 Simulated multibeam patterns at 72 GHz.

Table 6-2 simulated peak realized gains at different angles

| Radiation angle | 0° | ±10° | ±20° | ±29° | ±38° | ±43° |
|---|---|---|---|---|---|---|
| Peak gain (dBi) | 27.2 | 27 | 26.7 | 26.6 | 25.4 | 24.1 |

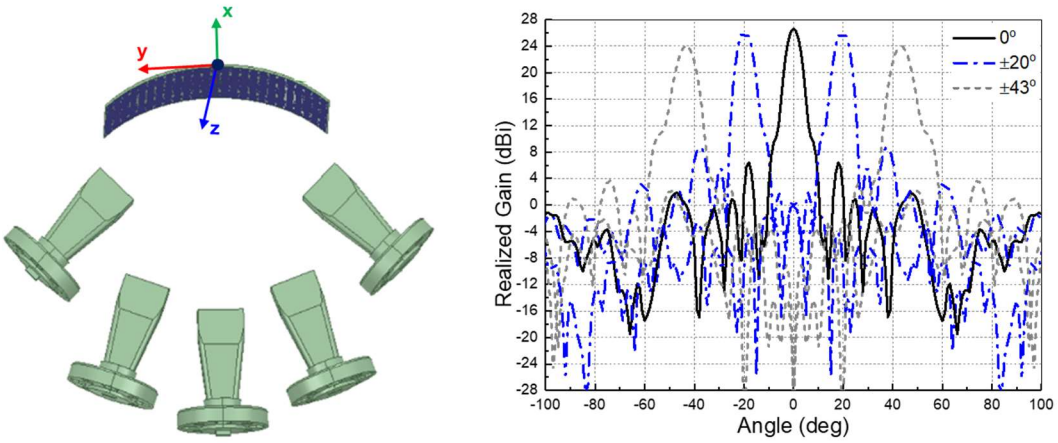


(a) (b)

Fig. 6-11 (a) The multibeam TA with 5 feed horns for 0°, ±20° and ±43°. (b) Simulated radiation patterns with 5 feed horns.

In practice, multiple feeds can be utilised to generate multiple beams, as shown in Fig. 6-11 (a). The model consists of five feed horns for radiations at 0°, ±20° and ±43°, respectively. The simulated radiation patterns are given in Fig. 6-11 (b). They are almost the same as the results when a single sliding horn is used as in Fig. 6-10. Due to the size of the available gain horn in our lab, the angular step of the multiple beams cannot be very small. This could be resolved by using smaller feed horns/waveguides or designing appropriate microstrip antenna arrays as feed sources.

### *6.2.5 Design Procedure*

According to the theoretical analysis and the prototype simulations discussed in the last few sub-sections, we can summarize the whole design procedure as follows:

Step 1: Choose a proper focal length $l_0$ and the desired maximal radiation angles $\pm\alpha$;

Step 2: By following (6-10) and (6-11), the elliptical contour formula of TA can be derived, and the specific phase compensation values along it can be obtained;

Step 3: Adopt a refocusing design based on (6-20) to find the feed horn position for boresight radiation and reduce the phase errors of multiple beams on the horizontal plane;

Step 4: Choose the value of $d_{00}$ as the virtual focal length for phase compensation along the vertical straight plane, aiming to balance the radiation performance at 0° and the maximum radiation angles;

Step 5: Combine phase compensation along the horizontal and vertical planes to decide the conformal TA configuration;

Step 6: Optimize the refocusing position for the boresight radiation to obtain the best 0° radiation pattern;

Step 7: Draw the final refocusing arc with three known feed positions, and locate different feed horns along this arc to realize multibeam radiations between $-\alpha$ and $\alpha$.

## 6.3 Prototype Fabrication and Measurement

To verify the developed transmitting aperture for multibeam radiations, an antenna prototype is fabricated and measured. The transmitting aperture consists of two substrate layers with a thickness of 0.254 mm for each one. The unfolded transmitting surface is fabricated using a standard PCB technology. Then the two surfaces are laminated together and attached to a 3-D printed cylindrical frame. Photographs of the TA prototype with a 3-D printed fixture are shown in Fig. 6-12. As seen from Fig. 6-12 (b), P1 and P2 are two screws to connect the focal arm to the array fixture and horn fixture, respectively. P1 point can be rotated to find different feed positions along the refocusing arc, and P2 point can be rotated to keep the feed horn pointing to the TA centre. Considering the overall cost and available measurement conditions, one feed horn is moved along the refocusing arc for different beams.

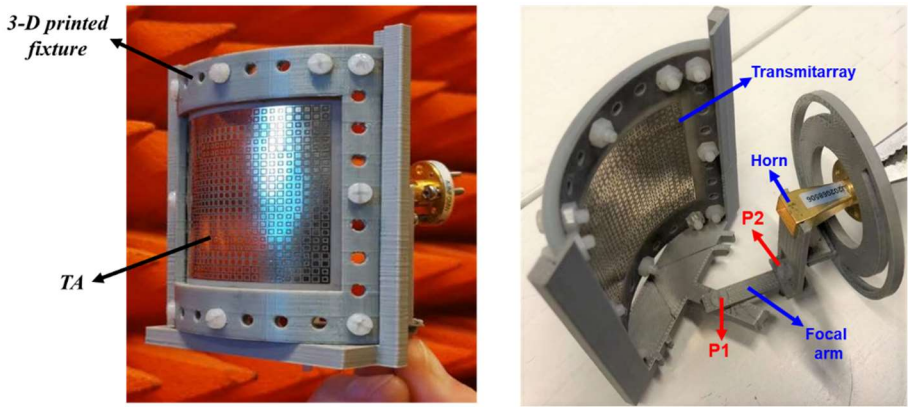


(a) (b)

Fig. 6-12 Photographs of fabricated prototype. (a) Front view. (b) Side view.

Since the TA is a single-port device, the reflection coefficient is measured by connecting the feed horn to one port of the vector network analyzer (VNA). The S-parameter of the TA is measured using a Keysight VNA N5225A with one 60-90 GHz VNA extender. Simulated and measured S-parameters for the boresight radiation are compared in Fig.

6-13 (a). Reasonably good agreement can be found with both curves lower than -10 dB from 60 GHz to 85 GHz. The measured S-parameters for other oblique beams are given in Fig. 6-13 (b), showing that all of them are below -20 dB from 60 GHz to 85 GHz. Due to the structural symmetry, only results for positive angles are plotted for the sake of clarity. Far-field radiation patterns are measured using a Microwave Vision Group (MVG) compact range antenna measurement system located at University of Technology Sydney, Australia. For the boresight radiation, the simulated and measured realized peak gains versus frequency are compared in Fig. 6-14 (a). It can be noticed that the operating frequency shifts to a lower band. The simulated peak realized gain occurs at 72 GHz while the measured one is at 70.5 GHz, which corresponds to a shift of 2%. This frequency shift is attributed to multiple reasons, including the phase errors resulting from the fabrication and alignment inaccuracies. Furthermore, a thin PVC layer is employed to laminate the two substrate layers together, which may bring some deviations from the ideal element model in the simulation. The measured 3-dB gain bandwidth is 12.3% from 65.7 GHz to 74.3 GHz, with a maximal value of 27 dBi at 70.5 GHz. The simulated and measured patterns for the boresight radiation at 70.5 GHz along E-plane and H-plane are compared in Fig. 6-14 (b) with good agreement.

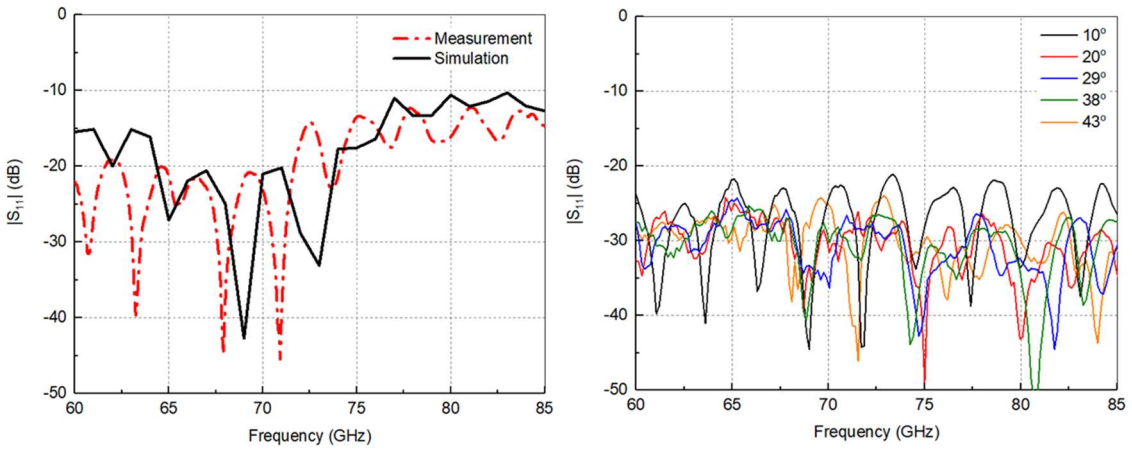


(a) (b)

Fig. 6-13 Results from simulation and measurement. (a) S-parameter for boresight radiation. (b) Measured S-parameter at different radiation angles.

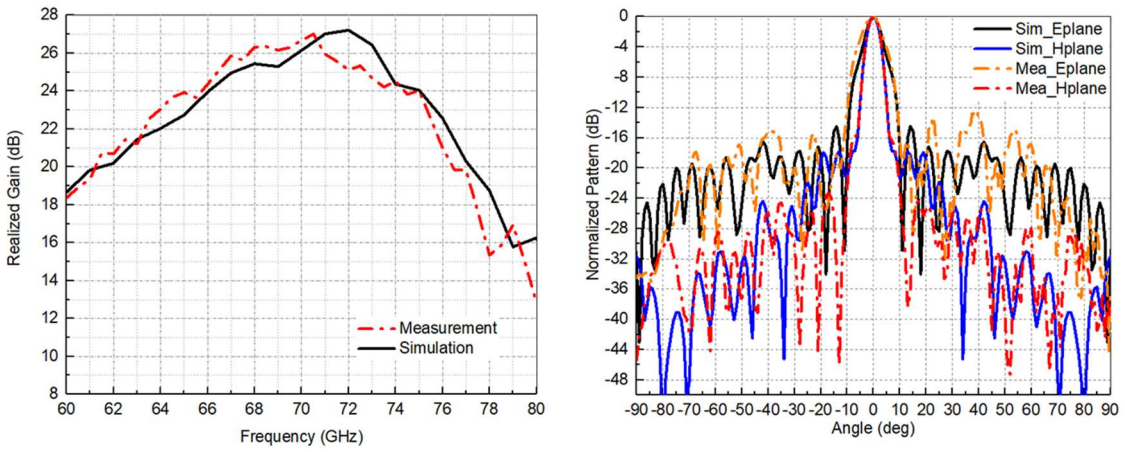


(a) (b)

Fig. 6-14 (a) Realized gain versus frequency for boresight radiation. (b) Boresight radiation patterns at 70.5 GHz.

Table 6-3 Measured results of different scanning angles at 70.5 GHz

| Beam angle | 0° | -10°/+10° | -20°/+20° | -29°/+29° | -38°/+38° | -43°/+43° |
|---|---|---|---|---|---|---|
| Gain (dBi) | 27 | 26/26.1 | 26.2/26.2 | 26.2/25.9 | 25.1/25.4 | 24.3/24.3 |
| SLL (dB) | -23 | -19/-17 | -17/-16 | -19/-16 | -16/-14 | -14/-14 |

The measured multibeam radiation performance at 66 GHz, 68 GHz, 70.5 GHz, 72 GHz and 74 GHz are plotted in Fig. 6-15 (a)-(e), respectively. The realized gains at 70.5 GHz for 0° and ±43° are 27 dBi and 24.3 dBi, respectively. The peak gain values and sidelobe levels (SLL) for each beam angle at 70.5 GHz are listed in Table 6-3. The maximum aperture efficiency is 34% for the boresight radiation. For other frequencies, the scanning loss is between 2.3 dB and 2.7 dB. Besides, from Fig. 6-15 (f), it is noticeable that the measured cross-polarization levels at 70.5 GHz for different radiation angles are all lower than -20 dB with respect to the co-polarization level. Similar values are obtained for other frequency points which are not shown here for brevity.

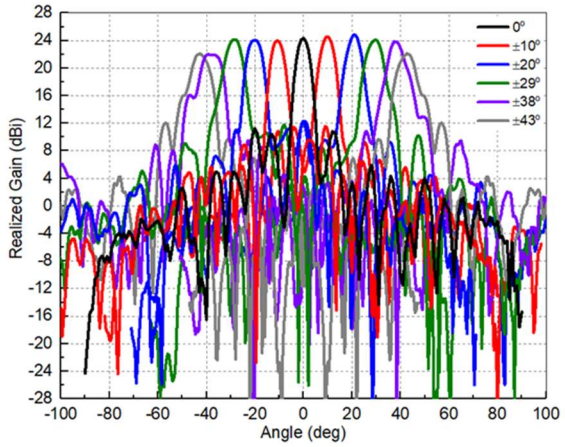


(a)

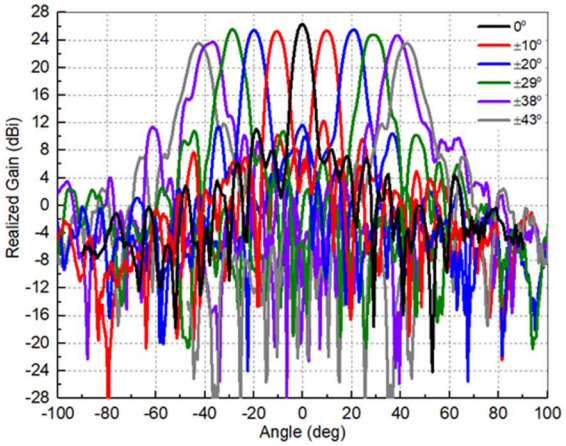


(b)

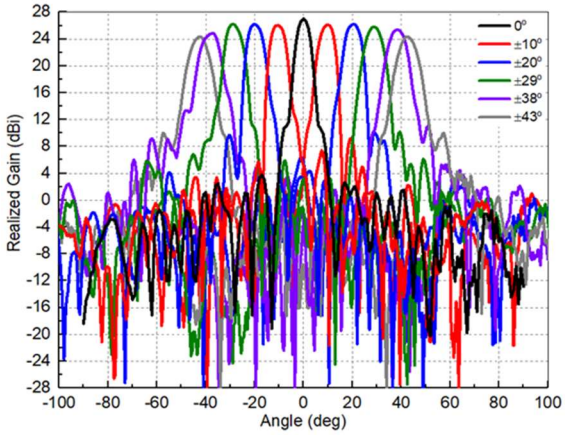


(c)

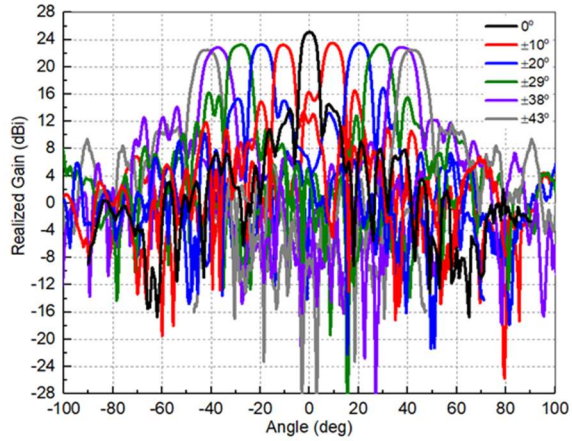


(d)

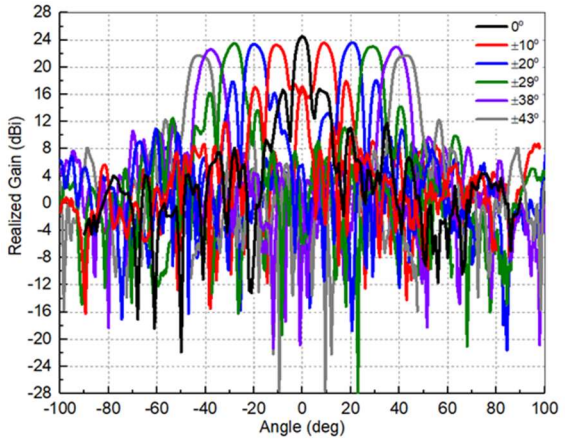


(e)

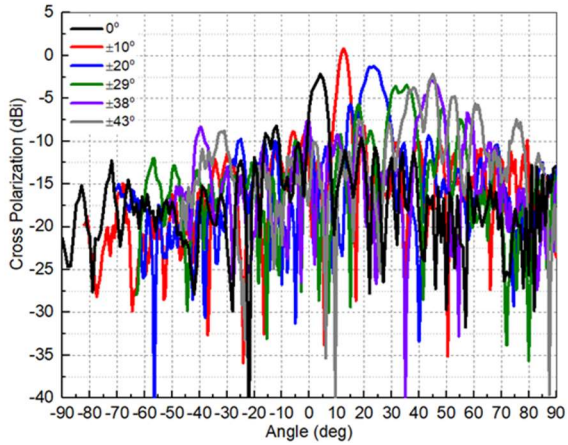


(f)

Fig. 6-15 Measured multibeam radiation patterns. (a) 66 GHz. (b) 68 GHz. (c) 70.5 GHz. (d) 72 GHz. (e) 74 GHz. (f) Cross polarization at 70.5 GHz.

Table 6-4 shows the performance comparison between the proposed TA and other reported designs. Regarding the beam coverage, even though a wide range of 82° is achieved in [93], the aperture efficiency is low and the scanning loss is large. The designs from [65] and Chapter 3 provide very low scanning losses, but the scanning ranges are limited. It is noticeable that our array has a greater beam scanning range and a small scanning loss without sacrificing the aperture efficiency.

Table 6-4 Performance comparison with other designs

| **Ref. No.** | **Frequency** | **Maximal beam coverage** | **Peak gain /dBi** | **Aperture efficiency** | **Scanning loss /dB** |
|---|---|---|---|---|---|
| [65] | 26 GHz | 66° (-33°~ +33°) | 22.2 | 35.7% | 1.2 |
| [66] | 28.5 GHz | 60° (-30°~ +30°) | 25 | 32.3% | 3.5 |
| [67] | 28 GHz | 54° (-27°~ +27°) | 24.2 | 24.5% | 3.7 |
| [69] | 30 GHz | 50° (0°~ +50°) | 27.3 | 15.1% | 2.8 |
| [70] | 20/30 GHz | 50° (0°~ +50°) | 24.7/27.2 | 37.3%/29.5% | 4.4/3.7 |
| [93] | 30 GHz | 82° (-4°~ +78°), *simulated results* | 28.9 | 20% | 3.9 |
| Chapter 3 | 25 GHz | 30° (-15°~ +15°) | 18.7 | 25.1% | 0.8 |
| **This work** | 70.5 GHz | 86° (-43°~ +43°) | 27 | 34% | 2.7 |

## 6.4 Conclusion

An elliptical cylindrical transmitting aperture is developed for multibeam TAs. The phase compensation and the shape of the array are jointly designed to enlarge the beam coverage. A refocusing analysis is introduced to reduce phase errors of multiple beams on the horizontal plane. Besides, a virtual focal length is adopted to calculate the phase values on the vertical plane. As a validation, a multibeam prototype at 72 GHz is designed, fabricated and measured, showing good agreement between simulation and measurement. The radiation angles can cover from -43° to 43° with a 2.7-dB scanning loss. The developed multibeam TAs are expected to find wide applications in 5G wireless systems and beyond.

# Chapter 7: Conclusions and Future Work

## 7.1 Conclusions

This dissertation presents several advanced conformal TAs with unique features in order to facilitate 5G and beyond wireless communications. In Chapter 2, the basic concept of TAs is introduced, and different element synthesis techniques are explained with examples. Besides, based on different communication system requirements, a comprehensive literature review regarding multiple research areas of TAs is conducted, including low profile, beam scanning, high efficiency, wide operating band, multibeam radiation and conformal applications. It is noteworthy that very few research work has been reported on the development of conformal TAs. To fill this research gap, several innovative methodologies are proposed and verified experimentally for conformal TA designs with high-efficiency, ultra-wide band, beam steering and multi-beam radiation properties, respectively. All of these designs are summarized below.

In Chapter 3, a novel conformal TA with a beam-steering capability is presented. A thin TA element consisting of three layers of identical square slots is designed with an overall thickness of 0.508 mm at 25.5 GHz. It is applied to a cylindrical conformal transmitting surface, achieving a fixed boresight radiation beam with a peak measured gain of 19.6 dBi and an aperture efficiency of 25.1%. Furthermore, the transmitting surface of the fixed-beam array is divided into two parts with individually calculated phase distributions, so that the combined beam can be switched to different oblique angles. A prototype of the beam-steering TA is fabricated and measured, with the main beam scanned to ±15°, ±10°, ±5° and 0°, and a stable gain value of about 18.7 dBi at all beam angles is achieved.

In Chapter 4, a dual-layer ultra-thin conformal TA with a high efficiency is developed based on Huygens metasurface theory. The proposed element consists of two metal layers printed on single substrate with an only 0.5-mm thickness ($\lambda_0$/60 at 10 GHz). Electric and magnetic responses are analysed and manipulated together for desired transmission phases, producing eight elements to cover a quantized 360º phase range with a maximal 1.67-dB loss. Also, the oblique incidence cases are considered on each element to enhance the aperture efficiency further. The final cylindrical conformal TA achieves a measured gain of 20.6 dBi with a 47.4% aperture efficiency.

In Chapter 5, an innovative technique is introduced for both UWB planar and conformal TAs resorting to connected-array and true-time-delay-line theories. In particular, the elements are composed of a horizontally connected slot-bowtie and vertical meander slot-lines, capable of a 360° phase variation at the highest frequency of 17 GHz with transmission losses less than 3 dB from 6 GHz to 17 GHz. The TA has been designed, fabricated and measured with both planar and cylindrical shapes. Both of them can provide stable boresight radiation patterns from 6 GHz to 17 GHz with increasing peak gains as frequency.

In Chapter 6, a mm-wave TA with an elliptical cylindrical shape is developed for wide-angle multibeam radiations. Multiple feeds can be placed on the middle horizontal plane to radiate multiple beams. The antenna shape and phase compensation are jointly designed according to desired maximal beam directions. Innovative methods including a feed refocusing analysis and a virtual focal length are utilized to determine the phase distribution across the transmitting surface for multiple beams with a small scanning loss. By changing the feed horn position along the final refocusing arc, the main beam of the fabricated prototype is scanned to eleven directions between ±43° with a 2.7-dB scanning loss at 70.5 GHz.

## 7.2 Future Work

Owing to their aerodynamic performance, it is expected that conformal TAs will find a wide range of applications to airborne, space borne and satellite networks, such as UAVs, high-altitude platforms (HAPs), and aircrafts, especially in the context of 5G and beyond networks. To date, research in conformal TAs is still in its infancy. Consequently, the technologies presented in this thesis are meant to inspire more innovations as shown below in this field.

1. The presented beam-scanning and multibeam radiation methods can serve point-to-point/multi-point-to-multi-point communication links. For broadcasting purpose, we need to deliver the same information to several distributed users simultaneously. For this scenario, single-feed multibeam or shaped beam conformal TAs are needed.
2. The profile of the transmitting surface of the developed conformal TAs has been reduced significantly for practical implementations in this dissertation. Another potential research challenge is to reduce the overall profile of the TA systems with feed sources, e.g., develop folded conformal TAs with reduced focal lengths.
3. The developed conformal TAs work mainly at microwave bands or mm-wave bands. For the future sixth generation (6G) wireless networks and space communications, advanced terahertz (THz) conformal TAs with beam-scanning or multibeam capabilities are highly demanded, which can lead to new challenges and opportunities.

# Bibliography


[1] Q. Luo, S. Gao, W. Liu, C. Gu, "Low-cost smart antennas," *John Wiley & sons*, March 2019.

[2] S. Gaber, S. H. Zainud-Deen and H. A. E. Malhat, "Analysis and design of reflectarrays/transmitarrays antennas," *LAP LAMBERT Academic Publ,* 2014.

[3] L. Dussopt, "Transmitarray antennas," in A. Boriskin and R. Sauleau (eds), Aperture Antennas for millimeter and sub-millimeter wave applications, Springer 2018.

[4] A. H. Abdelrahman, A. Z. Elsherbeni, and F. Yang, "High-gain and broadband transmitarray antenna using triple-layer spiral dipole elements," *IEEE Antennas Wireless Propag. Lett.*, vol. 13, pp. 1288–1291, 2014.

[5] P.-Y. Feng, S.-W. Qu, and S. Yang, "Octave bandwidth transmitarrays with a flat gain," *IEEE Trans. Antennas Propag.*, vol. 66, no. 10, pp. 5231–5238, Oct. 2018.

[6] Q. Luo, S. Gao, M. Sobhy, and X. Yang, "Wideband transmitarray with reduced profile," *IEEE Antennas Wireless Propag. Lett.*, vol. 17, no. 3, pp. 450–453, Mar. 2018.

[7] M. Beccaria, P. Pirinoli, F. Yang, "Preliminary results on conformal transmitarray antennas," In *2018 IEEE International Symposium on Antennas and Propagation & USNC/URSI National Radio Science Meeting*, pp. 265-266, IEEE, 2018.

[8] T. A. Hill, J. R. Kelly, M. Khalily, T. W. C. Brown, "Conformal transmitarray for scan loss mitigation with thinned reconfiguration," In *13th European Conference on Antennas and Propagation (EuCAP),* pp. 1-5, IEEE. 2019.

[9] S. V. Hum and J. Perruisseau-Carrier, "Reconfigurable reflectarrays and array lenses for dynamic antenna beam control: A review," *IEEE Trans. Antennas Propag.*, vol. 62, no. 1, pp. 183–198, Jan. 2014.

[10] C. Huang, W. Pan, and X. Luo, “Low-loss circularly polarized transmitarray for beam steering application,” *IEEE Trans. Antennas Propag.*, vol. 64, no. 10, pp. 4471–4476, Oct. 2016.

[11] J. G. Nicholls and S. V. Hum, “Full-space electronic beam-steering transmitarray with integrated leaky-wave feed,” *IEEE Trans. Antennas Propag.*, vol. 64, no. 8, pp. 3410–3422, Aug. 2016.

[12] C. Tian, Y.-C. Jiao, and G. Zhao, “Circularly polarized transmitarray antenna using low-profile dual-linearly polarized elements,” *IEEE Antennas Wireless Propag. Lett.,* vol. 16, pp. 465–468, 2017.

[13] Q. Luo, Steven Gao, M. Sobhy, X.Yang, Z.-Q. Cheng, Y.-L. Geng, J. T. S. Sumantyo, “A hybrid design method for thin panel transmitarray antennas,” *IEEE Trans. Antennas Propag.,* vol. 67, no. 10, pp. 6473-6483, Oct. 2019.

[14] P.-Y. Qin, L.-Z. Song, and Y. Jay Guo, “Beam steering conformal transmitarray employing ultra-thin triple-layer slot elements,” *IEEE Trans. Antennas Propag.,* vol. 67, no. 8, pp. 5390-5398, Aug. 2019.

[15] W. Hong et al. “Multibeam antenna technologies for 5G wireless communications,” *IEEE Trans. Antennas Propag.,* vol. 65, no. 12, pp. 6231–6249, Dec. 2017.

[16] B. Panzner, A. Joestingmeier, and A. Omar, “Ka-band dielectric lens antenna for resolution enhancement of a GPR,” in *Proc. Int. Symp. On Antennas, Propagation and EM Theory*, Kunming, China, pp. 31-34, Nov. 2–5, 2008.

[17] Z. X. Wang and W. B. Dou, “Dielectric lens antennas designed for millimeter wave application,” in *Proc. Infrared Millimeter Waves and 14th Int. Conf. on Teraherz Electronics*, Shanghai, China, pp. 376–376, 2006.

[18] R. J. Mailloux, *Phased Array Antenna Hand Book*. Norwood, MA: Artech House, 1994.

[19] C. G. M. Ryan, M. R. Chaharmir, J. Shaker, J. R. Bray, Y. M. M. Antar, A. Ittipiboon, “A wideband transmitarray using dual-resonant double square rings,” *IEEE Trans. Antennas Propag.,* vol. 58, no. 9, pp. 1486–1493, May 2010.

[20] A. H. Abdelrahman, P. Nayeri, A. Z. Elsherbeni, F. Yang, “Bandwidth improvement methods of transmitarray antennas,” *IEEE Trans. Antennas Propag.,* vol. 63, no. 7, pp. 2946–2954, Jul. 2015.

[21] P.-Y. Feng, S.-W. Qu, S. Yang, L. Shen, and J. Zhao, “Ku-band transmitarrays with improved feed mechanism,” *IEEE Trans. Antennas Propag.*, vol. 66, no. 6, pp. 2883–2891, Feb. 2018.

[22] A. Aziz, F. Yang, S. Xu, and M. Li, “An efficient dual-band orthogonally polarized transmitarray design using three-dipole elements,” *IEEE Antennas Wireless Propag. Lett.*, vol. 17, no. 2, pp. 319–322, Feb. 2018.

[23] A. H. Abdelrahman, A. Z. Elsherbeni, F. Yang, “Transmitarray antenna design using cross-slot elements with no dielectric substrate,” *IEEE Antennas Wireless Propag. Lett.*, vol. 13, pp. 177–180, Jan. 2014.

[24] D. T. McGrath, “Planar three-dimensional constrained lenses,” *IEEE Trans. Antennas Propag*., vol. 34, no. 1, pp. 46–50, Jan. 1986.

[25] D. M. Pozar, “Flat lens antenna concept using aperture coupled microstrip patches,” *Electron. Lett.,* vol. 32, no. 23, pp. 2109-2111, Nov. 1996.

[26] Y. Zhou, S. Rondineau, D. Popovic, A. Sayeed, and Z. Popovic, “Virtual channel space time processing with dual-polarization discrete lens antenna arrays,” *IEEE Trans. Antennas Propag.,* vol. 53, no. 8, pp. 2444–2455, 2005.

[27] P. Naseri, F. Khosravi, P. Mousavi, “Antenna-filter-antenna-based transmit-array for circular polarization application,” *IEEE Antennas Wireless Propag. Lett.*, vol. 16, pp. 1389-1392, Dec. 2016.

[28] Q. Cheng, H. F. Ma, and T. J. Cui, “Broadband planar Luneburg lens based on complementary metamaterials,” *Appl. Phys. Lett.*, vol. 95, no. 18, pp. 1-3, Nov. 2009.

[29] A. H. Abdelrahman, F. Yang, A. Z. Elsherbeni, P. Nayeri, C. A. Balanis, *Analysis and Design of Transmitarray Antennas*, San Francisco, CA, USA: Morgan & Claypool, 2017.

[30] M. Li and N. Behdad, "Wideband true-time-delay microwave lenses based on metallo-dielectric and all-dielectric lowpass frequency selective surfaces," *IEEE Trans. Antennas Propag.*, vol. 61, no. 8, pp. 4109–4119, Aug. 2013.

[31] M. Li, M. A. Al-Joumayly, and N. Behdad, "Broadband true-time-delay microwave lenses based on miniaturized element frequency selective surfaces," *IEEE Trans. Antennas Propag.*, vol. 61, no. 3, pp. 1166–1179, Mar. 2013.

[32] W. An, S. Xu, F. Yang, and M. Li, "A double-layer transmitarray antenna using malta crosses with vias," *IEEE Trans. Antennas Propag.*, vol. 64, no. 3, pp. 1120-1125, Mar. 2016.

[33] S. B. Yeap, X. Qing, and Z. N. Chen, "77-GHz dual-layer transmit-array for automotive radar applications", *IEEE Trans. Antennas Propag.*, vol. 63, no. 6, pp. 2833-2837, Jun. 2015.

[34] L. Palma, A. Clemente, L. Dussopt, R. Sauleau, P. Potier, and P. Pouliguen, "Circularly-polarized reconfigurable transmitarray in Ka-band with beam scanning and polarization switching capabilities," *IEEE Trans. Antennas Propag.*, vol. 65, no. 2, pp. 529-540, Feb. 2017.

[35] M. Wang, S. Xu, F. Yang, and M. Li, "Design of a Ku-band 1-bit reconfigurable transmitarray with 16×16 slot coupled elements," 2017 *IEEE AP-S*, San Diego, CA, USA.

[36] Y. Wang, S. Xu, F. Yang, M. Li, "A novel 1 bit wide-angle beam scanning reconfigurable transmitarray antenna using an equivalent magnetic dipole element," *IEEE Trans. Antennas Propag.*, vol. 68, no. 7, pp. 5691-5695, Jul. 2020.

[37] J. Y. Lau and S. V. Hum, "A wideband reconfigurable transmitarray element," *IEEE Trans. Antennas Propag.*, vol. 60, no. 3, pp. 1303-1311, 2012.

[38] G. Liu, H. Wang, J. Jiang, F. Xue, and M. Yi, “A high efficiency transmitarray antenna using double split rings slot elements,” *IEEE Antennas Wireless Propag. Lett.,* vol. 14, pp. 1415-1418, 2015.

[39] B. Rahmati, H. R. Hassani, “High-efficient wideband slot transmitarray antenna,” *IEEE Trans. Antennas Propag.,* vol. 63, no. 11, pp. 5149–5155, 2015.

[40] S. H. R. Tuloti, P. Rezaei, and F. T. Hamedani, “High-efficient wideband transmitarray antenna,” *IEEE Antennas Wireless Propag. Lett.,* vol. 17, no. 5, pp. 817-820, May 2018.

[41] C. Tian, Y.-C. Jiao, G. Zhao, and H. Wang, “A wideband transmitarray using triple-layer elements combined with cross slots and double square rings,” *IEEE Antennas Wireless Propag. Lett*., vol. 16, pp. 1561–1564, 2017.

[42] A. Clemente, L. Dussopt, R. Sauleau, P. Potier, P. Pouliguen, “Wideband 400-element electronically reconfigurable transmitarray in X band,” *IEEE Trans. Antennas Propag.,* vol. 61, no. 10, pp. 5017-5027, 2013.

[43] F. Diaby, A. Clemente, L. Di Palma, L. Dussopt and R. Sauleau, “Impact of phase compensation method on transmitarray performance,” *11th European Conference on Antennas and Propagation (EUCAP)*, pp. 3114-3118, Paris, 2017.

[44] E. Carrasco, J.A. Encinar, and M. Barba, “Bandwidth improvement in large reflectarrays by using true-time delay,” *IEEE Trans. Antennas Propag.*, vol. 56, no. 8, pp. 2496-2503, Aug. 2008.

[45] S.-W. Qu, H. Yi, B. J. Chen, K. B. Ng, and C. H. Chan, “Terahertz reflecting and transmitting metasurfaces,” *Proc. IEEE*, vol. 105, no. 6, pp. 1166–1184, Jun. 2017.

[46] Y.-M. Cai, W. Li, K. Li, S. Gao, Y. Yin, L. Zhao, W. Hu, “A novel ultrawideband transmitarray design using tightly coupled dipole elements,” *IEEE Trans. Antennas Propag*., vol. 67, no. 1, pp. 242-250, Jan. 2019.

[47] L. Xiao, S.-W. Qu, S. Yang, “Wideband planar tightly coupled dipole transmitarray,” *13th European Conference on Antennas and Propagation (EuCAP)*, 2019.

[48] Y. Zhou, F. Zhu, S. Gao, Q. Luo, L.-H. Wen, etc, “Tightly coupled array antennas for ultra-wideband wireless systems,” *IEEE Access*, vol. 6, pp.61851-61866, Oct. 2018.

[49] A. O. Bah, P.-Y. Qin, R. W. Ziolkowski, Y. J. Guo, T. S. Bird, “A wideband low-profile tightly coupled antenna array with a very high figure of merit,” *IEEE Trans. Antennas Propag*., vol. 67, no. 4, pp.2332-2343, Apr. 2019.

[50] J. P. Doane, K. Sertel, J. L. Volakis, “A wideband, wide Scanning tightly coupled dipole array with integrated balun(TCDA-IB),” *IEEE Trans. Antennas Propag.,* vol. 61, no. 9, pp. 4538-4548, Sep. 2013.

[51] X. Huang, Y. J. Guo, J. D. Bunton, “A hybrid adaptive antenna array,” *IEEE Trans. Wireless Commun*., vol. 9, no. 5, pp. 1770–1779, May 2010.

[52] Y. Hu, J. Zhan, Z. H. Jiang, C. Yu, W. Hong, “An orthogonal hybrid analog-digital multibeam antenna array for millimeter-wave massive MIMO systems,” *IEEE Trans. Antennas Propag.,* vol. 69, no. 3, pp. 1393-1403, Mar. 2021.

[53] O. Quevedo-Teruel, J. Miao, M. Mattsson, A. Algaba-Brazalez, M. Johansson, L. Manholm, “Glide-symmetric fully metallic Luneburg lens for 5G communications at Ka-band,” *IEEE Antennas Wireless Propag. Lett.*, vol. 17, no. 9, pp. 1588-1592, Sep. 2018.

[54] Q. Wu, Z. H. Jiang, O. Quevedo-Teruel, J. P. Turpin, W. Tang, Y. Hao, D. H. Werner, “Transformation optics inspired multibeam lens antennas for broadband directive radiation,” *IEEE Trans. Antennas Propag.,* vol. 61, no. 12, pp. 5910-5922, Dec. 2013.

[55] Y. Li, L. Ge, M. Chen, Z. Zhang, Z. Li, J. Wang, “Multibeam 3-D-printed Luneburg lens fed by magnetoelectric dipole antennas for millimeter-wave MIMO applications,” *IEEE Trans. Antennas Propag.,* vol. 67, no. 5, pp. 2923-2933, May 2019.

[56] Z. H. Jiang, F. Wu, X.-W. Zhu, Q. Ren, P. L. Werner, D. H. Werner, "Metasurface-based circularly-polarized multibeam reflect-/transmit-arrays," *14th European Conference on Antennas and Propagation (EuCAP)*, 2020.

[57] A. H. Abdelrahman, P. Nayeri, A. Z. Elsherbeni, and F. Yang, "Single-feed quad-beam transmitarray antenna design," *IEEE Trans. Antennas Propag.,* vol. 64, no. 3, pp. 953–959, Mar. 2016.

[58] A. Aziz, F. Yang, S. Xu, M. Li, "A low-profile quad-beam transmitarray," *IEEE Antennas Wireless Propag. Lett.*, vol. 19, no. 8, pp. 1340-1344, Aug. 2020.

[59] P. Nayeri, F. Yang, and A. Z. Elsherbeni, "Design of single-feed reflectarray antennas with asymmetric multiple beams using the particle swarm optimization method," *IEEE Trans. Antennas Propag.*, vol. 61, no. 9, pp. 4598–4605, Sep. 2013.

[60] Z. H. Jiang, Y, Zhang, W, Hong, "Anisotropic impedance surface-enabled low-profile broadband dual-circularly polarized multibeam reflectarrays for Ka-band applications," *IEEE Trans. Antennas Propag.,* vol. 68, no. 8, pp. 6441-6446, Aug. 2020.

[61] Y. Hu, W. Hong, Z. H. Jiang, "A multibeam folded reflectarray antenna with wide coverage and integrated primary sources for millimeter-wave massive MIMO applications," *IEEE Trans. Antennas Propag.,* vol. 66, no. 12, pp. 6875-6882, Dec. 2018.

[62] M. Ansari, H. Zhu, N. Shariati, Y. J. Guo, "Compact planar beamforming array with endfire radiating elements for 5G applications," *IEEE Trans. Antennas Propag.,* vol. 67, no. 11, pp. 6859-6869, Nov. 2019.

[63] J.-W. Lian, Y.-L. Ban, C. Xiao, Z.-F. Yu, "Compact substrate-integrated 4×8 Butler matrix with sidelobe suppression for millimeter-wave multibeam application," *IEEE Antennas Wireless Propag. Lett.*, vol. 17, no. 5, pp. 928-932, May 2018.

[64] P. Nayeri, F. Yang, A. Z. Elsherbeni, "Bifocal design and aperture phase optimizations of reflectarray antennas for wide-angle beam scanning

performance," *IEEE Trans. Antennas Propag.,* vol. 61, no. 9, pp. 4588-4597, Sep. 2013.

[65] Z. H. Jiang, Y. Zhang, J. Xu, Y. Yu, W. Hong, "Integrated broadband circularly polarized multibeam antennas using Berry-phase transmitarrays for Ka-band applications," *IEEE Trans. Antennas Propag.,* vol. 68, no. 2, pp. 859-872, Feb. 2020.

[66] G. Liu, M. R. D. Kodnoeih, T. K. Pham, E. M. Cruz, D. González-Ovejero, R. Sauleau, "A millimeter-wave multibeam transparent transmitarray antenna at Ka-band," *IEEE Antennas Wireless Propag. Lett.*, vol. 18, no. 4, pp. 631–635, Apr. 2019.

[67] M. Jiang, Z. N. Chen, Y. Zhang, W. Hong, X. Xuan, "Metamaterial-based thin planar lens antenna for spatial beamforming and multibeam massive MIMO," *IEEE Trans. Antennas Propag.,* vol. 65, no. 2, pp. 464-472, Feb. 2017.

[68] G. Li, Z. Wang, Y. Ge, "Multibeam folded transmitarray antenna for massive MIMO applications," *International Workshop on Electromagnetics: Applications and Student Innovation Competition (iWEM),* Sep. 2019.

[69] E. B. Lima, S. A. Matos, J. R. Costa, C. A. Fernandes, N. J. G. Fonseca, "Circular polarization wide-angle beam steering at Ka-band by in-plane translation of a plate lens antenna," *IEEE Trans. Antennas Propag.,* vol. 63, no. 12, pp. 5443-5455, Dec. 2015.

[70] S. A. Matos, E. B. Lima, J. S. Silva, J. R. Costa, C. A. Fernandes, N. J. G. Fonseca, J. R. Mosig, "High gain dual-band beam-steering transmit array for satcom terminals at Ka-band," *IEEE Trans. Antennas Propag.,* vol. 65, no. 7, pp. 3528-3539, Jul. 2017.

[71] Y. Hou, L. Chang, Y. Li, Z. Zhang, Z. Feng, "Linear multibeam transmitarray based on the sliding aperture technique," *IEEE Trans. Antennas Propag.,* vol. 66, no. 8, pp. 3948–3958, Aug. 2018.

[72] M. Beccaria, P. Pirinoli, F. Yang, “Preliminary results on conformal transmitarray antennas,” *IEEE International Symposium on Antennas and Propagation & USNC/URSI National Radio Science Meeting*, Jul. 2018.

[73] S. H. Zainud-Deen, S. M. Gaber, H. A. Malhet, K. H. Awadalla, “Cylindrical perforated transmitarrays,” *The 2nd Middle East Conference on Antennas and Propagation*, Dec. 2012.

[74] T. A. Hill, J. R. Kelly, M. Khalily, T. W. C. Brown, “Conformal transmitarray for scan loss mitigation with thinned reconfiguration,” *13th European Conference on Antennas and Propagation (EuCAP)*, Apr. 2019.

[75] X. Zhong, L. Chen, Y. Shi, and X. Shi, “Design of multiple-polarization transmitarray antenna using rectangle ring slot element,” *IEEE Antennas Wireless Propag. Lett.*, vol. 15, pp. 1803–1806, 2016.

[76] T. Su, X.Yi, B. Wu, “X/Ku dual-band single-layer reflectarray antenna,” *IEEE Antennas Wireless Propag. Lett.*, vol. 18, pp. 338–342, Jan. 2019.

[77] Z.-W. Miao, Z.-C. Hao, Q. Yuan, “Design and implementation of a G-band silicon-based single-layer reflectarray antenna,” *IEEE Antennas Wireless Propag. Lett.,* vol. 16, pp. 2191-2194, May 2017.

[78] L. Guo, H. Yu, W. Che, W. Yang, “A broadband teflectarray antenna using single-layer rectangular patches embedded with inverted L-shaped slots,” *IEEE Trans. Antennas Propag.*, vol. 67, no.5, pp. 3132–3139, Feb. 2019.

[79] H. Li, G. Wang, J. Liang, X. Gao, H. Hou, and X. Jia, “Single-layer focusing gradient metasurface for ultrathin planar lens antenna application,” *IEEE Trans. Antennas Propag.,* vol. 65,no. 3, pp. 1452–1457, Mar. 2017.

[80] S. B. Glybovski, S. A. Tretyakov, P. A. Belov, Y. S. Kivshar, C. R. Simovski, “Metasurfaces: From microwaves to visible,” *Physics Reporots,* vol. 634, pp. 1-72, May 2016.

[81] J. P. S. Wong, M. Selvanayagam, G. V. Eleftheriades, “Design of unit cells and demonstration of methods for synthesizing Huygens metasurfaces,” *Photonics*

*and Nanostructures-Fundamentals and Applications,* 12, no. 4, pp. 360-375. 2014.

[82] C. Pfeiffer and A. Grbic, "Millimeter-wave transmitarrays for wavefront and polarization control," *IEEE Trans. Microw. Theory Techn.,* vol. 61, no. 12, pp. 4407-4417, 2013.

[83] C. Pfeiffer and A. Grbic, "Metamaterial Huygens' surfaces: Tailoring wave fronts with reflectionless sheets," *Phys. Rev. Lett.,* 110, no. 19, 197401, May 2013.

[84] K. Chen, Y. Feng, F. Monticone et al., "A reconfigurable active Huygens' metalens," *Adv. Mater.,* 29, no. 17, 1606422 , May 2017.

[85] B. O. Zhu, et al., "Dynamic control of electromagnetic wave propagation with the equivalent principle inspired tunable metasurface," *Sci. Rep.,* 4, 4971, May 2014.

[86] A. Epstein and G. V. Eleftheriades, "Huygens' metasurfaces via the equivalence principle: design and applications," *J. Opt. Soc. Am. B*, 33, no. 2, pp. A31-A50, Feb. 2016.

[87] M. Selvanayagam and G. V. Eleftheriades, "Circuit modelling of Huygens surfaces," *IEEE Antennas Wireless Propag. Lett.*, 12, pp. 1642-1645, Dec. 2013.

[88] W. Lin, R. W. Ziolkowski, J. Huang, "Electrically small, low-profile, highly efficient, Huygens dipole rectennas for wirelessly powering Internet-of-Things devices," *IEEE Trans. Antennas Propag.,* vol. 67, no. 6, pp. 3670-3679, Mar. 2019.

[89] R. C. Hansen, "Linear connected arrays," *IEEE Antennas Wireless Propag. Lett.,* vol. 3, 2004.

[90] D. Cavallo, A. Neto, G. Gerini, A. Micco and V. Galdi, "A 3- to 5-GHz wideband array of connected dipoles with low cross polarization and wide-scan capability," *IEEE Trans. on Antennas and Propag.*, vol. 61, no. 3, pp. 1148-1154, March 2013.

[91] D. Cavallo, A. Neto and G. Gerini, “PCB slot based transformers to avoid common-mode resonances in connected arrays of dipoles,” *IEEE Trans. on Antennas and Propag.*, vol. 58, no. 8, pp. 2767-2771, Aug. 2010.

[92] A. Neto, D. Cavallo, G. Gerini, and G. Toso, “Scanning performances of wide band connected arrays in the presence of a backing reflector,” *IEEE Trans. on Antennas and Propag.,* Vol. 57, No. 10, pp. 3092-3102, Oct. 2009.

[93] A. Arraiano1, et al. "Ultra-wide beam scanning using a conformal transmit-array for Ka-band." *the13th European Conference on Antennas and Propagation (EuCAP), IEEE*, 2019.

[94] J. Ruze, “Wide-angle metal-plate optics,” *Proc. IRE*, vol. 38, no. 1, pp. 53–69, Jan. 1950.

# Appendix

Properties of elements 2-8 in Chapter 4 under different oblique incidence angles

| **Element 2 ($\angle S_{21} = -41^o$)** | | | | | | | |
|---|---|---|---|---|---|---|---|
| District No. | Oblique incidence angle $\theta_s$ | $\|S_{21}\|$ /dB | $\angle S_{21}$ | Wz /mm | Wc /mm | Lc /mm | Ld /mm |
| 0,1 | 0° | -0.42 | -41° | 3.8 | 1.6 | 0.1 | / |
| 2 | 18° | -0.3 | -38° | 3.8 | 1.4 | 0.05 | / |
| 3 | 26° | -0.18 | -33° | 3.8 | 1.75 | 0.05 | / |
| 4 | 33° | -0.17 | -34° | 3.8 | 1.5 | 1 | 0.9 |
| 5 | 39° | -0.12 | -31° | 3.8 | 1.5 | 1.6 | 1.5 |
| **Element 3 ($\angle S_{21} = -100^o$)** *Note: No 'T' stubs are added in this model.* | | | | | | | |
| District No. | Oblique incidence angle $\theta_s$ | $\|S_{21}\|$ /dB | $\angle S_{21}$ | Wz /mm | Wc /mm | Lc /mm | Ld /mm |
| 0,1 | 0° | -1 | -100° | 4.1 | / | / | / |
| 2 | 18° | -1 | -99° | 4.1 | / | / | / |
| 3 | 26° | -1 | -97° | 4.1 | / | / | / |
| 4 | 33° | -0.9 | -92° | 4.1 | / | / | / |
| 5 | 39° | -0.7 | -88° | 4.1 | / | / | / |
| **Element 4 ($\angle S_{21} = -153^o$)** | | | | | | | |
| District No. | Oblique incidence angle $\theta_s$ | $\|S_{21}\|$ /dB | $\angle S_{21}$ | Wz /mm | Wc /mm | Lc /mm | Ld /mm |
| 0,1 | 0° | -1.67 | -153° | 4.19 | 1.2 | 0.6 | / |
| 2 | 18° | -1.6 | -159° | 4.19 | 1.4 | 0.6 | / |
| 3 | 26° | -1.63 | -151° | 4.19 | 1.4 | 0.6 | / |
| 4 | 33° | -1.6 | -155° | 4.19 | 1.5 | 0.6 | / |
| 5 | 39° | -1.6 | -154° | 4.19 | 1.6 | 0.6 | / |
| **Element 5 ($\angle S_{21} = -187^o$)** | | | | | | | |
| District No. | Oblique incidence angle $\theta_s$ | $\|S_{21}\|$ /dB | $\angle S_{21}$ | Wz /mm | Wc /mm | Lc /mm | Ld /mm |
| 0,1 | 0° | -1.66 | -187° | 4.2 | 1.2 | 0.37 | / |
| 2 | 18° | -1.73 | -187° | 4.2 | 1.3 | 0.37 | / |
| 3 | 26° | -1.8 | -180° | 4.2 | 1.4 | 0.37 | / |
| 4 | 33° | -1.7 | -178° | 4.2 | 1.5 | 0.37 | / |
| 5 | 39° | -1.73 | -180° | 4.2 | 1.5 | 0.3 | / |
| **Element 6 ($\angle S_{21} = -241^o$)** | | | | | | | |
| District No. | Oblique incidence angle $\theta_s$ | $\|S_{21}\|$ /dB | $\angle S_{21}$ | Wz /mm | Wc /mm | Lc /mm | Ld /mm |
| 0,1 | 0° | -1.36 | -241° | 4.25 | 1.5 | 0.4 | / |
| 2 | 18° | -1.38 | -239° | 4.25 | 1.6 | 0.4 | / |
| 3 | 26° | -1.36 | -244° | 4.25 | 1.6 | 0.3 | / |
| 4 | 33° | -1.39 | -242° | 4.25 | 1.5 | 0.2 | / |

| | | | | | | | |
|---|---|---|---|---|---|---|---|
| 5 | 39° | -1.43 | -234° | 4.25 | 1.4 | 0.15 | / |
| **Element 7 ($\angle S_{21} = -284^o$)** | | | | | | | |
| District No. | Oblique incidence angle $\theta_s$ | $\lvert S_{21} \rvert$ /dB | $\angle S_{21}$ | Wz /mm | Wc /mm | Lc /mm | Ld /mm |
| 0,1 | 0° | -0.86 | -284° | 4.3 | 1.62 | 0.4 | / |
| 2 | 18° | -0.84 | -286° | 4.3 | 1.5 | 0.3 | / |
| 3 | 26° | -0.81 | -287° | 4.3 | 1.45 | 0.2 | / |
| 4 | 33° | -0.8 | -288° | 4.3 | 1.7 | 0.2 | / |
| 5 | 39° | -0.82 | -288° | 4.3 | 1.5 | 0.1 | / |
| **Element 8 ($\angle S_{21} = -330^o$)** | | | | | | | |
| District No. | Oblique incidence angle $\theta_s$ | $\lvert S_{21} \rvert$ /dB | $\angle S_{21}$ | Wz /mm | Wc /mm | Lc /mm | Ld /mm |
| 0,1 | 0° | -0.5 | -330° | 4.4 | 1.62 | 0.35 | / |
| 2 | 18° | -0.45 | -328° | 4.4 | 1.6 | 0.3 | / |
| 3 | 26° | -0.46 | -333° | 4.4 | 1.6 | 0.2 | / |
| 4 | 33° | -0.42 | -330 | 4.4 | 1.45 | 0.1 | / |
| 5 | 39° | -0.4 | -332° | 4.4 | 1.7 | 0.1 | / |